Recent advances of electrodeposition of Bi_2Te_3 and its thermoelectric applications in miniaturized power generation and cooling

Tai-feng Shi[a], Jing-yuan Zheng[a], Xia Wang[a], Peng Zhang[b], Peng-an Zong[a*], Kafil M. Razeeb[c*]

[a]*College of Materials Science and Engineering, Nanjing Tech University, Nanjing 210009, China;* [b]*Faculty of Materials and Manufacturing, Beijing University of Technology, Beijing, 100124, China;* [c]*Micro-Nano Systems Centre, Tyndall National Institute, University College Cork, Dyke Parade, Lee Maltings, Cork T12 R5CP, Ireland*

*Corresponding Authors.

Email: pazong@njtech.edu.cn (P. A. Zong); kafil.mahmood@tyndall.ie (K. M. Razeeb)

Abstract:

Thermoelectric (TE) technology enables direct conversion between thermal and electrical energy and thus has been regarded as an alternative for energy harvesting and refrigeration. Bismuth telluride (Bi_2Te_3) is the most widely used TE material at room temperature due to its high figure of merit (~1). Since the first publication on the electrodeposition of Bi_2Te_3 films in 1994, a large number of publications has emerged in the last two decades, owing to its advantages such as simple and safe preparation, high deposition rate, convenient micromachining, good compatibility to semiconductor microfabrication techniques, etc. This article reviews the recent research progress in electrodeposition of Bi_2Te_3 and its application in TE devices. Additionally, an outlook towards the future development of this area has also been discussed.

Keywords: Thermoelectric; bismuth telluride; electrodeposition; nanocomposite; Bi_2Te_3-based ternary alloys; TEG

Content

0. Introduction

Thermoelectrics (TEs) enable direct conversion from heat to electricity and vice versa and thus have long been considered for use in low carbon alternative energy generation and recovery or solid-state Peltier coolers. The conversion efficiency of TE devices (TEDs), including TE generators (TEGs) and TE coolers (TECs), is currently lower than traditional mechanical generators or compression-type refrigerators. Nevertheless, they possess special advantages such as having no moving parts, being reliable, safe, silent and scalable, thereby making them ideal for niche and distributed power generation, such as powering deep space exploration, portable devices and wearable electronics, or for energy recovery from waste heat; and for localized cooling applications, such as for cooling 5G stations, high-end chips, etc. [1]. The TE conversion efficiency (η) of TEGs is given by [2]:

$$\eta_{max} = \frac{T_h - T_l}{T_h} \frac{\sqrt{1+ZT}-1}{\sqrt{1+ZT}+T_l/T_h} \quad (1)$$

and the coefficient of performance (COP) of TECs is [3]:

$$COP_{max} = \frac{T_l}{T_h - T_l} \frac{\sqrt{1+ZT}-T_h/T_l}{\sqrt{1+ZT}+1} \quad (2)$$

where T_h is the hot-side temperature, T_l is the cold-side temperature, and, ZT is the TE figure of merit of material at the ambient temperature $T = (T_h+T_l)/2$ [4]:

$$ZT = \frac{\sigma S^2 T}{k} \quad (3)$$

where, σ is the electrical conductivity, S is the Seebeck coefficient, and κ is the thermal conductivity. κ has two components: the carrier transport part (κ_e) and phonon transport part (κ_l). σS^2 is defined as the power factor (PF) and is the comprehensive indicator of a material's relevant electrical properties. For traditional TE materials with $ZT \sim 1$, η of the corresponding TEGs is ~ 13% at T_h = 900 K and T_l = 300 K. One has to boost ZT to ~ 3 for η to be ~30 %, so as to be competent against traditional

generator [5−7]. Similarly, *ZT* should reach ~ 4, thereby the TECs can compete against traditional refrigeration at room temperature (RT) [8].

For near room-temperature applications, the most widely used TE material is bismuth telluride (Bi_2Te_3) and its alloys, with a *ZT* ~ 1 at RT. The alloys of Bi_2Te_3 are n-type when alloyed with bismuth selenide (Bi_2Se_3) whereas being p-type with antimony telluride (Sb_2Te_3) [9 − 11]. Bi_2Te_3 is orthorhombic with a rhombohedral layered structure, exhibiting a bandgap of ~ 0.15 eV. The constituent atoms are arranged in the order of Te_1-Bi-Te_2-Bi-Te_1, wherein Bi and Te_1 or Te_2 atoms are connected by covalent bonds, while adjacent Te_1 atoms interact with the Van der Waals forces **(Figure 1(a))** [12]. The unit cell parameters of Bi_2Te_3 at RT are a = 3.8 Å and c = 30.5 Å and its single crystal cleavage plane is perpendicular to the c-axis direction [13]. The transport of electrons and phonons are impeded to different degrees by the Van der Waals gap of Te_1-Te_1. The in-plane σ and κ are 3 ~ 7 times and 2 ~ 2.5 times that of cross-plane ones, respectively, whereas the *S* is regarded as isotropic, resulting in a better TE performance perpendicular to the c axis [14−16]. As shown in **Figure 1(b)**, Manzano et al. [13] deposited polycrystalline Bi_2Te_3 films highly oriented along the [110] direction by pulsed electrodeposition. The ratio between the out-of-plane and in-plane ZT is approximately 1.8, agreeing well with single crystal bulk Bi_2Te_3.

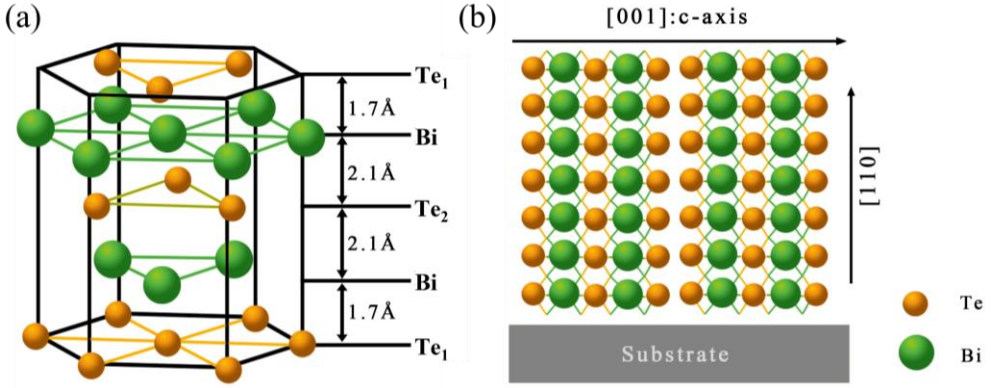

Figure 1. (a) Crystal structure of quintuple Bi_2Te_3. (b) Preferential orientation of the pulse electrodeposited polycrystalline Bi_2Te_3 film on a substrate [13].

So far researchers have synthesized Bi_2Te_3 thin films by a variety of methods, such as solvothermal method (ST) [17−21], pulsed laser deposition (PLD) [22−26], thermal evaporation (EVP) [27−31], magnetron sputtering (MS) [32−34], and electrodeposition (ED) [35,36]. From the viewpoint of performance, as shown in Table 1, the Bi_2Te_3 film prepared by ED showed a power factor of 30.2 $\mu W\ cm^{-1}K^{-2}$ according to the latest work [37], which is 1−2 orders of magnitude higher than that made by solvothermal method (ST), better than that made by thermal evaporation (EVP) and magnetron sputtering (MS), and comparable to that made by pulsed laser deposition (PLD). Therefore, ED is competitive among all known methods to prepare Bi_2Te_3 films from the viewpoint of performance. From the viewpoint of production process, firstly, the raw materials used in ED are oxides and salts, which are of lower cost than the high-purity ($\geq$ 3N) Bi, Te metals or Bi_2Te_3 alloys utilized in PLD, EVP, and MS. Secondly, ED can be carried out in air at RT, while PLD, EVP and MS are conducted in high vacuum ($\leq 10^{-3}$ Pa) or high-purity inert gas ($\geq$ 4N) at high temperatures. Thirdly, the PLD, EVP, and MS methods demand evaporation of Bi and Te atoms ahead of deposition, entailing a larger energy consumption for breaking chemical bonds. Fourthly, as ED process is driven by an electrical field, ED can only take place on conducting areas, thus it can realize region-selective deposition for designed patterns. Although the PLD, EVP and MS methods can also realize designed patterns by masking unintended regions, the Bi_2Te_3 layers are also deposited on the masks (e.g. photoresist), which causes a waste of raw materials. Fifthly, ED can be combined with complementary metal-oxide-semiconductor (CMOS) technology to prepare high-power-density TEGs or TECs [38,39]. These endow ED special advantages in the preparation of micro-TEDs, which is of great significance for power generation or cooling of next-generation microelectronic and photonic devices. Considering all the above factors, ED is a cost-effective preparation method of the Bi_2Te_3 films and more competent

to scale-up for the further development of micro-devices.

Table 1. RT TE properties and thickness of Bi_2Te_3 thin films prepared by different methods, and the raw materials as well as conditions utilized.

Method	σ (Scm^{-1})	S (μVK^{-1})	PF ($\mu Wcm^{-1}K^{-2}$)	THK (μm)	Raw materials	Atmosphere	T	Ref.
ED	399	−275	30.2	1.85	TeO_2, Na_2TeO_3, $Bi(NO_3)_3$, Bi_2O_3 etc. (≥ 2N)	Air	RT	[37]
ED	500	−148	11.0	3.80				[36]
ED	2000	−100	20.1	-				[140]
ED	690	−146	14.7	3.00				[16]
PLD	1080	−160	27.7	1.50	Bi, Te, Bi_2Te_3 target (≥ 3N)	Vac. (≤ 10^{-3} Pa)	200 ~ 600 ℃	[23]
PLD	-	-	56.8	0.03				[26]
PLD	33000	−52	83.8	0.60				[24]
EVP	670	−160	17.0	-	Bi, Te, Bi_2Te_3 target (≥ 3N).	Vac. (≤ 10^{-3} Pa)	~ 230 ℃	[31]
EVP	500	−233	27.0	0.40				[29]
MS	1020	−163	27.3	1.00	Bi, Te, Bi_2Te_3 target (≥ 3N)	Ar（≥ 4N）	150 ~ 300 ℃	[33]
MS	470	−148	10.2	1.00				[34]
ST	120	−74	0.7	1.50	TeO_2, Na_2TeO_3, $Bi(NO_3)_3$, Bi_2O_3 etc. (≥ 2N)	Air	~200 ℃	[18]
ST	40	−300	3.5	40.00				[19]
ST	120	−103	1.3	10.00				[20]

Note: TE properties in ***Ref.*** 29 were measured at 83 °C. Vac.: vacuum, THK: thickness, T: temperature. 2N: 99 %, 3N: 99.9 %, 4N: 99.99 %.

The TE properties of an electrodeposited Bi_2Te_3 film are strongly correlated to its composition and microstructure, which are determined by the deposition process. Adjusting Bi^{III}/Te^{IV} ionic ratio ($C_{Bi^{III}}/C_{Te^{IV}}$) can control the stoichiometric ratio in the product, thereby tuning the TE properties of the film. Being away from the optimal $C_{Bi^{III}}/C_{Te^{IV}}$, miscellaneous phases such as BiTe and Bi_2Te other than Bi_2Te_3 would be formed. Therefore, predesigning of $C_{Bi^{III}}/C_{Te^{IV}}$ is essential for a high-property film. Utilizing appropriate deposition mode, potential and temperature, a specific electrolyte system, including surfactant or annealing process can generate films that are smooth and dense, which in turn can boost the TE properties. However, reviews of Bi_2Te_3 electrodeposition are rare [40,41]; and

the ones that exist mainly summarize the ED processes of Bi_2Te_3, and discuss the microstructures and properties of the products, without thoroughly commenting on the underlying relationships between among processes, microstructures and properties, which are significant factors for process optimization. Meanwhile, several hundred update research articles on the ED of Bi_2Te_3 have been published in recent years. Accordingly, this work aims to provide for the reader a guidance for ED processes optimization, to achieve high-performance Bi_2Te_3 films and their TEDs, based on a thorough analysis of the inter-relationship between processes, microstructures and properties. More than 200 recent and enlightening literature are cited or commented on in this critical review and underlying mechanisms are summarized and future challenges proposed.

1. Mechanism

ED of Bi_2Te_3 is usually carried out using a three-electrode system. One loop composed of working electrode (WE), counter electrode (CE) and power supply, is designed to transmit electrons and induce an electrochemical reaction on the WE. The other loop composed of WE and reference electrode (RE), is set to monitor the electrochemical reaction process on the WE. As shown in **Figure 2**, when an external voltage is applied, the WE would be filled with electrons, and an electric field is thus established between WE and CE. As a result, the Bi^{III} and Te^{IV} cations contained in the electrolyte (in the form of Bi^{3+} and $HTeO_2^+$, respectively) would migrate to the WE, and be reduced on the surface of the WE. The general formula of the electrochemical reaction can be expressed as [42]:

$$2\,Bi^{3+} + 3\,HTeO_2^+ + 18\,e^- + 9\,H^+ \rightarrow Bi_2Te_3 + 6\,H_2O \quad (4)$$

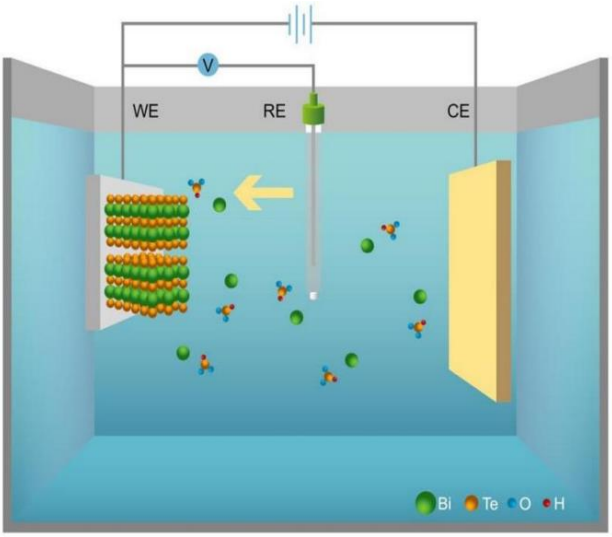

Figure 2. Schematic diagram showing ED process of Bi_2Te_3 film.

The above equation is a complex reaction with reductions occurring of both Bi^{III} and Te^{IV} cations. It is thus important to illustrate the underlying reaction sequences to understand the deposition mechanisms. Firstly, the ionic mobilities (m) of Bi^{III} and Te^{IV} cations under a fixed temperature in the same electrolyte system are different, which can be expressed by the formula [43]:

$$m = \frac{ez}{6\pi vr} \tag{5}$$

where e is the elementary charge, z is the ionic-charge number, v is the viscosity of the electrolyte, and r is the ionic radius. In the same system (for example, 1M nitric acid, HNO_3), Te^{IV} cations (r = 0.206 nm, z = 4) has a larger m than Bi^{III} cations (r = 0.253 nm, z = 3) [44]. Secondly, since the electron affinity of Te^{IV} is larger than Bi^{III}, the onset potential (potential at which the reduction is started, E_{onset} [45]) of Te^{IV} is thus more positive (**Figure 3(a)**), which means that the reduction of Te^{IV} takes place at first during co-deposition (**Figure 3(b)**). Thirdly, due to a lower work function in Bi (~ 4.0 eV) than that in Te (~ 4.22 eV) and the contribution of the interaction between Bi and Te, the underpotential deposition of Bi would occur then, namely, Bi can be deposited on Te at a positive potential than its thermodynamically reversible potential [46,47]. It is thus considered that Te^{IV} cations are reduced to

Te^0 on the WE at first, and then Bi^{III} cations are deposited and bonded with reduced Te^0 to form Bi_2Te_3. The ED reaction of Bi_2Te_3 can then be separated into two steps [48]:

$$HTeO_2^+ + 4e^- + 3H^+ \rightarrow Te^0 + 2H_2O \quad (6)$$

$$3Te^0 + 2Bi^{3+} + 6e^- \rightarrow Bi_2Te_3 \quad (7)$$

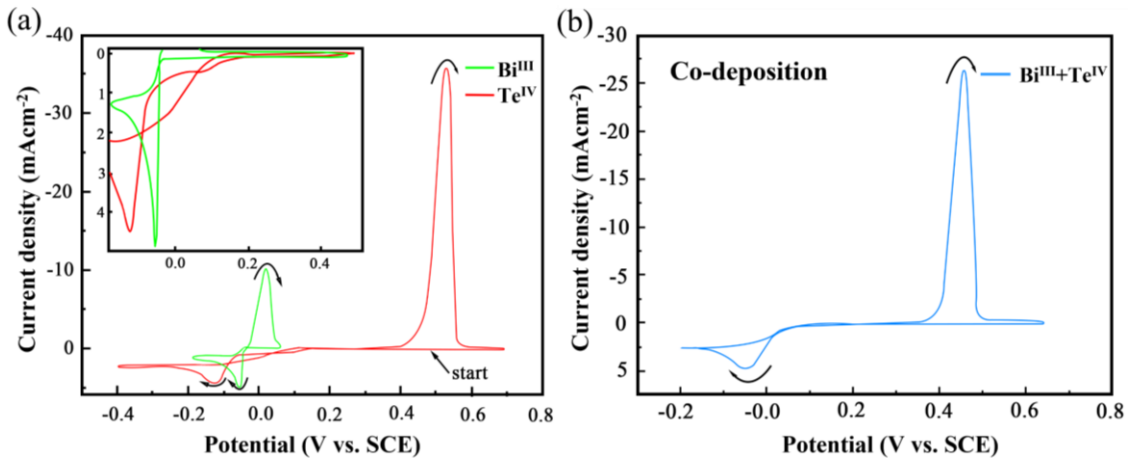

Figure 3. (a) Cyclic voltammograms (CV) of WE in 10 mM Bi^{III} or 10 mM Te^{IV}/1M HNO_3 aqueous solutions, respectively. (b) CV of WE in 10 mM Bi^{III} plus 10 mM Te^{IV}/1M HNO_3 aqueous solutions (Co-deposition) [48]. Copyright 2009, Elsevier. Reprinted with permission.

However, one recent work raised a different mechanism. Bo et al. [49] deposited Bi^{III} on composite indium tin oxides (ITO)-gold and ITO-gold-tellurium electrodes, vis: (ITO)/Au and ITO/Au/Te. It was found that elemental Te did not promote the deposition of Bi^{III}, as their cyclic voltammetry (CV) curves almost overlapped. Likewise, they deposited Te^{IV} on ITO/Au and ITO/Au/Bi, respectively. On the other hand, elemental Bi was apparently found to promote the deposition of Te^{IV}, as the E_{onset} was positively shifted in the latter case. Therefore, they claimed that Bi^{III} cations are first reduced to Bi^0, and then Bi^0 promotes the reduction of Te^{IV}. However, we believe this experimental design needs further improvement to make it more convincing. Firstly, the Bi^{III} and Te^{IV} cations were designed to be deposited on sputtered elemental Te and Bi films respectively in the experiment. The

Te and Bi are present in form of micro-grains in the film, which have far less surface energy than the Te^0 and Bi^0 in atomic state during ED of Bi_2Te_3 [50,51]. In addition, it is reasonable that the E_{onset} is altered when the substrate changed from Au to Bi due to altered kinetics [52]. The *m* of Bi^{III} and Te^{IV} cations can also be affected by temperature, mechanical stirring and other factors [53−56]. Direct evidence of the deposition sequence remains an issue, for which new in-situ atomic-scale investigation technology is to be developed.

2. Electrolyte

The electrolyte is the medium that provides necessary ions and facilitates ionic motions for mass transfer. Therefore, the electrolyte is one of the key factors that affects the TE properties of the electrodeposited films. This section discusses the influence of electrolyte-related factors (impurities, solvents, surfactants, temperature and ionic concentration, etc.) on the compositions, microstructures as well as TE properties of the electrodeposited Bi_2Te_3.

2.1 Impurities

The Bi^{III} and Te^{IV} cations in the electrolyte are usually provided by Bi metal powder or bismuth nitrate ($Bi(NO_3)_3$) salt, and Te or tellurium oxide (TeO_2) powders respectively. However, the presence of impurities in the raw materials is inevitable, which potentially has an impact on the TE properties of the film that cannot be neglected. Manzano et al. [57] used Te and Bi powder with different purities to deposit Bi_2Te_3 and investigated the influence of the impurities on the TE properties. Film A was made of 4N-purity raw materials with trace Se, Film B was made of 5N-purity materials and Film C was made of 4N-purity raw materials with a trace amount of alkali metal elements such as Na and K.

As shown in **Figure 4**, Film A had the best σ and PF, because trace Se doping induces vacancies, and ionize electrons, thus increasing n. The electrical conductivity, σ can be calculated by the formula [16]:

$$\sigma = ne\mu \quad (8)$$

where n is the carrier concentration, μ is the carrier mobility and e is the charge of an electron. As the electronic structure is not altered by Se doping, μ can be maintained, so that σ is increased [58]. Film C revealed the worst TE properties, due to the substitution of high valence Bi^{3+} with low valence Na^{+} or K^{+}, which introduces holes and point defects in Bi_2Te_3, thus reducing n and μ, and consequently lowering the σ [59−61]. The alkali metal elements such as Na and K usually exist in ordinary deionized water, which are readily doped into the product by electrolyte bath. Hence, the impurity species in the raw materials have a greater impact on the TE properties than purity. As was reported, doping of appropriate donor impurities, such as Se [58], Cu [62], etc. [63−64] into n-type Bi_2Te_3, could increase n and optimize PF; otherwise, will deteriorate the TE properties [65−67]. One may expect optimizing the TE performance by purposely doping appropriate impurities into electrodeposited Bi_2Te_3 by electrolyte bath.

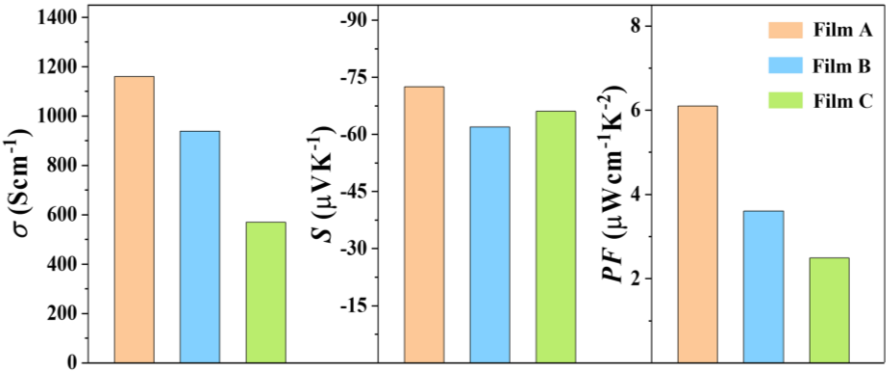

Figure 4. TE properties of Film A, B, C made of raw materials with 4N (with trace Se), 5N and 4N (with trace K and Na) purity respectively [57].

2.2 Solvent systems

Aqueous solutions: Compared with Bi^{III} cations, Te^{IV} species exhibit much lower solubilities in aqueous solution [68]. To ensure a higher $C_{Te^{IV}}$, ED of Bi_2Te_3 is often carried out in a strong acidic electrolyte, mainly in HNO_3, where Te^{IV} cations exist in the form of $HTeO_2^+$ with high solubility (**Figure 5 (a)**). However, the maximum $C_{Te^{IV}}$ in 1 M HNO_3 can only reach 50 mM, which is still much lower than that of Bi^{III} cations (~ 400 mM) [68,69]. The solution acidity is seldom realized by hydrochloric acid (HCl) or sulfuric acid (H_2SO_4). Kang et al. [70] investigated the electrochemical reduction behaviors of Bi^{III} and Te^{IV} cations in HNO_3 and HCl electrolytes. It has been found that a higher HNO_3 concentration (a lower pH) leads to a higher $C_{Te^{IV}}$, thus promoting the reduction of Te^{IV} (Equation 6). However, too low pH values would have an adverse effect, because redundant H^+ cations would adsorb on the deposited Te^0, and impede the reduction of Bi^{III} cations due to the Coulomb repulsion. Moreover, the hydrogen evolution potential shifted positively when the pH value decreased. It could coincide with the ED potential of Bi_2Te_3, so that the hydrogen evolution reaction occurs concurrently with ED of Bi_2Te_3, engendering a loose and porous structure. Therefore, the determination of an optimal HNO_3 concentration is of great significance.

In HCl electrolyte, Cl^- anions would chelate with Bi^{III} and Te^{IV}, generating $BiCl_x^{3-x}$ and $TeCl_x^{4-x}$ complex ions, respectively (**Figure 5(d)**). The formation of the complex structure $BiCl_x^{3-x}$ makes the reduction of Bi^{III} difficult, due to the presence of a coordination bond. On the contrary, the reduction of Te^{IV} in the form of $TeCl_x^{4-x}$ becomes easier than $HTeO_2^+$ due to the ion bridging effect, which could hasten the electron flows from WE to the adsorbed cations [71]. Thus, increasing the HCl concentration is more effective for promoting the reduction of Te^{IV} than HNO_3. As shown in **Figure 5(b−c)**, the Bi_2Te_3 electrodeposited in the HNO_3 system exhibits a needle-like morphology from the surface view

and columnar grains with a preferred (1 1 0) orientation from the cross-sectional view. While the Bi_2Te_3 electrodeposited in the HCl solution exhibits a nanocrystalline structure with ball-like morphology **(Figure 5(e−f))**. Because the nanocrystalline structures have a lager grain boundary density than the columnar structures, the μ was depressed by 3 ~ 4 times, leading to decreased σ and *PF* (**Table 2**).

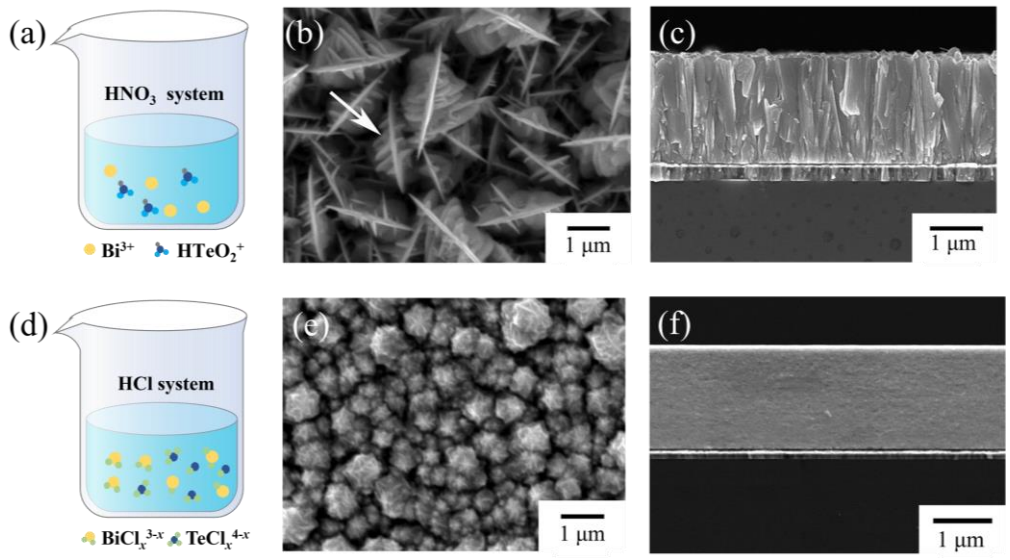

Figure 5. Schematic diagrams of the existing forms of Te^{IV} and Bi^{III} in (a) HNO_3 and (d) HCl aqueous solution**.** (b, c) Surface and Cross-sectional SEM images of the deposited film in 0.7 M HNO_3 and (e, f) 0.35 M HCl aqueous solution [70]. Copyright 2017, Elsevier. Reprinted with permission.

Regarding the H_2SO_4 system, Heo et al. [72] electrodeposited Bi_2Te_3 in the H_2SO_4 system in 2006. A maximum *PF* of 7.40 $\mu Wcm^{-1}K^{-2}$ was obtained, comparable to HNO_3 system (**Table 2**). However, in H_2SO_4 system, since the produced bismuth sulfate, $Bi_2(SO_4)_3$, is very difficult to dissolve (~ 2 mM at pH = 0.5), the yield of Bi_2Te_3 is severely restricted at a certain volume of electrolyte. There has been no follow-up report in H_2SO_4 electrolyte systems since. Therefore, considering the ionic concentration of the electrolyte, microstructure and TE performance of the Bi_2Te_3 film, the HNO_3 solution is the best choice to date. We believe that if one could develop a complexing agent that can form a complex with Te^{IV} while leaving Bi^{III} free in HNO_3 system, it would enlarge the Te^{IV} concentration and narrow the

mobility difference between Te^{IV} and Bi^{III}, so as to obtain uniform Bi_2Te_3 film with high TE performance.

Nonaqueous solutions: The strong acidity of inorganic acid aqueous solutions has strong corrosiveness to some electrodes, such as anodic aluminum oxide (AAO), metal foams, etc. [73,74]. Besides, the hydrogen evolution reaction brought by low pH usually makes the film loose and porous, thereby reducing TE performance [16,77]. To overcome the above shortcomings, researchers have electrodeposited Bi_2Te_3 in nonaqueous solutions such as dimethyl-sulfoxide (DMSO) [75], ethylene glycol (EG) [76], and dichloromethane (DCM) [77], etc. Cicvarić et al. [77] deposited Bi_2Te_3 in DCM at a deposition potential of −0.6 V, before which a large potential of −1 V was applied for 5 s for quick nucleation of Bi_2Te_3 seeds. Because the permittivity of DCM ($\varepsilon_r = 8.9$) is only 1/9 of water ($\varepsilon_r = 80$) [78−81], the capacity of dissolution and dissociation of salts is greatly limited [82]; the $C_{Bi^{III}}$ and $C_{Te^{IV}}$ in DCM were only 3 and 3 mM, respectively. Which are 1-2 orders of magnitude lower than in HNO_3. Moreover, the organic chains in DCM readily chelate with Bi^{III} and Te^{IV}, which induce coordination bonds, thus enlarging the overpotential [70]. The small ionic concentration as well as the high current density due to the larger overpotential could restrict the grain growth because Bi^{III} or Te^{IV} species are always insufficient and late for the replenishment. As a result, the grain size of the film is small and the grain boundary density is high. In addition, there are residual organic species at the grain boundaries. The above defects cause carrier scattering. This greatly reduces the σ to 62.9 Scm^{-1}, a value two orders of magnitude lower than HNO_3 system, 1408.5 Scm^{-1} (**Table 2**). The *PF*, 0.17 $\mu Wcm^{-1}K^{-2}$, is therefore far inferior to HNO_3 system (7.32 $\mu Wcm^{-1}K^{-2}$).

The viscosity of the most nonaqueous solution is higher than that of the aqueous solution [78], it has an adverse effect on *m* via equation 5. Because the deposition rate is proportional to *m*, a larger

overpotential is required in nonaqueous solution than in aqueous solution in order to reach the same deposition rate. However, under a high overpotential, the nucleation rate of Bi_2Te_3 is much larger than its growth rate, implying that the nucleation is dominant in nonaqueous solution. Besides, considering the low σ and ε_r of organic solvents, some supporting electrolytes, such as $NaClO_4$, $HClO_4$ and Tetra-n-butylammonium perchlorate, can be added to improve the σ and solvability [78,83−85]. However, this may incorporate unwanted impurities into the Bi_2Te_3 film and degrade its TE properties. Most solutions in REs are aqueous and the direct contact with nonaqueous solutions can cause contamination. Hence, the use of REs in nonaqueous solutions is more complex and this will be discussed in section 4.2.

Table 2. RT TE properties and grain sizes of Bi_2Te_3 films electrodeposited in different solvent systems.

Solvent systems	V_{dep} **(V)**	S (μVK^{-1})	σ (Scm^{-1})	μ ($cm^2V^{-1}s^{-1}$)	n (10^{20} cm^{-3})	**Grain-size** (nm)	PF ($\mu Wcm^{-1}K^{-2}$)	**Ref.**
HNO_3	−0.02	−72	1409	7.97	−11	-	7.32	[70]
HCl	−0.02	−105	153	2.38	−4	15	1.69	[70]
H_2SO_4	−0.10	−100	740	-	-	-	7.40	[72]
EG	+0.02	+240	-	-	-	-	-	[76]
DCM	−0.60	−52	63	-	-	4	0.17	[77]

Note: V_{dep}: Deposition potential.

2.4 Surfactants

Surfactants are long chain molecules with a polar (hydrophilic) group at one end and a non-polar (lipophilic) group at the other. While the polar end has an affinity for the molecules of a polar solvent, the non-polar end will have an affinity for the gas phase, so surfactants can significantly reduce the surface tension of the target solution [86]. Due to the sigma and pi bonds in the molecular structure of

surfactants, including polar and non-polar forces, as well as other electronic factors (charge, ionic or dipole effect), they are readily to be adsorbed onto the surface of deposited grains, thus adjusting the grain growth [87,88]. Different surfactant species have different influence on the growth of Bi_2Te_3, resulting in different grain-sizes (**Table 3**) and size-distributions [88−90]. For example, some surfactants such as polyvinyl pyrrolidone (PVP) and sodium dodecyl sulfate (SDS) can form functional assembly with Bi_2Te_3 and narrow the size distribution of grains, thus improving the μ by weakening electronic scattering [88].

An enhanced (1 1 0) orientation was observed after adding sodium lignosulfonate (SLS) as the surfactant [91]. Without SLS, the film grows in a typical Volmer-Weber model [92−94]. As shown in **Figure 6(a)**, due to the poor infiltration between the deposited Bi_2Te_3 and the substrate, atoms of Bi_2Te_3 are more inclined to bond with each other and condense into numerous isolated small nuclei, thus forming three-dimensional islands. After growing for a period of time, the film structure collapses to leave a void inside, thus making a loose film with poor TE properties due to a reduced μ. With the assistance of SLS, the infiltration is enhanced, the deposited Bi_2Te_3 first grows in a Frank-van der Merwe mode **Figure 6(b)**, where the atoms tend to bond with the substrate atoms, and spread along the substrate surface. After the growth of an initial layer of atomic thickness, the growth follows the Stranski-Krastanov model (**Figure 6(c)**), implying a transition from a layered growth to an island growth. The growth is isotropic with ball-like nucleation points. These balls grow and merge with each other, ensuring a dense, smooth, and isotropic film, and an enhanced TE performance can be achieved (**Table 3**).

Song et al. [95] added cetyltrimethylammonium ammonium bromide (CTAB) as the surfactant, and the film (**Figure 6(e)**) becomes smoother and denser than that without CTAB (**Figure 6(d)**). The

preferential orientation was also changed from (0 1 5) to (1 1 0) as a result of under potential deposition. Both the σ and S were increased, resulting in a nearly doubled PF (**Table 3**). The hardness and elastic modulus were improved as well, approaching that of bulk Bi_2Te_3 (**Figure 6(f)**). We believe that after adding CTAB, there is also a transition of the growth model from the Volmer-Weber model to the Stranski-Krastanov model one as discussed above.

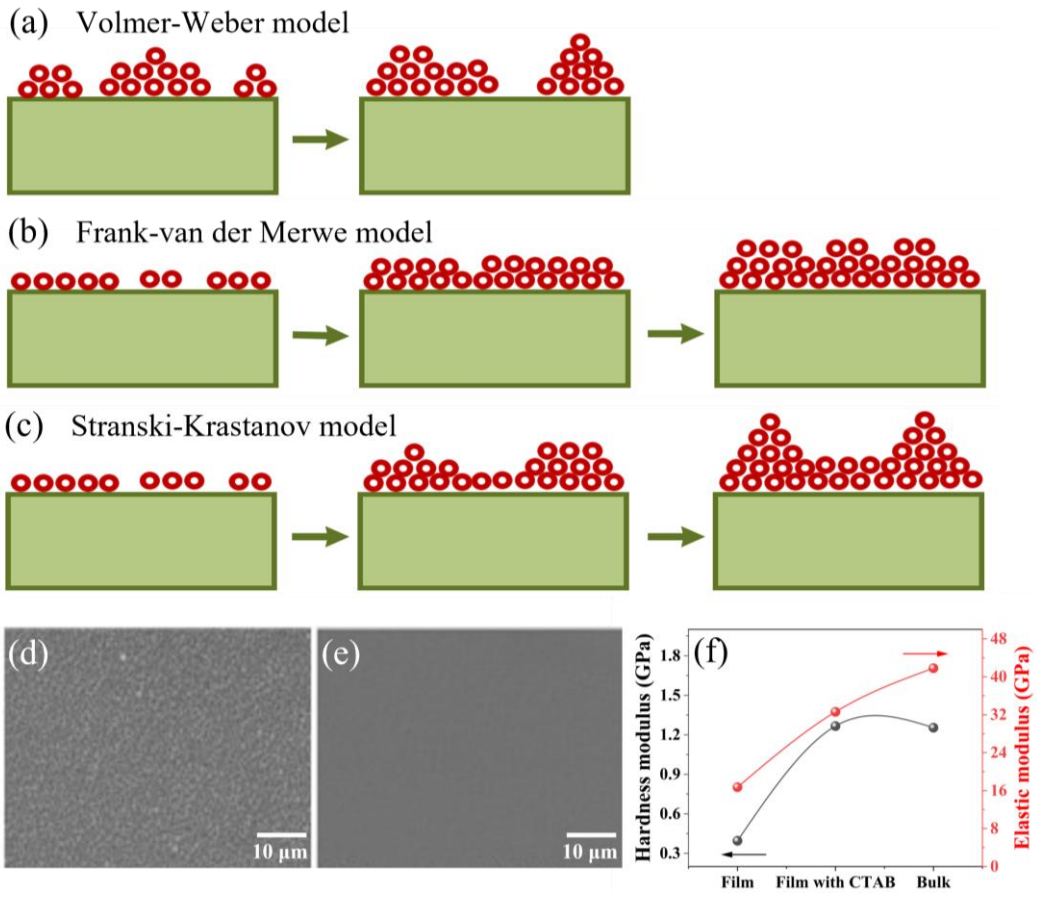

Figure 6. (a) Schematic diagram of Volmer-Weber growth mode, (b) Frank-van der Merwe growth mode and (c) Stranski-Krastanov growth mode of film growth during ED. SEM images of the deposited Bi_2T_3 films (d) without and (e) with CTAB. (f) Hardness and elastic modulus of Bi_2Te_3 films deposited with/without CTAB and bulk Bi_2Te_3 [95]. Copyright 2015, Elsevier. Reprinted with permission.

Polyvinyl alcohol (PVA) is often used as a surface inhibitor because it can enhance the adhesion

of films, facilitate the formation of a homogeneous film, improve nuclei density and decrease grain size [96]. However, the insulating PVA locating at the grain boundaries can impede the carrier transport, leading to a low σ. In addition, PVA has been proven to increase the internal tensile stress of the film and lead to cracks. This is because the long PVA chains readily attract and entangle with each other, which increases the friction between the grains [97]. Sodium saccharin (SS) can be used to reduce the internal stress of the film. SS incorporates sulfur at the island boundaries, reducing the grain-boundary energy, thus causing a systematic reduction in the tensile grain-boundary coalescence stress [98−100]. Yu et al. [101] used multiple additives including PVA, SS and KCl salt for ED of Bi_2Te_3 film, the deposited film achieved an elevated *PF* of 8.34 $\mu Wcm^{-1}K^{-2}$, which is considerably larger than that without additives (**Figure 7(d)**). As shown in **Figure 7(a)**, the deposited film is rough and fragile, when no additives are used. The addition of PVA can effectively enhance adhesion to substrate and smooth the film surface, but bring in enormous micro cracks due to a high internal stress. Further addition of SS can remove micro-cracks by decreasing tensile stress while increasing compressive stress. A smooth and compact film can be obtained with a low deposition rate, as the grain growth is inhibited by SS ((**Figure 7(b)**)). Thus, the σ is severely lowered due to the high density of grain boundaries. Further addition of KCl could boost the ionic conductivity of the electrolyte, benefit grain growth (**Figure 7(c)**) and speed up ED rate, thus adjusting the grain size to a higher level for an enhanced σ and, eventually, an optimized *PF* (**Figure 7(d)**).

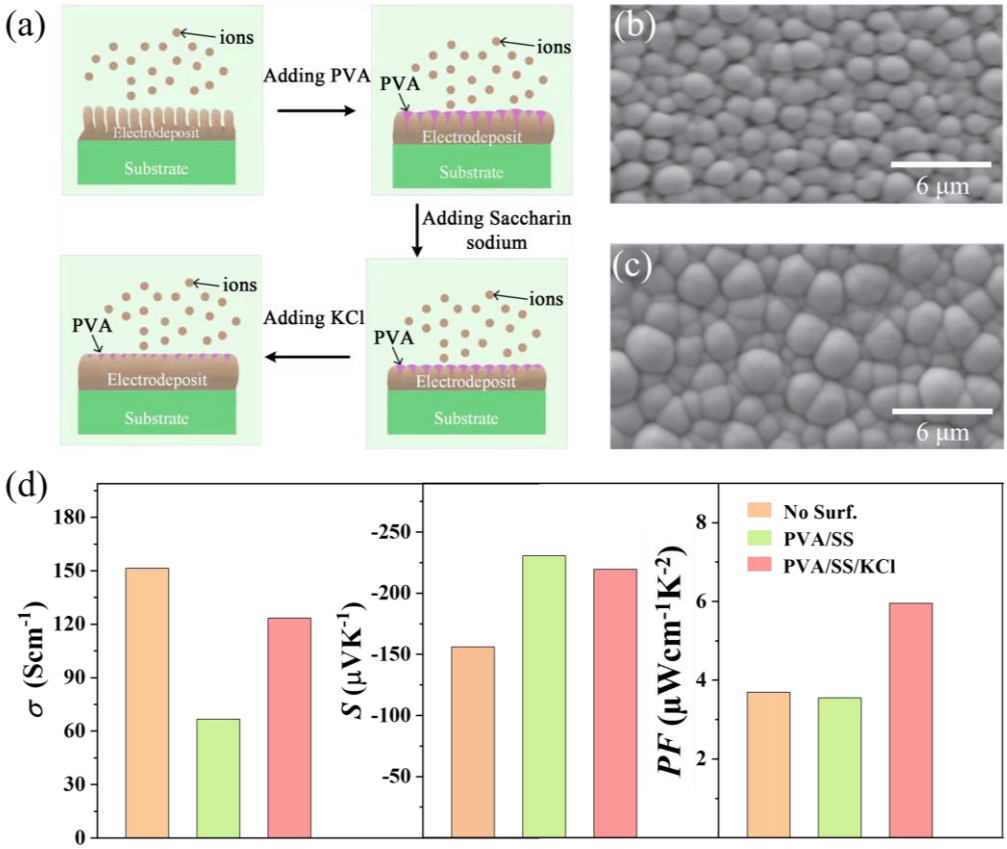

Figure 7. (a) Mechanism of co-operative interactions among multiple additives. Microstructure of deposited Bi_2Te_3 based film with addition of (b) PVA/SS and (c) PVA/SS/KCl. (d) RT TE properties of Bi_2Te_3 films with different additives [101]. Copyright 2021, IOP Publishing, Ltd. Reprinted with permission.

As shown in **Table 3**, most of the Bi_2Te_3 films deposited with surfactants revealed enhanced *S*. This is suggested to be due to the energy filtering effect, as the presence of surfactants would induce disordered or amorphous regions at grains boundaries, forming inter-grain energy barriers, which could filter out low energy charge carriers and allow high energy ones to transmit [102]. In addition, the hetero-interfaces between Bi_2Te_3 and organic surfactants might also induce interfacial potential barriers for energy filtering [103]. These could significantly improve *S* according to the formula [104]:

$$S = \frac{8\pi^2 k_B^2}{3eh^2} m^* T \left(\frac{\pi}{3n}\right)^{\frac{2}{3}} \quad (9)$$

where *h* is the Planck constant, k_B is the Boltzmann constant, m^* is effective mass of the carriers. To

conclude, it is difficult to realize a smooth, dense film with a high TE performance by using a single surfactant or additive, so, multiple additives are required. Further understanding of the influence of each additive and their combinations on the microstructure and TE properties of the films and the underlying mechanisms is of great significance for a cooperative effect on optimization of TE properties.

Table 3. TE properties and microstructures of Bi_2Te_3 films without/with different surfactants.

Surfactants	σ (Scm^{-1})	S (μVK^{-1})	PF ($\mu Wcm^{-1}K^{-2}$)	Grain-size (nm)	Preferential orientation	Ref.
No Surf.	320	−26	0.22	78	(0 1 8)	[88]
+PVP	4500	−22	2.20	48	(0 1 8)	[88]
+SDS	1480	−37	2.00	38	(0 1 8)	[88]
No Surf.	-	−13	-	39	(1 1 0)	[89]
+SL	333−769	−15	0.12	21	(1 1 0)	[89]
No Surf.	90	−73	0.46	-	(0 1 5)	[95]
+CTAB	110	−85	0.83	-	(1 1 0)	[95]
No Surf.	400	−65	1.70	-	(1 1 0)	[91]
+SLS	290	−82	1.90	-	(1 1 0)	[91]
+EDTA	140	−70	0.12	-	(0 1 5)	[105]

Notes: No Surf.: without Surfactants, +: add; PVP: polyvinyl pyrrolidone, SDS: sodium dodecyl sulfate, SL: sodium lignosulfonate, SLS: sodium laurylsulfate, CTAB: hexadecyl trimethyl ammonium bromide, EDTA: ethylene diamine tetraacetic acid. All TE properties were measured at room temperature except ***ref.*** 91 at ~ 105 °C.

2.5 Ionic concentration and temperature

Relative concentration: To ensure a precise stoichiometric ratio of Bi_2Te_3, C_{Bi}^{III}/C_{Te}^{IV} in the electrolyte usually lies in the range of between 2:1 and 2:3, with 1:1 and 3:4 being the most common

[95,105−108]. In any case, C_{Bi}^{III}/C_{Te}^{IV} should be over 2:3 because the Bi^{III} cation has a lower m and a more negative E_{onset} than the Te^{IV} cation, as discussed in the Mechanism section. As shown in **Figure 8(a)**, based on theoretical results [109], the conduction behavior of Bi_xTe_y transforms from n- to p-type at the atomic ratio of Bi:Te ≈ 37:63. With the decrease of $C_{Bi^{III}}/C_{Te^{IV}}$ in the electrolyte, the atomic ratio of Bi:Te decreases accordingly. Below Bi:Te ≈ 37:63, i.e. in a Te-rich product, some Te atoms occupy the Bi vacancies to form antisite defects $Te_{Bi}^{\cdot}$, thus introducing electrons. However, too small a value of $C_{Bi^{III}}/C_{Te^{IV}}$ can induce single-phase Te, producing a superlattice structure with Bi_2Te_3/Te [110−112]. With the increase in $C_{Bi^{III}}/C_{Te^{IV}}$ in the electrolyte, the atomic ratio of Bi:Te in the product increases correspondingly. Above Bi:Te ≈ 37:63, i.e. in Bi-rich products, some Bi atoms occupy Te positions to form antisite defects Bi_{Te}', introducing hole carrier. Consequently [113,114], the typical Bi-rich products are $(Bi)_{2m}(Bi_2Te_3)_n$, Bi_3Te_4, Bi_2Te and BiTe (**Figure 8(b)**) [115−119].

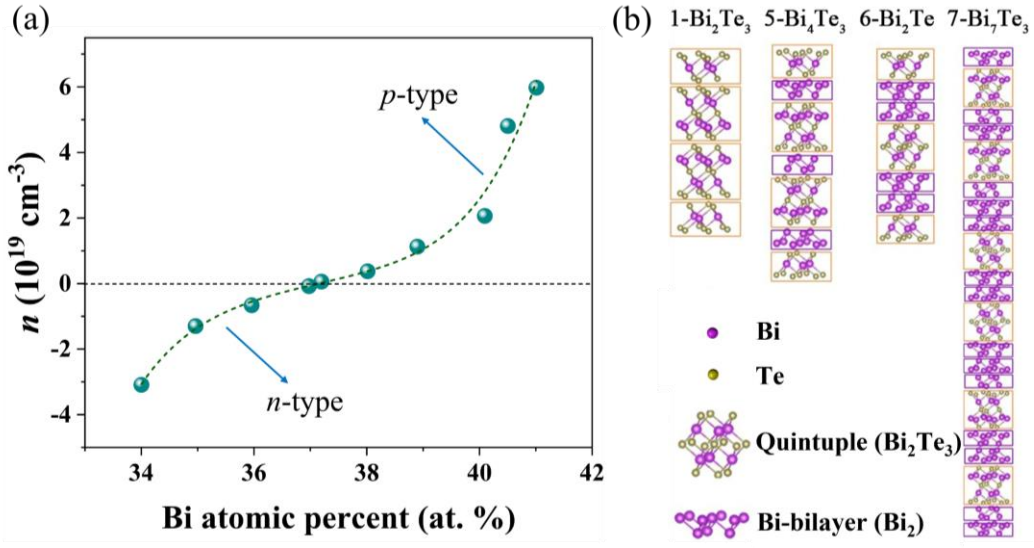

Figure 8. (a) Room temperature carrier concentration of Bi_2Te_3 as a function of Bi atomic percent [109,114]. (b) Atomic structure of Bi-rich products (Bi_2Te_3 quintuples are outlined by orange and Bi-bilayers by purple rectangles).

Absolute concentration: The absolute concentrations $C_{Bi^{III}}$ and $C_{Te^{IV}}$ can influence the

product compositions, as well as the $C_{Bi^{III}}/C_{Te^{IV}}$ ratio discussed above [120]. Because, Te^{IV} cations have a higher *m* and a more positive E_{onset} than Bi^{III} cations, small Te^{IV} concentrations can be exhausted quickly without timely supplement, thus giving rise to a great composition deviation. When the absolute ionic concentration is high enough, it can supplement the consumed ions in a timely fashion and maintain the stoichiometric ratio in the film (**Figure 9(a)**). As shown in **Table 4**, sample S3 was deposited with a higher absolute concentration than S2 at the same $C_{Bi^{III}}/C_{Te^{IV}}$ ratio, the composition of S3 is closer to the stoichiometric one (2/3), thus having a much higher *S* and *PF* (nearly double that of S2). Therefore, at a fixed $C_{Bi^{III}}/C_{Te^{IV}}$ ratio, the larger the absolute $C_{Bi^{III}}$ and $C_{Te^{IV}}$, the closer the film composition will get to stoichiometry (**Figure 9(d)**). However, this does not mean that the higher the absolute concentration, the better the TE performance will be, because the current density increases with ionic concentration. Too larger a current density can cause large crystal growth rate, thus leading to aggregated grains (**Figure 9(b,c)**) and consequent depression in μ [120].

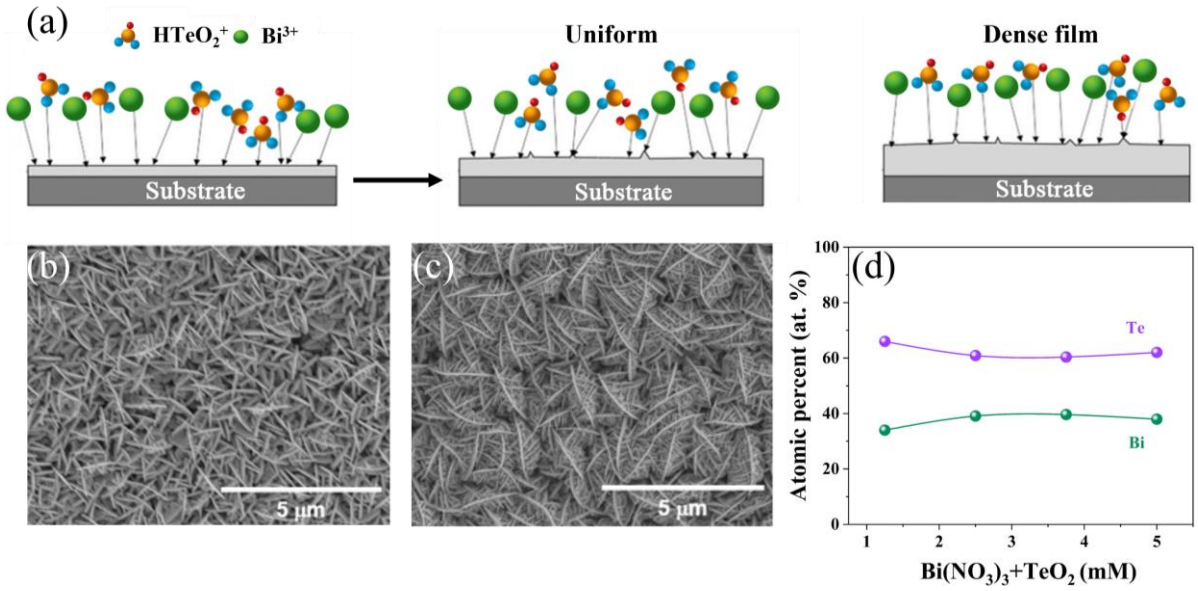

Figure 9. (a) Crystal growth mechanisms with high electrolyte concentration. Surface SEM images of the Bi_2Te_3 films deposited with ionic concentration of (b) 1.25 mM and (c) 3.75 mM. (d) Atomic percent of the Bi_2Te_3 films as functions of ionic concentration [120]. Copyright 2018, Elsevier. Reprinted with permission.

Temperature: As shown in **Figure 10(a)**, compared with the absolute ionic concentration, the electrolyte temperature has an opposite effect on the product composition. That is, at a fixed concentration, the higher the temperatures, the larger the composition deviation from the stoichiometric one [120]. Increasing the system temperatures can widen the ionic mobility gap between Te^{IV} and Bi^{III} cations. In this case the deposition rate of Bi^{III} cannot match with Te^{IV}, leading to dendrite growth and a loose structure (**Figure 10(c)**). The Bi atomic percent was also lowered with increasing temperatures (**Figure 10(d)**). Consequently, either the σ or S of sample S4 was severely reduced, leading to a low *PF*, two orders of magnitude lower than sample S1 (**Table 4**) deposited at a lower temperature, which exhibited a needle-like and denser structure (**Figure 10(b)**). Therefore, an electrolyte pair with a lower temperature and an appropriate ion concentration is more favorable for the TE properties of the Bi_2Te_3 film.

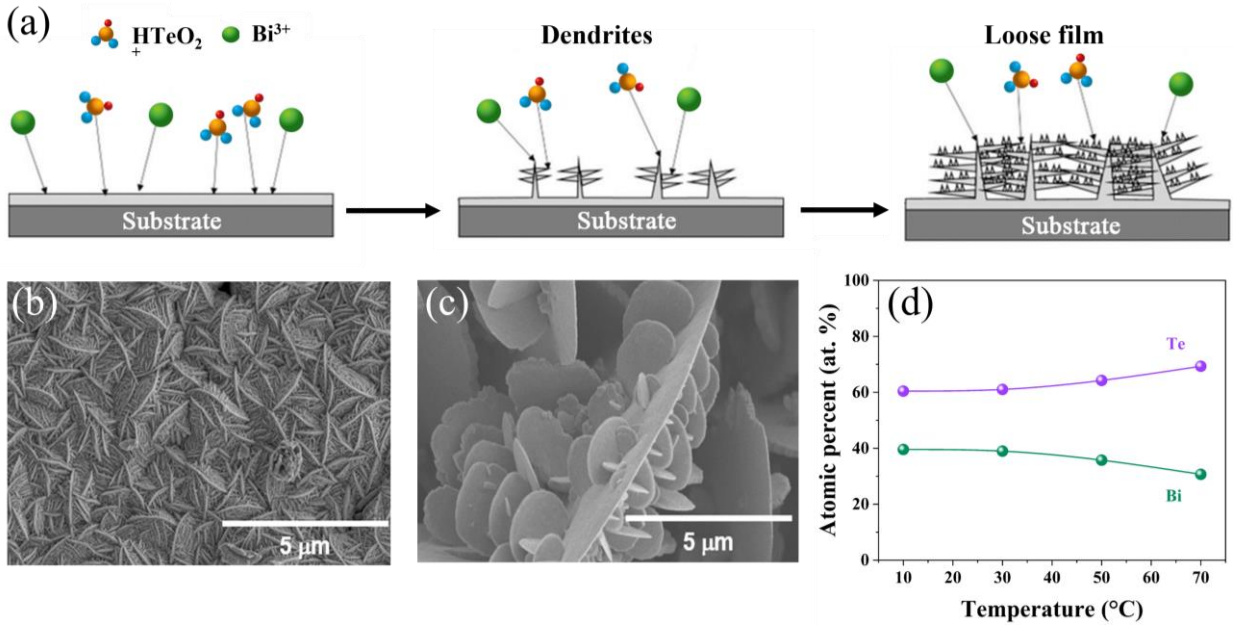

Figure 10. (a) Crystal growth mechanisms at high electrolyte temperature. Surface SEM images of the Bi_2Te_3 films deposited at electrolyte temperatures of (b) 10 °C and (c) 70 °C. (d) Atomic percent of the Bi_2Te_3 films as functions of electrolyte temperature [120]. Copyright 2018, Elsevier. Reprinted with permission.

Table 4. TE properties of Bi_2Te_3 films at different electrolyte temperatures and ionic concentrations [120].

No.	Composition	$C_{Bi^{III}}$ (mM)	$C_{Te^{IV}}$ (mM)	T (°C)	S (μVK^{-1})	σ (Scm^{-1})	PF ($\mu Wcm^{-1}K^{-2}$)
S1	Bi_2Te_3	1.00	1.50	10	−76	198	1.14
S2	$Bi_{1.7}Te_{3.3}$	0.50	0.75	30	−63	180	0.71
S3	Bi_2Te_3	1.25	2.50	30	−66	274	1.19
S4	$Bi_{1.5}Te_{3.5}$	1.00	1.50	70	−36	70	0.09

2.6 Oxidation prevention

Bi_2Te_3 could be oxidized during electrodeposition, as oxygen exist, which was revealed by XPS characterization in previous works [77,121]. However, the oxidation state was considered to be confined within nanometer-depth from the outer surface. Because it would attain a saturation after a long oxidation time, as oxygen atoms have to jump over the Te_1-Te_1 gap several times and this takes a long time. The formation of a 2 nm thick oxidation layer in ambient environment takes ~6000 hours [122]. The XPS is essentially a surface detection technology with a detection depth of several nanometers, it is therefore sensitive to the oxidation state of the surface layer with several tens of atoms in thickness. Since no phases of Bi_2O_3 or TeO_2 were observed in the XRD patterns, which has a detection depth of micrometers, the degree of oxidation is considered not high for electrodeposited Bi_2Te_3.

However, when Bi_2Te_3 is oxidized, oxygen atoms replace Te_2 in the quintuple layer (-Te_1-Bi-Te_2-Bi-Te_1-) and act as donors to increase the n, which is the primary reason for the Seebeck coefficient to decrease. Moreover, the defects induced by oxidation would enhance carrier scattering and thus reduce the μ [123−126], which would ultimately deteriorate The TE performance. Therefore, it is important to prevent oxidation during ED process. Some methods have already been developed, such as feeding

N_2 (nitrogen purging) into the electrolyte system to remove dissolved oxygen [37], annealing the film in a reduction atmosphere, e.g. N_2+5%H_2 gas, or Ar+5%H_2 gas [110,138]. In addition, based on thermodynamics, in the ternary system of Bi_2Te_3-Bi_2O_3-TeO_2, Bi exhibits the highest reactivity at equilibrium and Bi-Te shows the strongest bonding (−1.5 eV), followed by Bi – O (−1.0 eV) and Te – O (−0.8 eV). Therefore, the oxygen inward diffusion becomes considerably slower, when the surface terminates with Te [127]. One can try to deposit a protective layer of Te with a thickness of several atoms on the surface to hinder oxygen invasion, as well as to supplement Te volatilization in subsequent annealing.

3. Deposition mode

ED process of Bi_2Te_3 can adopt galvanostatic, potentiostatic or pulse mode. Before deposition, cyclic voltammetry (CV) scanning is required to obtain CV curves for analysis of the ED mechanism and proper range of the deposition potential or current density [128]. Ahead of ED process, the ionic concentration is uniform at all regions in the electrolyte. After initiation of ED, the ions in the interfacial layer on WE are the first depleted, thereby generating an ionic concentration gradient. The ions from bulk phase can diffuse into the vicinity of WE to supplement the ions depleted by the reaction. However, since the mass transfer rate cannot keep up with the deposition rate of the ions, the ionic concentration in the interfacial liquid layer on WE is further reduced, thus the concentration gradient is further increased [140,144]. As the reaction proceeds, the current density at WE continue to increase. The ion diffusion layer is continuously widened until the ions in the interfacial liquid layer on WE approach a lower concentration. When the quantity of the ions diffusing in is equal to the ions consumed on WE, a reaction equilibrium will be achieved. The polarization caused by the difference

between the ionic concentration in the interfacial layer and bulk phase, is termed concentration polarization [129]. The overpotential (η_{cp}) caused by this concentration polarization can be written as [129]:

$$\eta_{cp} = \frac{RT}{\alpha\xi F}\ln\frac{i_L}{i_L - i_K} \quad (10)$$

where, R is the molar gas constant, T is the thermodynamic temperature, α is the transfer coefficient, ξ is the moles of electrons transferred, F is the Faraday constant, i_L is the limiting current density, and i_K is the current density. With the increase of current density (i_K), the over potential generated by concentration polarization increases exponentially. Thus, concentration polarization is the main form of polarization under high current density, which can lead to a dendritic structure, rough surface and compositional deviations, as well as increased power consumption [130,131]. Therefore, devising methods to weaken the concentration polarization during ED of Bi_2Te_3 become a concern.

3.1 ***Potentiostatic/Galvanostatic mode***

As shown in **Figure 11(a)**, the early reported ED processes of Bi_2Te_3 were carried out by the potentiostatic or galvanostatic modes [132−136], which means that the applied potential or current density is fixed from the beginning to the end. However, the continuous deposition is unable to avoid the adverse effect of concentration polarization, thus forming small grain sizes, various orientations (**Figure 11(d)**) as well as deviated compositions [144,204,208]. These would eventually deteriorate the TE properties. Yamamuro et al. [137] prepared Bi_2Te_3 at an ED potential of −0.1 V by potentiostatic mode. A low σ of 79 Scm^{-1} was obtained, leading to a PF of only 0.3 $\mu Wcm^{-1}K^{-2}$. Mechanical stirring could reduce concentration polarization by enhancing mass transfer. Takashiri et al. [138] prepared Bi_2Te_3 at a current density of 1.8 mA cm^{-2} by galvanostatic mode under stirring. An improved σ of 930

Scm^{-1} was obtained, leading to a much higher *PF* of 4.20 $\mu Wcm^{-1}K^{-2}$. Although mechanical stirring could weaken the concentration polarization, the current density is concurrently increased, which in turn limits the weakening effect of concentration polarization.

3.2 Pulse mode

Currently, Bi_2Te_3 thin films are mostly prepared by pulse mode. Pulse mode involves two processes, i.e., Bi^{III} and Te^{IV} ions are reduced and deposited on the WE during the period t_{on}, when the current is turned on. The ionic concentration in the interfacial layer decreases rapidly and the polarization increases. During the period t_{off}, when the current is turned off, the ions in the electrolyte are driven by the chemical potential and diffuse into interfacial layer for compensation, thereby eliminating the concentration polarization (**Figure 11(b)**), and achieving a dense structure (**Figure 11(e)**). One can control the film thickness by repeating this cycle, where one cycle period $t = t_{on} + t_{off}$. Herein, $f = t_{off} / t_{on}$ is termed on-off ratio. Zhou et al. [139] studied the effect of different *f* on the TE properties of Bi_2Te_3. They found that the film morphology and composition is related to *f*. Since the *m* of Te^{IV} ions is greater than that of Bi^{III} ions, with the increase of t_{off}, more Te^{IV} ions can reach the interfacial layer compared to the Bi^{III} ions, thus Te atomic ration in the film increases with *r*. The composition at $r = 50$ is closest to the stoichiometric ratio (2/3). The film composition or morphology is not only affected by the magnitude of *f*, but also by *t*. At fixed *f*, the shorter the *t*, the better the TE properties. This is mainly attributed to the increased proportion of crystal grains with (1 1 0) orientation in the film.

For the cases where the mass transfer path is difficult, a multi-step pulse deposition model was proposed. Ning et al. [140] deposited TE cylinders with a diameter of 60 μm and a height of 200 μm

in an area of 1 × 1 cm^2, with a spacing of 200 μm between the cylinders. They used a glass plate with large-aspect-ratio through-holes as a template for the patterned ED of Bi_2Te_3. The conducting electrode located at the bottom of the holes, making the mass transfer path ultra-long. Therefore, ions consumed in the hole could not be supplemented in a timely fashion. To achieve a TE cylinder with uniform composition and regular microstructure, a three-step pulse deposition model was proposed, which introduced a relaxation step period T_0. The potential applied during T_0 corresponds to the oxidation peak of in the CV curve, which can dissolute the loose Bi_2Te_3 deposited, and then re-deposit in the next pulse cycle (**Figure 11(c)**). Finally, columnar Bi_2Te_3 with denser morphology was obtained than two-step pulse method (**Figure 11(f)**).

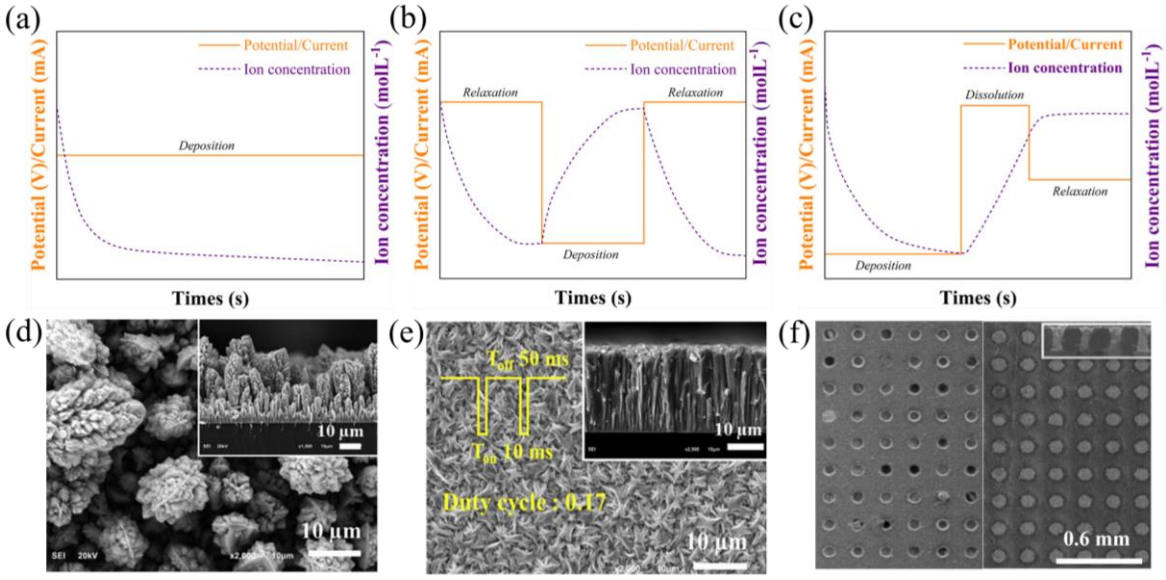

Figure 11. (a) Time dependencies of working potential/current (red line) and ion concentration in the interfacial layer on WE (dotted line) in potentiostatic/galvanostatic mode, (b) two-step pulse mode and (c) three-step pulse mode. (d) SEM images of the deposited Bi_2Te_3 films by potentiostatic and (e) pulse mode [208]. (f) Surface morphologies of the columnar Bi_2Te_3 deposited into thorough-holes by two-step (left) and three-step pulse (right) method [140]. Copyright 2008, Elsevier. Copyright 2020, MDPI. Reprinted with permission.

4. Electrodes

As mentioned in the Mechanism section, in order to eliminate the large error of the electrode potential caused by the polarization current, Bi_2Te_3 is usually deposited by the three-electrode system (an additional RE compared to the two-electrode system). In order to minimize the influence of CE polarization on WE, CE is required to be non-polarizable, of a small intrinsic resistance and a larger area than WE, as a small current density through WE can be achieved with a large area CE under the same current [46]. According to the Tafel equation [141]:

$$\eta_{ep} = \frac{RT}{\alpha nF} \ln \frac{i_K}{i^0} \tag{11}$$

where, η_{ep} is the overpotential generated by electrochemical polarization, i^0 is the exchange current density, which cannot be altered by polarization under a certain ionic concentration. Therefore, the smaller the i_K, the smaller the η_{ep}. During ED, the three electrodes are often placed at equal distance and in a common plane in general. According to the formula [142]: $E = \frac{\Delta\varphi}{L}$, where E, Δφ and L are the electric field, voltage gap and electrode distance respectively, it can be inferred that when the L decreases, the current density would increase based on the equation [143]:

$$i = \sum z_k F C_k \left(\frac{ezE}{6\pi\eta r_k}\right) \tag{12}$$

where, k indicates the k^{th} ion, C_k is its concentration, z_k is its ionic-charge number, $\frac{ez_kE}{6\pi\eta r_k}$ is its drift velocity, which leads to a loose structure and degraded TE properties as discussed above. However, for galvanostatic model, where the current density is constant, the effect of the electrode distance is neglectable [144]. The selection rules of WE, CE and RE and their functions in ED of Bi_2Te_3 will be discussed in detail in the next sections.

4.1 Counter electrode

The function of the CE is to form a loop with the WE to pass current. Usually, a stable material such as platinum (Pt) is used as a CE to ensure not to affect the reaction on WE. During the reaction progresses, the $C_{Bi^{III}}$ and $C_{Te^{IV}}$ in the electrolyte decreases, causing the film composition to gradually deviate from the stoichiometric ratio. In the final product, the Bi:Te atomic ratio varies with the thickness of the film, and the closer it is to the upper surface of the Bi_2Te_3 film, the greater its deviation from the stoichiometric ratio. To minimize the change in ionic concentration in the system, some researchers used Bi_2Te_3 rods as CEs [145]. In this way, as the reaction proceeds, Bi^{III} and Te^{IV} continuously to be added into the electrolyte, supplementing ionic consumption in the electrolyte. However, the molar ratio (2:3) of the ionized Bi^{III}:Te^{IV} can disturb the balanced concentration ratio initially set as discussed in *section* 2.5. Therefore, the stoichiometric ratio in the Bi_xTe_y needs to be pre-designed.

4.2 Reference electrode

The RE has a stable and well-known electrode potential and is used to precisely measure the varying potentials of the other electrodes. The reaction occurring at the RE should be a single reversible reaction, with a stable electrode potential and good reproducibility. Generally, a slightly soluble salt electrode is often used as a RE, since the hydrogen electrode is just an ideal one, which is not easy to realize. Of course, there are many kinds of REs. A suitable RE could be selected based on the type of electrolyte and pH value. As mentioned above, most of the electrolytes for Bi_2Te_3 deposition are acidic, so the commonly used REs are calomel electrode (SCE, mercury (Hg)/mercury chlorides (Hg_2Cl_2)/(saturated potassium chloride (KCl)) [146] or silver (Ag)/silver chloride (AgCl) electrode

(Ag/AgCl/(saturated KCl)) [147]. SCE is widely used in the organic solution system. However, it cannot be directly immersed in the organic solvent because it contains KCl-saturated aqueous solution. A salt bridge containing a specific nonaqueous solvent and supporting electrolyte is required to connect the RE to the electrolyte [148−150]. For alkaline systems or systems excluding Cl^-, Hg-Hg_2O electrodes or Hg-Hg_2SO_4 electrodes can be adopted. Ag-AgCl electrode is also widely used in non-aqueous solvents [75−77], but it should also be noted that the electrode shall not be in direct contact with the electrolyte, otherwise the potential can be changed.

4.3 Working electrode

The surface of WE are where the electrochemical reactions occur. There are a variety of WEs for ED of Bi_2Te_3, including smooth stainless steel (SSS) [134,151], conductive glasses [75,209], cuprum (Cu) [152], and platinum (Pt) [153]. In flexible electronic devices, TEDs are often integrated with other electronics on a circuit board. Insulating substrates are often adopted in order to prevent short circuits between devices in different regions. Ti, Cr, Au or Pt can be deposited on the insulating substrate as conductive seed layer before ED of Bi_2Te_3 [154−158].

Previous literature has not mentioned whether the type of the WE having a specific impact on the TE properties of the electrodeposited Bi_2Te_3 film, which would subsequently be transferred. However, it is reported that the Bi_2Te_3 film has weak adhesion to the SSS [16]. It can be easily peeled off from the substrate with epoxy tape, with no residue left on the stainless-steel sheet, which is beneficial for film transference. To enhance the adhesion between the seed-layer and the electrodeposited Bi_2Te_3, the seed layer could also be electrodeposited, as the resulting seed-layer surface could be rougher than the sputtered one.

5. Annealing treatment

Defects inevitably exist in the electrodeposited film because of the influence and limitations of deposition conditions and techniques. The crystal grains of the as-deposited film are small and there are enormous grain boundaries. Because intrinsic Bi_2Te_3 is an n-type semiconductor, its major carriers are electrons. Many grain boundaries and defects severely scatter electrons, reducing the σ of the material [159]. To further improve σ, the deposited film is usually subjected to an annealing treatment. Annealing refers to a heat treatment process in which the material is exposed to a high temperature for a certain duration, and then slowly cooled. This can increase the crystallinity and grain size of the material, reduce the defect density, and thereby increase σ (**Figure 12(a)**) [136].

5.1 Annealing regime

Due to the high saturated vapor pressure of Te, Te is easily volatilized out during annealing of Bi_2Te_3 [160−163], thus inducing a deviation in composition. Therefore, the Bi_2Te_3 annealing is generally carried out in a protective atmosphere, such as N_2, N_2 + 4% H_2, Ar + 4% H_2, or Te-rich one, to inhibit Te volatilization and oxidation as well [163,201,205,210]. In addition, the annealing temperature and duration can also have a great influence on properties. An annealing process which is too high in temperature or too long in duration can cause excess volatilization of Te from the Bi_2Te_3 film, causing an enlarged composition deviation as well as a loose and porous structure, degrading the TE properties of the film. Therefore, optimizing the annealing temperature and duration are of great significance for enhancing the TE properties.

Rashid et al. [136] annealed Bi_2Te_3 in Ar with annealing temperatures ranging from 200 to 300 °C for 2 to10 min. Their analysis showed that at lower annealing temperatures, the atomic ratio of Te in

the film increases with time, mainly due to the release of oxygen from the film, but the grain size of Bi_2Te_3 remained essentially unchanged. At high annealing temperatures, the Te atomic ratio in the film decreases rapidly due to its volatilization and the Bi_2Te_3 grain size doubled compared to that before annealing. Consequently, the carrier concentration decreased and the μ increased (**Figure 12(b)**). After a rapid thermal annealing process at 300 °C for 8 min, the S and PF of the Bi_2Te_3 film were improved significantly, the S was increased by about 3-fold, from –57 to –169.49 μVK^{-1} and the PF was improved over 6-fold, from 2.74 to 17.37 $\mu Wcm^{-1}K^{-2}$.

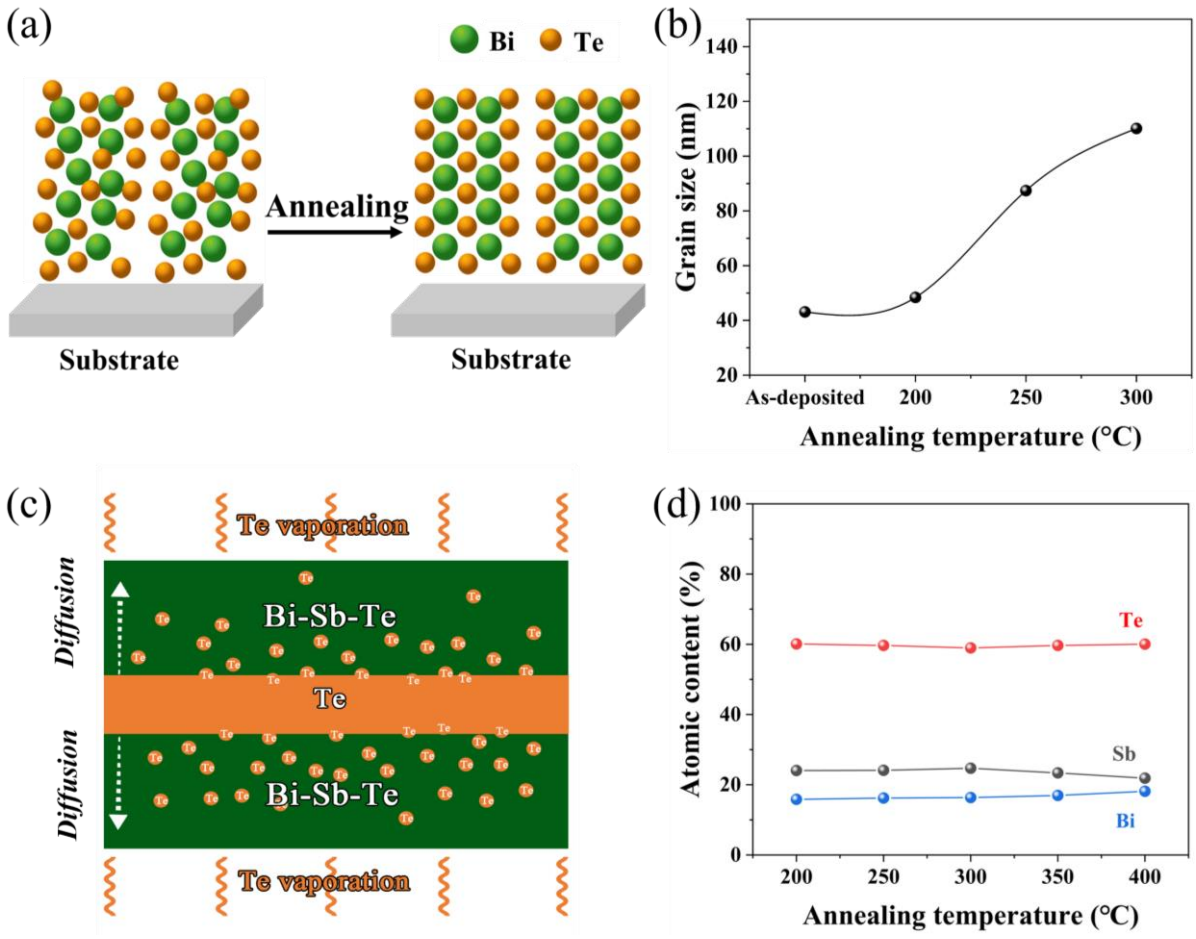

Figure 12. (a) A schematic diagram of defect alleviation or recrystallization by thermal annealing. (b) Annealing temperatures dependence of the average Bi_2Te_3 grain size [136]. (c) A supplementary Te layer supplementing the volatilized Te during annealing. (d) Annealing temperature dependence of the atomic composition in the as-deposited Bi-Sb-Te films [164].

5.2 Supplementary layer

It has been proven that appropriately increasing the annealing temperature and prolonging the duration can improve the film crystallinity, thereby increasing its σ [138]. However, as mentioned in section 5.1, both the annealing temperature and duration should be controlled to prevent Te escaping. To preserve Te at a higher annealing temperatures, Lal et al. [164] prepared a film with a $(Bi\text{-}Sb\text{-}Te)_x$-$Te_y$-$(Bi\text{-}Sb\text{-}Te)_z$ sandwiched structure by ED as shown in **(Figure 12(c))**. The film was then annealed at 250−400 °C in N_2 atmosphere. The Te interlayer can compensate the Te loss through diffusion during annealing, so as to maintain the stoichiometric ratio. As shown in **Figure 12(d)**, the Te atomic ratios of all films after annealing at different temperatures showed no remarkable changes.

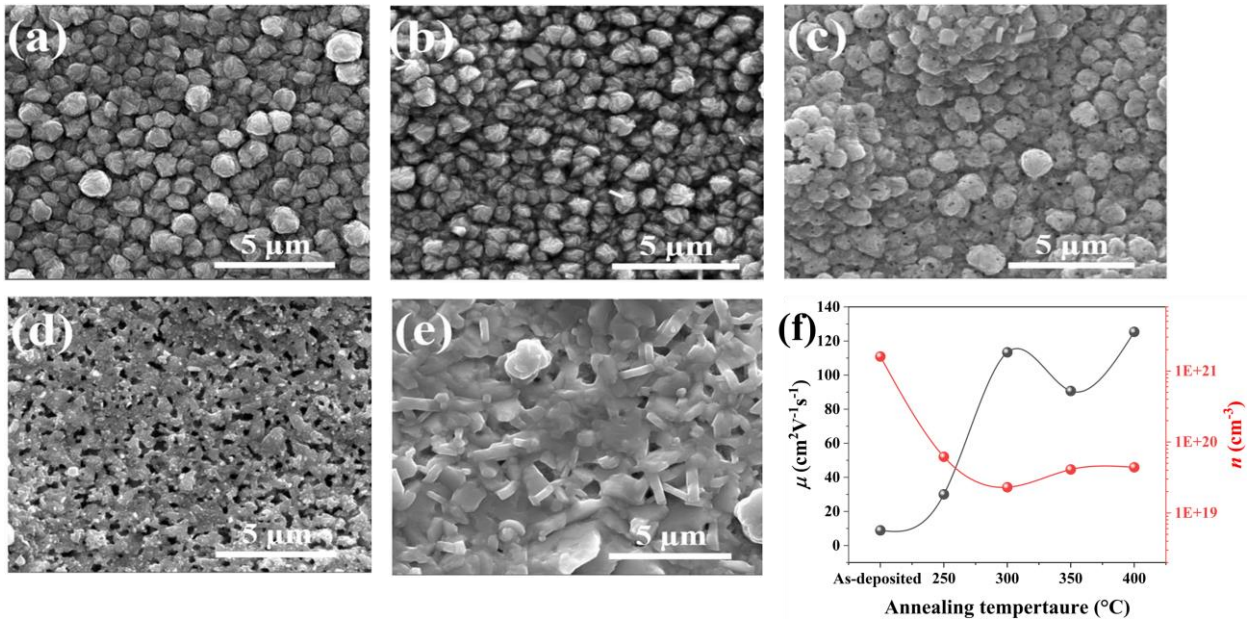

Figure 13. Surface SEM images of (a) as-deposited films and the annealed films at (b) 250 °C, (c) 300 °C, (d) 350 °C, and (e) 400 °C. (f) Annealing temperature dependencies of μ and n of all films [164]. Copyright 2019, Amer Inst Physics. Reprinted with permission.

With the annealing temperature increasing from 250 to 300 °C, the grains grew up with decreased grain boundary density (**Figure 13(a−c)**), so that the μ increased (**Figure 13(f)**). However, a further

increase in annealing temperature to 350 °C caused increasing porosity due to severe Te evaporation (**Figure 13(d)**), thus the μ decreased correspondingly. When the annealing temperature reached 400 °C, the grains were fully interconnected, the μ was therefore improved again (**Figure 13(e,f)**). Due to the reduction of antisite defects, the n of the annealed films was reduced to 2–6 × 10^{19} cm^{-3}, which was two orders of magnitude lower than the original 1.58 × 10^{21} cm^{-3}. This reduction in n then led to an increase in the S. The TE properties of the sample annealed at 350 ℃ for 1 h were the best with an optimized PF of 2.40 μW $cm^{-1}K^{-2}$.

5.3 Barrier layer

When the deposited Bi_2Te_3/substrate as a whole is annealed directly without transference, some impurity atoms from the substrate can diffuse into the Bi_2Te_3(**Figure 14(a)**). The induced defects could cause carrier scattering, thereby degrading TE properties of the material [165,166]. Depositing a diffusion barrier layer between the substrate and Bi_2Te_3 has been proved to be an effective way to inhibit the diffusion of impurity-atom into Bi_2Te_3 (**Figure 14(b)**). The selection of the diffusion barrier material should consider the following [167−169]: firstly, the barrier material and the adjacent material should be thermodynamically stable; secondly, the thermal expansion coefficients of the barrier material and the adjacent material should be matched; thirdly, the barrier layer should be as thin as possible while maintaining thermal stability with the adjacent material; lastly, the lower the surface roughness of the diffusion barrier layer, the stronger the bonding between the diffusion barrier layer and the adjacent layers. Common barrier materials for Cu, SSS and Se electrodes in TEDs include TiN [169−171], Ta [172,173], and TaN [174,175].

Eguchi et al. [176] deposited a TiN barrier layer with a thickness of 0.15 μm on a SSS by DC

magnetron sputtering, followed by ED of Bi_2Te_3 and annealing in Ar + 4% H_2 atmosphere. As shown in **Figure 14(c),** Bi_2Te_3 deposited on WE without a diffusion barrier layer exhibits Fe and Ni impurity after annealing, while Bi_2Te_3 deposited on WE with a barrier layer shows no Fe and Ni impurity after annealing. Thereby, the σ of the Bi_2Te_3 with a barrier layer is 4 times higher than the one without a barrier layer, as shown in **Figure 14(d),** leading to a 4 × increase in *PF* (reaching 4.4 $\mu Wcm^{-1}K^{-2}$).

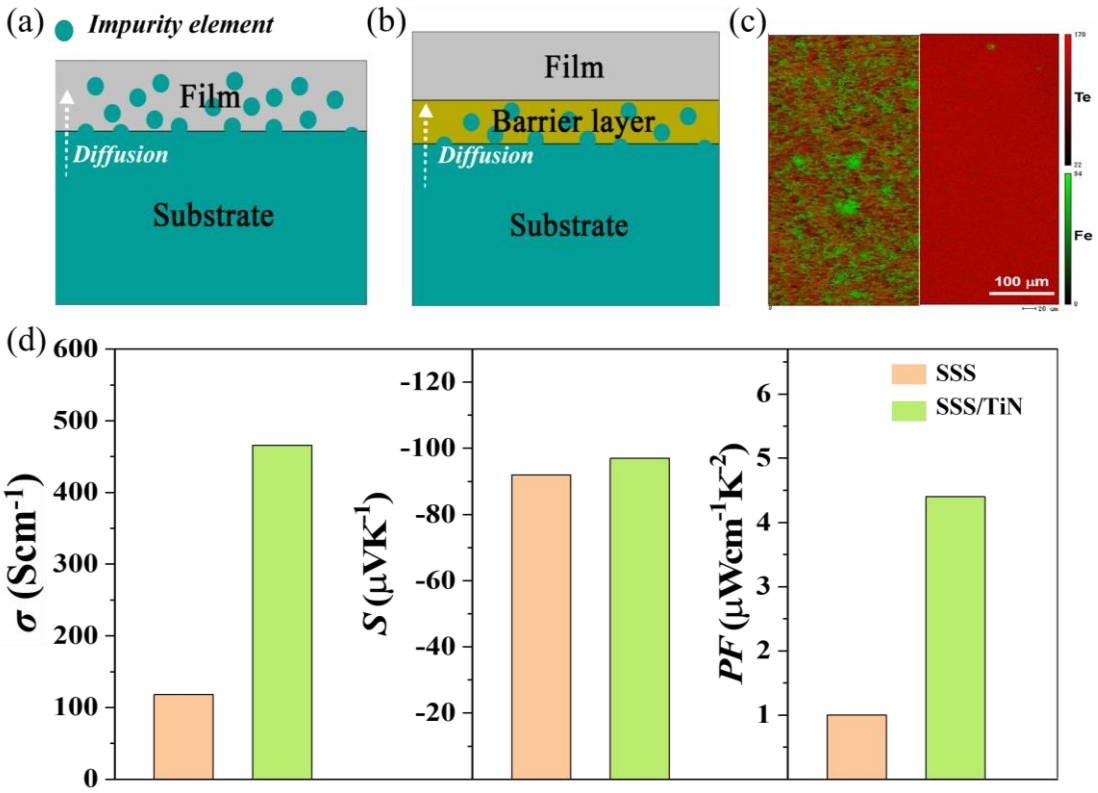

Figure 14. (a) Schematic diagram of impurity diffusion from substrate into the film and (b) being impeded by a barrier later during annealing. (c) Te and Fe elemental color mapping of the film deposited on bare SSS substrate (left) and SSS/TiN substrate (right). (d) RT TE properties of the Bi_2Te_3 films deposited on the bare SSS and TiN-coated SSS substrates [176]. Copyright 2020, Elsevier. Reprinted with permission.

6. Nanocomposite and ternary alloy

Although Bi_2Te_3 is the material with the best TE properties near RT, the TE conversion efficiency

is still far lower than that of traditional mechanical generators, so improving the TE properties of Bi_2Te_3 either at its bulk or film state remains a focus. Currently, two strategies are used to improve the TE properties of Bi_2Te_3 during ED processing: nanocomposites and ternary alloys.

6.1 *Nanocomposite*

The term "nanocomposite" refers to a composite material within which at least one phase is of nanometer dimensionality. A nanoscale dispersed phase can strongly scatter phonons with a wavelength similar to its dimension, and through this mechanism significantly reduce the phonon thermal conductivity (κ_l), thus boosting *ZT* [177,180,184]. In some cases, if the bandgap energy of the second phase is different from that of Bi_2Te_3, a potential barrier at the hetero-interfaces can be induced, which will scatter low energy carriers, thus enhancing *S* and improving the TE properties (**Figure 15(a,b)**) [145,178,179,]. In addition, some incorporated dispersed phases, such as carbon nanotubes (CNT), can increase the electron transport path to improve the σ of the material (**Figure 15(c)**), in which case the overall *PF* can be improved [212](**Figure 15(d)**).

Nguyen et al. [145] added PVP solution dispersed with Au nanoparticles into the electrolyte, and prepared Au/Bi_2Te_3 composites by electrodeposition. The nanocomposite containing 5% Au nanoparticles with a diameter of 5 nm showed the highest *ZT* (~ 0.62) at RT, ~ 40 times higher than that without Au nanoparticles. Au nanoparticles were introduced to generate a charge transfer between Au and the host phase, resulting in a metal-semiconductor interface band bending. As shown in **Figure 15(b)**, this behavior forms an energy-dependent barrier (ΔE_g), which acts as a filter for scattering low-energy electrons. Only high-energy electrons can pass the barrier, while low-energy electrons are scattered on the barrier at the interface. And due to the introduction of defects and/or grain boundaries,

the thermal conductivity of the lattice is reduced by phonon scattering, thereby improving the overall TE properties of the material.

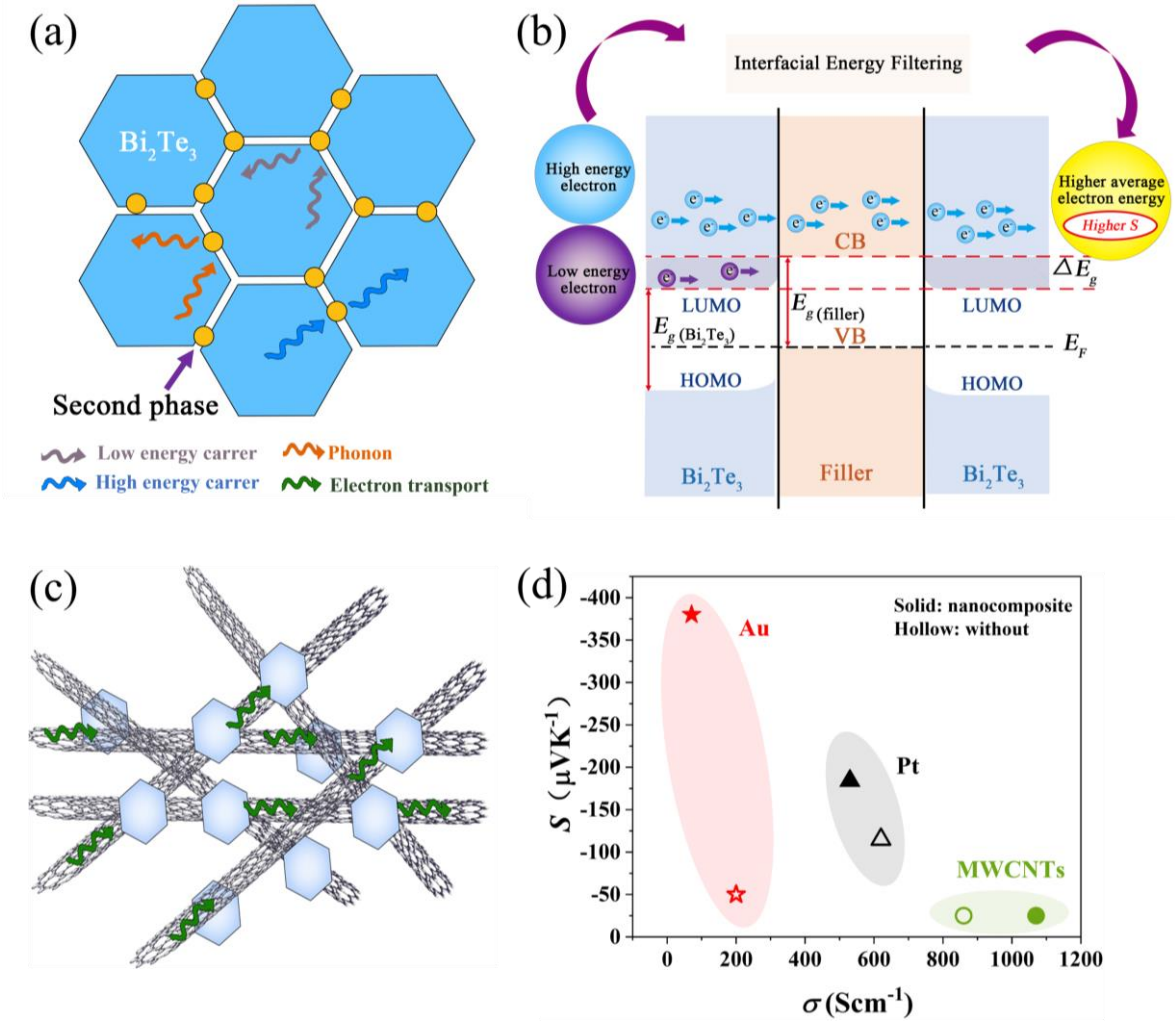

Figure 15. (a) Schematic diagram of the phonon and electron transport in nano-particle dispersed composite system, (b) energy filtering effect, (c) CNT dispersed composite system and (d) TE properties of the Bi_2Te_3 based nanocomposite with different second phases [145,184,212].

Wang et al. [180] introduced SiC nanoparticles with an average diameter of 60 nm into the Bi_2Te_3 film by electrodeposition. Because nano-SiC can optimize the *n*, the TE properties are the best at a mass content of 3.74 % SiC. The most representative non-metal second phases are carbon materials such as graphene and CNTs [[181−184]. Due to their superior σ and flexibility, they can be introduced as nano second-phases into Bi_2Te_3 films to improve both *ZT* and mechanical properties [184,185]. For

example, Xu et al. [184] embedded carbon nanotubes (MWNTs) into Bi_2Te_3 thin films by potentiostatic deposition. The addition of MWNTs increased the migration path of carriers and effectively improved the μ (**Figure 15(c)**). At a content of ~ 4.7 %, the σ increases from 860 Scm^{-1} to 1070 Scm^{-1}.

6.2 *Ternary alloy*

Here the term "solid solution alloy" refers to the introduction of an isoelectronic defect atom into the crystal lattice. Due to the induced mass and stress field fluctuations among host and guest atoms, a strong point defect scattering occurs, thereby reducing the κ_l consequently [186,187]. For the Bi_2Te_3 based solid solution, typically, Sb_2Te_3 and Bi_2Se_3 can be alloyed with Bi_2Te_3 to form p-type ($Bi_{2-x}Sb_xTe_3$) and n-type ($Bi_2Te_{3-x}Se_x$) materials, respectively **(Figure 16(a))** [188,189]. The energy band structure is not remarkably modified due to the introduction of a similar valence electronic structure, while the κ_l can be effectively reduced, and the *ZT* value could thus be improved [190−192].

P-type $Bi_{2-x}Sb_xTe_3$: Bi and Sb are the adjacent elements in Group VA of the periodic table, which have similar electronegativity and atomic radii (**Table 5**), so Sb can substitute Bi atoms in the Bi_2Te_3 lattice to form $Bi_{2-x}Sb_xTe_3$. However, compared with Bi, Sb atom has an atomic radius and electronegativity closer to Te atom, thus the energy required to occupy the site of Te is lower, and it is easy to form anti-site defects Sb'_{Te} (**Figure 16(b)**), thereby inducing holes and making $Bi_{2-x}Sb_xTe_3$ a strong p-type semiconductor [109]. Due to the large mass difference between Bi and Sb, the κ_l can be effectively suppressed and because of small differences in their electronegativity and atomic radius, the μ can be maintained. Moreover, the *n* can be fine-tuned by the quantity of Sb'_{Te}. Therefore, it can be regulated by *x* for a maximized *S* which peaks at $x = 1.5$ [193]. It is thus intriguing to realize such composition by ED. One of the key issues confronted is the ultra-low solubility of Sb in most solvents.

Tartaric acid (TA), ethylene diamine tetraacetic acid（EDTA）and citric acid (CA) have been reported to act as a chelating agents of Sb^{III} to increase its solubility [194,195]. Kang et al. [183] obtained $Bi_{2-x}Sb_xTe_3$ by pulse deposition in CA added electrolyte. The reaction formula of $Bi_{2-x}Sb_xTe_3$ can be expressed as [201]:

$$HTeO_2^+ + 3H^+ + 4e^- \rightarrow Te^0 + 2H_2O \quad (13)$$

$$3Te^0 + 2(1-x)Bi^{3+} + x[Sb_2(C_4H_4O_6)_2]^{2+} + 6e^- \rightarrow (Bi_{1-x}Sb_x)_2Te_3 + 2x(C_4H_4O_6)^{2-} \quad (14)$$

Due to the difference between m and E_{onset} of Bi^{III}, Sb^{III} and Te^{IV} ions, the optimal stoichiometric ratio in the deposited film is not easy to be realized [195]. The final product was measured to possess a composition of $Bi_{0.45}Sb_{1.22}Te_{3.33}$ and a mean grain size as low as 13 nm. We think this could be due to a large overpotential caused by the extra energy needed to break the $[Sb_2(C_4H_4O_6)_2]^{2+}$ complex. Therefore, the μ was heavily depressed, leading to a σ as low as 70 Scm^{-1}, which is 1−2 orders of magnitude lower than most Bi-Te based films. A PF of 1.5 $\mu Wcm^{-1}K^{-2}$ was obtained, which is far less than expected and even lower than most binary films (**Table 6**).

N-type $Bi_2Te_{3-y}Se_y$: Because the radius and electronegativity of a covalent Bi atom is quite different from Se (**Table 5**), the formation energy of an antisite defect in Bi_2Se_3 is large. Thus, the generation of antisite defects is restricted. Moreover, since the vapor pressure of Se is large, it is easy for it to escape from the lattice to form Se vacancies (**Figure 16(b)**) ($V_{Se}^{\cdot\cdot}$) in the crystal lattice and ionize electrons, thus making $Bi_2Te_{3-y}Se_y$ an n-type semiconductor [196,197]. Se doping is able to split the energy band of Bi_2Te_3, increase the density of states near the Fermi energy, and widen the forbidden band-gap [198], which can suppress the initiation of intrinsic excitation, thus enhancing TE performance at higher temperatures. The composition with the best TE properties has been proven to be $Bi_2Te_{2.7}Se_{0.3}$ [199,200]. Ma et al. synthesized $Bi_2Te_{3-y}Se_y$ thin film using potentiostatic deposition

on Au-coated silicon substrates in aqueous acidic solutions at RT [201]. The corresponding formula is:

$$(1-y)\,HTeO_2^{+} + ySeO_3^{2-} + (3+3y)H^{+} + 4e^{-} \rightarrow Se_{1-y}Te_y + (2+y)H_2O \quad (15)$$

$$2Bi^{3+} + 3Se_{1-y}Te_y + 6e^{-} \rightarrow Bi_2Te_{3-y}Se_y \quad (16)$$

As shown in Table 6, the final composition is $Bi_{1.9}Te_{2.8}Se_{0.3}$. The composition deviation leads to a decreased S of −65 μVK^{-1}, which is 1/3 of that of bulk $Bi_2Te_{2.7}Se_{0.3}$ (−208 μVK^{-1}) [202]. Due to the electronic scattering by inevitable impurities and grain boundaries, the μ was reduced, thus ultimately reducing the σ [59−61,203]. The optimal PF was 1.7 μWcm^{-1}K^{-2}, which was not as competitive as binary ones.

Table 5. Boiling point, electronegativity, covalent radius, and atomic mass of Bi, Sb, Te and Se [109].

Elements	**Bi**	**Sb**	**Te**	**Se**
Electronegativity	2.02	2.05	2.10	2.55
Covalent radius (Å)	1.46	1.40	1.36	1.16
Atomic mass	208.98	121.75	127.60	78.96
Boiling point (°C)	1664	1587	988	958
E_V	E_V(Sb-Te)＞E_V(Bi-Te)＞E_V(Bi-Se)			
E_{AS}	E_{AS}(Bi-Se)＞E_{AS}(Bi-Te)＞E_{AS}(Sb-Te)			

Note: E_V: the formation energy of anion vacancies (e.g., E_V(Sb-Te): the energy to form $V_{Te}^{\cdot\cdot}$ in Sb_xTe_y); E_{AS}: the formation energy of antisite defect (e.g., E_{AS}(Bi-Se): the energy to form antisite defect Bi_{Te}' in Bi_xTe_y).

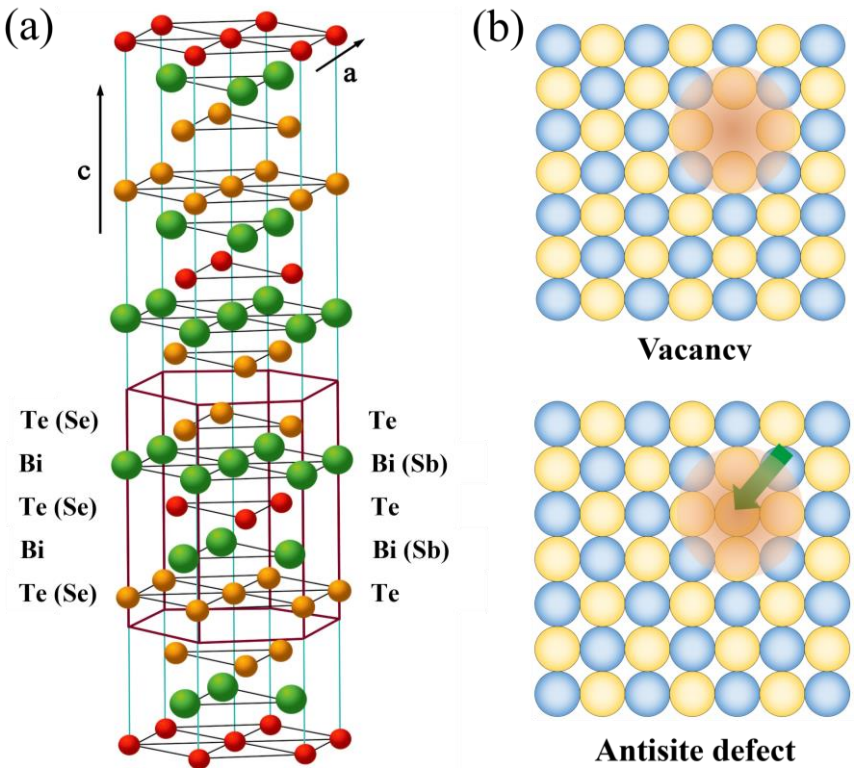

Figure 16. (a) Crystal structure of $Bi_{2-x}Sb_xTe_3$ or $Bi_2Te_{3-x}Se_x$. (b) Schematic diagram of vacancy and antisites defect. (The shaded represents the induced stress).

The TE properties of the electrodeposited Bi_2Te_3-based ternary alloys to date are still lower than expected, which is mainly attributed to the composition deviation from the optimal $Bi_{0.5}Sb_{1.5}Te_3$ or $Bi_2Se_{2.7}Te_{0.3}$. Recent researches have tried to regulate the film composition by manipulating the ionic concentration, concentration ratio of different ions, as well as the deposition potential and deposition mode. Precise control of the composition has been realized for binary Bi_2Te_3, but it is challenging for Bi_2Te_3-based ternary alloys, which are complex systems with three ionic species of different mobilities. In order to achieve the optimal composition in the same electrolyte system, future work is suggested to select appropriate chelating agents to form different chelates structures with Bi^{III}, Te^{IV}, Sb^{III}, and Se^{IV} ions to manipulate their mobilities, which can add a dimension for composition regulation to ionic concentration adjustment.

Table 6. ED Synthesis of Bi_2Te_3 films and their TE properties.

Composition	Mode	Annealing regime	σ (Scm^{-1})	S (μVK^{-1})	PF ($\mu Wcm^{-1}K^{-2}$)	Ref.
Bi_2Te_3	Galvanostatic	Ar + 5% H_2, 300 °C, l h	930	−67	4.2	[138]
Bi_2Te_3	Galvanostatic	-	2200	−61	8.2	[128]
Bi_2Te_3	Potentiostatic	-	270	−63	1.1	[120]
Bi_2Te_3	Potentiostatic	N_2 + 5% H_2, 160 °C, 0.5 h	670	−70	3.3	[110]
Bi_2Te_3	Potentiostatic	-	200	−50	0.5	[204]
Bi_2Te_3	Potentiostatic	N_2, 250 °C, 1h	500	−110	6.0	[204]
Bi_2Te_3	Potentiostatic	Ar + 5% H_2, 250 °C, 1h	810	−80	5.2	[205]
Bi_2Te_3	Pulse	-	330	−80	2.1	[206]
Bi_2Te_3	Pulse	-	520	−80	3.3	[204]
Bi_2Te_3	Pulse	N_2, 250 °C, 1 h	670	−150	15	[204]
Bi_2Te_3	Pulse	-	690	−146	14.7	[16]
Bi_2Te_3	Pulse	-	2000	−89	20.1	[140]
$Bi_2Te_{2.6}Se_{0.3}$	Potentiostatic	-	290	−89	2.3	[210]
$Bi_{1.9}Te_{2.8}Se_{0.3}$	Potentiostatic	-	400	−65	1.7	[154]
$Bi_{1.88}Te_{2.70}Se_{0.42}$	Potentiostatic	-	520	−50	1.3	[207]
$Bi_{2.00}Te_{2.39}Se_{0.77}$	Potentiostatic	-	70	−62	0.3	[208]
$Bi_2Te_{2.7}Se_{0.5}$	Pulse	-	90	−92	0.8	[209]
$Bi_{2.00}Te_{2.71}Se_{0.15}$	Pulse	-	1340	−93	11.5	[210]
$Bi_{2.00}Te_{2.71}Se_{0.15}$	Pulse	N_2 + 5% H_2, 200 °C, 1 h	1710	−106	19.2	[210]
$Bi_{0.22}Sb_{1.48}Te_{3.30}$	Potentiostatic	-	80	119	1.1	[211]
$Bi_{0.4}Sb_{1.3}Te_{3.3}$	Potentiostatic		20	~105	~0.3	[201]
$Bi_{0.4}Sb_{1.4}Te_{3.2}$	Potentiostatic	Ar, 130 °C, 2 h	90	~160	~2.3	[201]
$Bi_{0.45}Sb_{1.22}Te_{3.33}$	Pulse	-	70	150	1.5	[207]
$Bi_{0.8}Sb_{1.2}Te_3$	Pulse		910	11	0.1	[164]
$Bi_{0.83}Sb_{1.17}Te_3$	Pulse	N_2, 350 °C, 1 h	270	91	2.3	[164]
$Cu_{0.64}Bi_{1.11}Te_3$	Potentiostatic	-	399	−275	30.2	[37]
Bi_2Te_3	Potentiostatic	-	200	−50	50.0	[145]
Bi_2Te_3/Au	Potentiostatic	-	71	−380	10.3	[145]
Bi_2Te_3	Pulse	N_2, 250 °C, 2 h	620	−115	8.2	[212]
Bi_2Te_3/Pt	Pulse	N_2, 250 °C, 2 h	530	−184	18.0	[212]
Bi_2Te_3	Potentiostatic	N_2, 250 °C, 2 h			~2.0	[180]
Bi_2Te_3/SiC	Potentiostatic	N_2, 250 °C, 2 h	-	-	~2.5	[180]
Bi_2Te_3	Potentiostatic	N_2, 250 °C, 2 h	860	-	-	[184]
Bi_2Te_3/ MWNTs	Potentiostatic	N_2, 250 °C, 2 h	1070	-	-	[184]

7. Device integration

With the rapid development of integrated circuits, the power consumption of microelectronic systems continues to decrease, for which micro-power supply with high power density and long lifespan is urgently needed. Microscale TEGs (micro-TEGs) can realize in-situ power supply by utilizing environmental temperature difference, thereby holding a great potential for applications in wearable electronics, internet-of-things, etc. In addition, with the fast development of high-power density electronic components, precise temperature control and actively local cooling technologies are also stringently needed. Microscale TECs (micro-TECs) possess unique merits, such as a short cooling response-time in scale with their dimensions, a high heat flux handling capability and being compatible with conventional CMOS fabrication [213]. Therefore, micro-TECs have found their particular applications in areas of thermal management of photonic integrated circuits, microelectronic chips as well as heat/light sensors, etc. [214,215].

Since bulk thinning is not suitable for low-cost and scalable TED fabrications, a variety of preparation techniques of Bi_2Te_3, such as physical sputtering, ion etching, ED, etc., have been attempted to be combined with the TEG processes [216−220]. Among them, ED has advantages such as fast deposition rate, depositing-region-selective, less raw-material waste, compatible to CMOS based micro-fabrications, and most importantly, it can be used to make Bi_2Te_3 films as thick as several tens of μm [221]. Typical micro-TEDs process includes steps such as ED of Bi_2Te_3, transference, structure design and interconnection [222]. In this part, we would mainly discuss the recent processes that can facilitate the scalability of TED as well as structure optimization strategies for higher device performance (**Table 7**).

7.1 TED structure and processing

Micro-TEDs can be classified into the in-plane type when thermal flow is in parallel with the substrate and the cross-plane type when thermal flow is vertical to the substrate. The film structure of in-plane type TEGs is shown in **Figure 17(a)**, where the heat flow is in parallel to the sustaining substrate. It has long TE legs, thereby facilitating the establishment of a large temperature difference. However, due to heat loss through substrate, high internal resistance, its output energy density is low.

To address these issues, Trung et al. [223] designed a Y-shaped structure micro-TED as shown **Figure 17(b)**. The TE legs are parallelly aligned on the same plane, with vertically aligned heat guide bonded on junctions of p- and n-legs. Although the overall heat flow is vertical to the substrate, the heat flow through the TE films is parallel to the substrate. Therefore, it is still essentially an in-plane micro-TEG. As shown in **Figure 17(c)**, the fabrication of the Y-type micro-TEG is clearly illustrated. Both sides of the Y-type structure were encapsulated in polydimethylsiloxane (PDMS), which has a good flexibility and high thermal resistance. Multiple layers of Ti-TiN-Au-Cu were sputtered between the electrodeposited Bi_2Te_3 legs and Cu electrode, to reduce their contact resistance, and to prevent the diffusion of Cu into Bi_2Te_3, as well as to minimize the mismatch of the thermal expansion coefficient between the Cu electrodes and Bi_2Te_3. The Y-type structure could ensure long TE legs as well as a large film thickness, thereby establishing a larger temperature gap and smaller internal resistance. When attaching it to human skin at ambient temperature of 15 ℃ under free convection, the Y-type micro-TEG could maintain a temperature gap of ~ 6 °C, much larger than the conventional structure (~ 2.2 °C). Consequently, the Y-type micro-TEG could output an open circuit voltage (V_{oc}) of 56 mV and a maximum power density of 3 μW cm^{-2}. However, as the heat collection area is restricted by the area of the exposed heat guide, a large amount of heat from the heat sources is impeded by the PDMS,

the power density could be further improved by structure optimization (e.g. a V-shaped heat guide to increase heat contact areas) in future works.

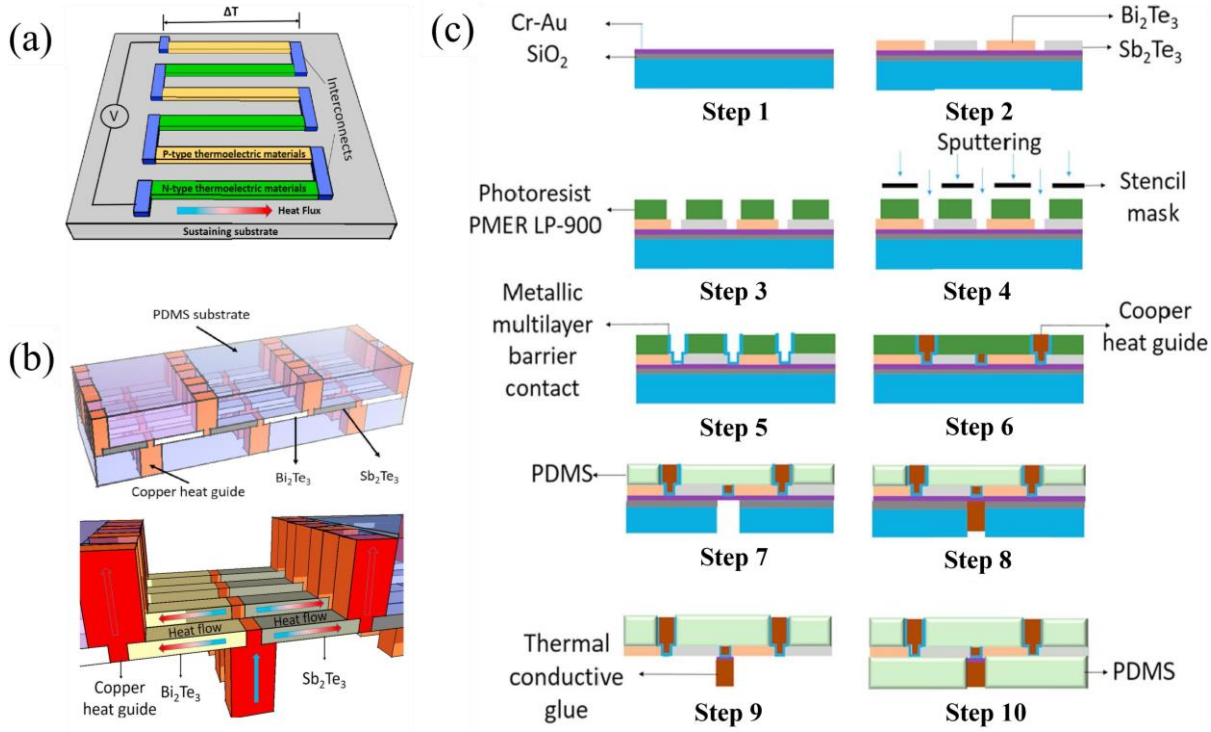

Figure 17. (a) Structure of conventional in-plane type micro-TEDs. Structure of the Y-type micro-TEDs (b) and its fabrication processes (c). Step 1: Depositing SiO_2-Cr-Au seed layer on silicon substrate. Step 2: Electrodeposition of Bi_2Te_3. Step 3: Photolithography. Step 4 and Step 5: Deposition of multilayers of barrier metal contacts of Ti-TiN-Au-Cu. Step 6: Deposition of copper heat guides. Step 7: PDMS refilling and Si-SiO_2 removing. Step 8: Screen printing of thermal conductive glue. Step 9: Back side etching. Step 10: PDMS refilling [223]. Copyright 2017, Elsevier. Reprinted with permission.

Compared with the in-plane type micro-TEDs, cross-plane type micro-TEDs are more widely used due to a larger output power density. Typically, a template with a pre-designed micro-pillared structure was obtained by patterning glass/silicon with laser ablation or photolithography, which would act as a WE for Bi_2Te_3 electrodeposition. By interconnecting and bridging, a cross-plane micro-TED would be made. The advantage is it has a large heat-collecting area, thereby ensuring a high energy

harvesting efficiency and power output [224,225].

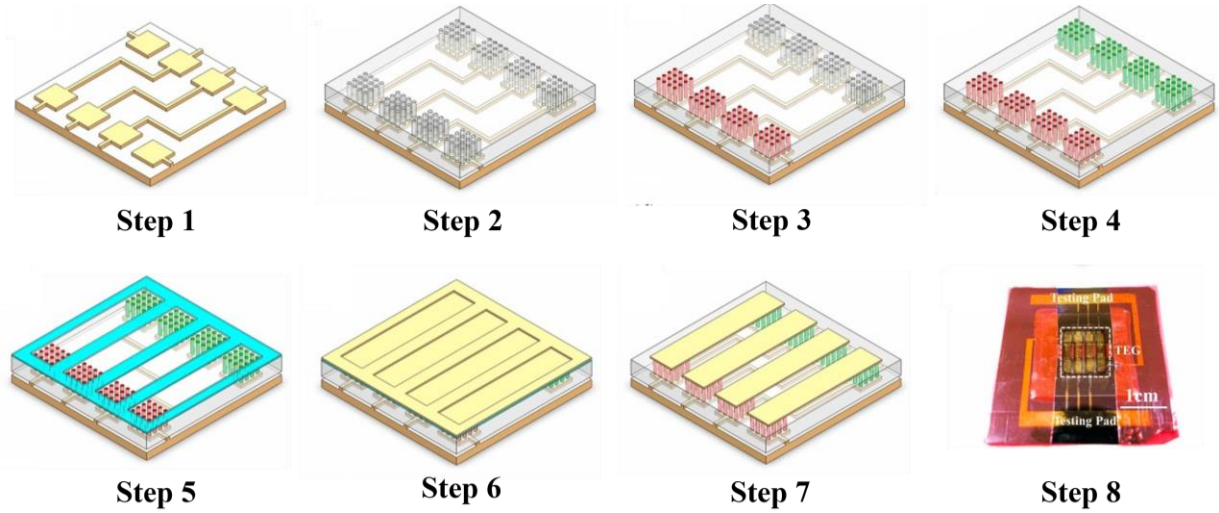

Figure 18. Step 1: Substrate patterned by photolithography and thermal evaporation of Ti/Pt/Au electrodes. Step 2: Glass template with array through-holes was placed on the substrate. Step 3 and Step 4: Electrodeposition of n-type Bi_2Te_3 and p-type Sb_2Te_3, respectively. Step 5: Mask placed on top. Step 6: Sputter Au layer on top. Step 7: Remove mask. Step 8: Photo of a micro-TEG with testing pads [226]. Copyright 2018, Elsevier. Reprinted with permission.

Regarding the processing of the cross-plane micro-TEGs, since a pair of TE legs includes one n-type and one p-type leg, one has to increase the TE couple quantity to increase the total energy output. However, their close locations on the same substrate greatly increases the processing difficulty at the micrometer scale. One has to precisely cover the region reserved for deposition of n-type B_2Te_3 during deposition of p-type B_2Te_3, thereby causing an increase in cost. As shown in **Figure 18**, Li et al. [226] used a pre-designed glass template with an array of through-holes to hold TE legs and a coupled bottom with patterned electrodes as WE for ED of Bi_2Te_3. The p- and n-type leg areas were separated by a certain distance, which simplified the step deposition of p- and n-type legs, greatly decreasing the processing difficulties for making micro-TEDs. Due to the large thermal resistance of the glass template, the TEG assembled with 4 thermocouples can maintain a maximum temperature gap of 138

K. The open circuit voltage and output power reached 40.89 mV and 19.72 μW, respectively. However, due to the large aspect ratio of the through-holes, the ions from the electrolyte cannot timely supplement these consumed in the holes, engendering large composition deviations, thus deteriorating device performance. Another demerit is its low packing density, due to the distance between the n- and p-leg regions.

The photolithography technology is commonly used in scalable fabrication of microelectronics. However, when depositing both n- and p-type legs on the same substrate, more processing steps need to be involved, wherein multiple photoresist layers are required, making the deposition of top-contacts an arduous task. To address this issue, the flip-chip bonding method using different solder materials have been proposed [225,227]. After electrodepositing n and p-type Bi_2Te_3 base TE legs on different substrates, it is easy to fulfil the top interconnects by using bonding materials after flipping one of the substrate/Bi_2Te_3 bodies. Lal et al. developed a cross-plane micro-TEG based on a combination of Bi_2Te_3 electrodeposition and the flip-chip method [227]. As shown in **Figure 19**, a 1 μm thick SiO_2 layer was first thermally grown on silicon substrate. Then, a seed layer of Ti/Au (20 nm/200 nm) was grown on the substrate by e-beam evaporation. Areas of 50 × 50 μm^2 were opened up by photoresist spin-coating, followed by exposing and developing. The 10 μm thick n-type Bi_2Te_3 pillars were electrodeposited on the exposed region. Then 200 nm thick Au and 3 μm thick In were sequentially electrodeposited, to act respectively as the barrier layer and bonding material for flip-chip bonding. It was considered that the stress from the electrodeposited Bi_2Te_3 pillars may result in its delamination along with the seed layer. This issue was solved by increasing the thickness of the Au layer from 200 nm to 3 μm by ED. Because ED can generate a rough surface, the adhesion between the pillars and the seed layer can be much enhanced, thereby enhancing the mechanical stability [80]. A different substrate

has also undergone a similar deposition sequence of p-type Bi_2Te_3 and bonding materials. The two substrates were then aligned to form a daisy chain in series. They were flip-chip bonded at 200 ℃ for 60 s with 300 gf. The TEG consists of 210 pairs of p- and n-type TE pillars, are connected thermally in parallel and electrically in series.

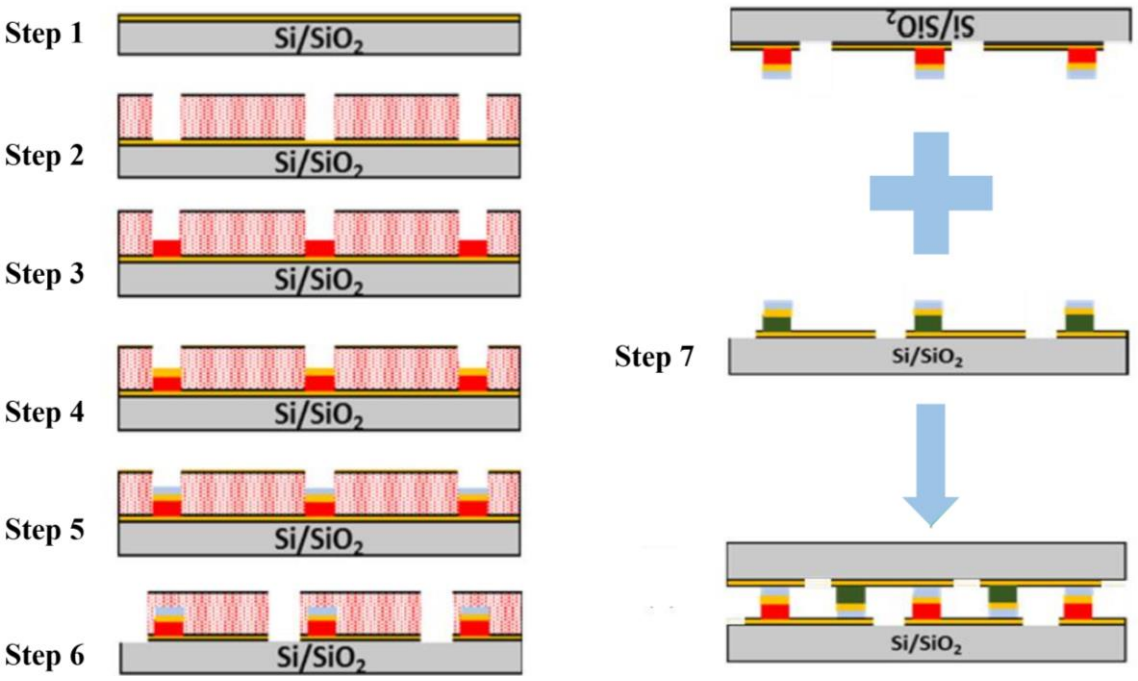

Figure 19. Schematic diagram for process flow of micro-TED made by flip-chip method. Step 1: e-beam evaporation of Ti/Au. Step 2: Patterning of photoresist. Step 3: Electrodeposition of Bi_2Te_3 pillar, Step 4: Electrodeposition of Au. Step 5: Electrodeposition of In. Step 6: Etching of seed layer. Step7: flip-chip bonding of substrate/ p- and n-type Bi_2Te_3 bodies [227]. Copyright 2019, IOP Publishing, Ltd. Reprinted with permission.

The Bi_2Te_3 TE pillars, the barrier layers, and the bonding layers are deposited on patterned substrates as shown in **Figure 20(a)**. **Figure 20(b)** revealed the top view features through the top silicon substrates using an X-ray imaging system. The daisy chain can be observed as well as the formation of the electrical contact by the perfect alignment of both dies. A slight overflow was observed near the edges of the pillars due to the height difference between the pillars. Fortunately, as

observed in **Figure 20(c)**, the overflowed indium does not short-circuit the connection. The TED made of 210 pairs of thermopiles are shown in **Figure 20(d)**, which could provide a voltage of ~ 315 mV, revealing a contribution of the *S* of 143.1 μV K^{-1} [227].

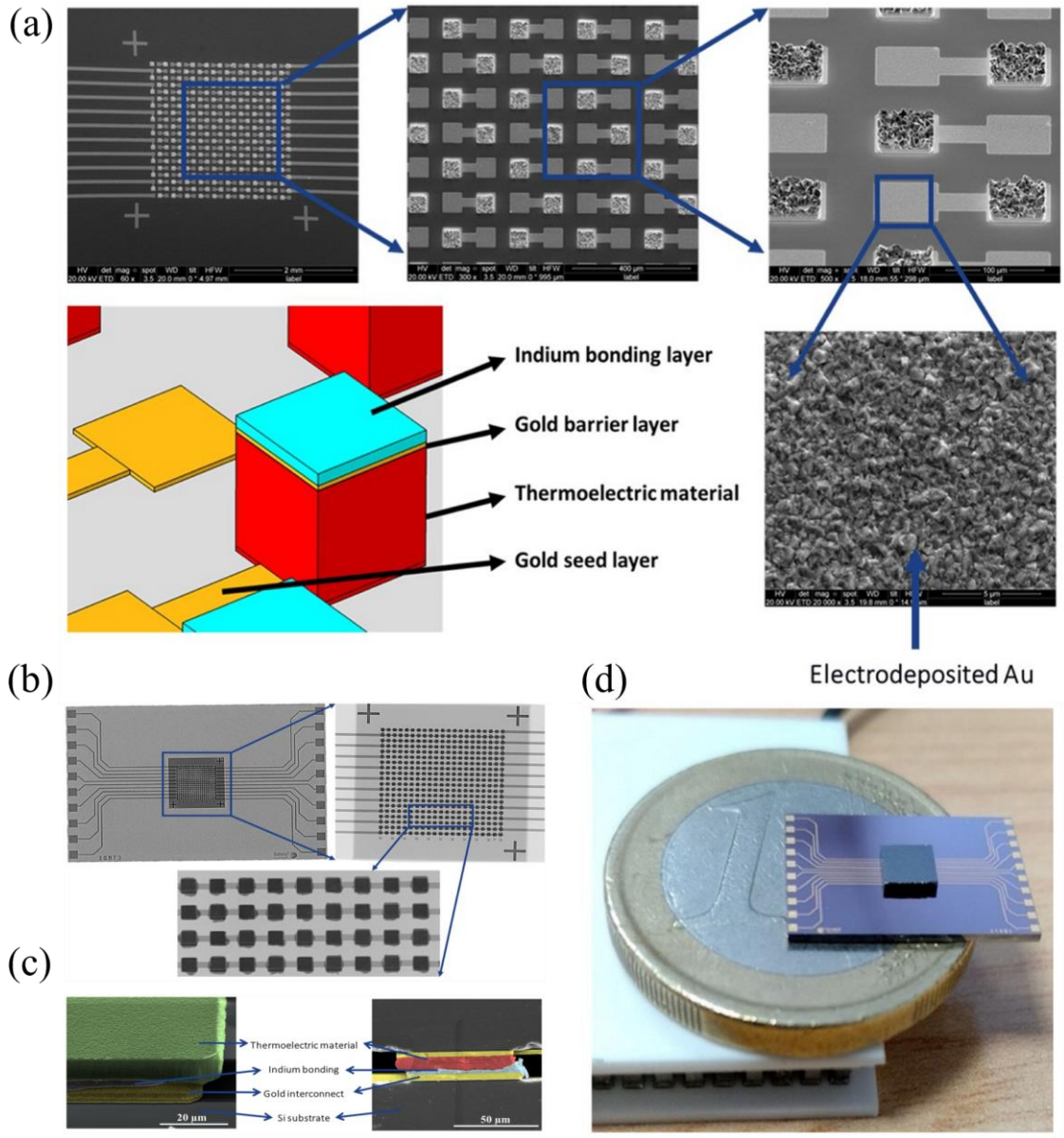

Figure 20. (a) Surface SEM images of completed substrate with electrodeposited Bi_2Te_3, Au barrier/seed material and In as bonding material. (b) X-ray imaging of the micro-TEG. (c) Cross-sectional SEM images of the flip-chip bonded micro-TEG. (d) Photo of the flip-chip bonded micro-TEG [227]. Copyright 2019, IOP Publishing, Ltd. Reprinted with permission.

7.2 Performance optimization

Much of the related research has been focused on structure optimization to boost the TE conversion performance of micro-TEGs. Optimization of the structure design for a larger TE output using the same mass of Bi_2Te_3 material is also very of great significant for reducing the scale-up cost of TEG fabrication. Tanwar et al. [224] gave some insight based on simulations: square cross-section TE legs have higher output than circular- and hexagonal- legs for a fixed projected area, due to a lower electrical resistance; the increase in leg height engenders a decrease in output power, due to a larger electrical resistance; the height of the top and bottom interconnection materials should be optimized for curtailing cost while keeping good electro-mechanical properties; the high thermal-conductive filler materials lead to a decrease in output power, due to thermal shunting; devices with an optimized cross-sectional area ratio of p/n-type leg outperform the ones with an equal leg cross-section due to the inferior TE properties of the p-type material.

Yazawa et al. [228] claimed that when the electrode size and the ratio of cross-sectional leg area/length are fixed, the TEG performance would be stable regardless of the total leg size, as shown in **Figure 21(a,b)**. Therefore, based on the same mass of Bi_2Te_3, one can prepare a larger quantity of small-sized legs with a fixed ratio of cross-sectional leg area/length. Integrating these legs with size-fixed electrodes, one can achieve a micro-TEG with a higher total power output. Uda et al. [229] further proved that when the number and size of TE-legs are fixed, the TEG performance could be improved by increasing the electrode area (**Figure 21(b,c)**). An umbrella-like electrode with a large area can collect heat energy to the fullest extent and thus increase power output. This umbrella-like electrode can also form a shadow on the bottom electrode, thus lowering the bottom temperature to help maintain the temperature gap. As shown in **Figure 21(d−f)**, when the size of TE leg is kept

constant, a 1.65-times increase in electrode area can bring in a 4.57-times increase in increment of power output. This strategy is meaningful for performance optimization as well as cost reduction: one can reduce the leg size for lower cost at a fixed electrode size, whereas one can increase electrode size for increasing power output at a fixed leg size.

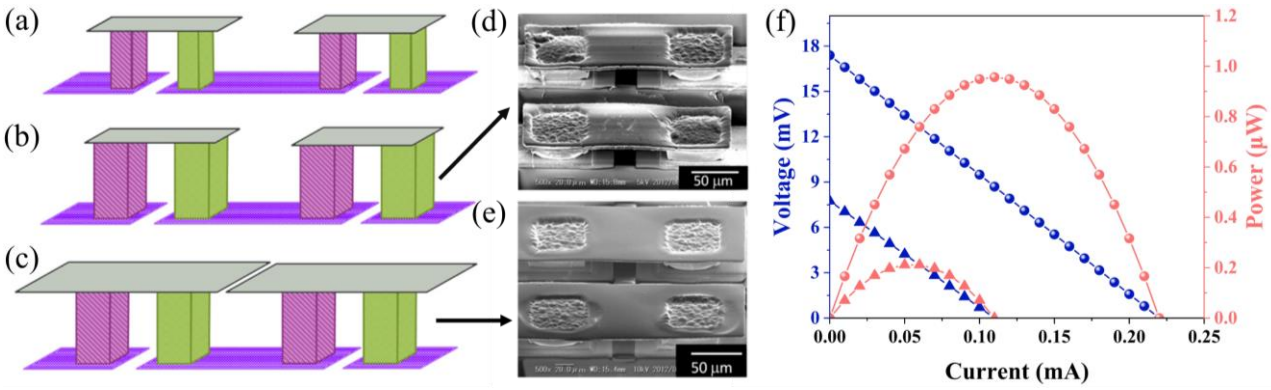

Figure 21. Schematic view of devices of small-sized (a) and large-sized (b) TE legs at fixed electrode size and aspect ratio, (c) larger-area electrode (umbrella-type) at fixed leg size and aspect ratio same to (b). Top-view SEM images of the device with small-area (d) and large-area (e) electrodes. (f) Output curves of device of small-area electrodes (triangles) and large-area electrodes (balls), corresponding to (d) and (e), respectively [229]. Copyright 2015, Elsevier. Reprinted with permission.

The power generation performance of the electrodeposited Bi-Te based micro-TEGs is listed in **Table 7**. It can be seen that TE properties reflected by compositions are of vital importance for the TE performance of the micro-TEGs. For example, the TEG with a Cu p-type leg revealed the lowest V_{oc} per couple per K, as the *S* of Cu is ultra-low, though the internal electrical resistance is also low. Lal et al. [227] deposited Cu-Te alloy as the n-leg for micro-TEG, which showed the best V_{oc} per couple per K. Another key point influencing power generation is the internal resistance. Zhang et al. [231] realized an ultra-low internal resistance, thus achieving the highest power output per couple per K, which is 1-3 orders of magnitude higher than others. To conclude, besides the TE properties of the materials, the

optimization of device structure, as well as the reduction of internal resistance are also of great importance for performance optimization of micro-TED.

Table 7. TE performances of Bi-Te based Micro-TEGs prepared by electrodeposition.

TE materials		ΔT (K)	No. of TCs	R/TC (×10² Ω)	V_{oc} (mV)	V_{oc} /(TC*ΔT) (mV/K)	P_{max} (μW)	P_{max} /(TC*ΔT) (×10² μW/K)	Ref.
n-leg	p-leg								
Cu_3Te_5	Bi_3Te_5	10.0	210	87.00	315.0	0.15	-	-	[227]
Bi_2Te_3	Sb_2Te_3	138.0	4	542.50	40.9	0.07	20	3.57	[226]
Bi_2Te_3	Sb_xTe_y	46.2	71	189.15	308.8	0.09	166	5.06	[230]
Bi_2Te_3	Sb_2Te_3	52.5	127	10.24	405.0	0.06	2990	44.84	[231]
Bi_2Te_3	Sb_2Te_3	22.3	242	1528.93	294.0	0.05	6	0.11	[232]
Bi_2Te_3	Sb_2Te_3	22.0	24	1250.00	56.0	0.10	-	-	[223]
Bi_2Te_3	Cu	1.9	7	0.57	0.6	0.04	-	-	[233]

Note: TC: Thermocouple, R/TC: Internal electrical resistance per thermocouple, P_{max}/TC: P_{max} per thermocouple, P_{max}/(TC*ΔT): P_{max} per ΔT per thermocouple.

For micro-TEDs, due to the micrometer scale leg-size as well as the massive increase in the leg-number per unit area, the contact electrical/thermal resistance between the electrode and the TE materials are greatly increased compared to the macro-TEDs, which has a remarkable effect on the TE performance of the TEDs. The optimization on the hetero-interface design is important for enhancing TE performance of the TEDs. Corbett et al. [215] electrodeposited a 5.5 μm thick Bi_2Te_3 leg on a Ti/Au/Si/SiO_2 substrate. Then, a 300 nm-thick SiN layer was deposited on top of the TE leg with an opening. Ar-ion etching was applied to remove carbon contamination and to activate the top open surface of the Bi_2Te_3 leg. Finally, 20 nm Ti, 100 nm W and 200 nm Au layers were deposited on top by electron beam evaporation (**Figure 22**). The W layer impedes the diffusion of Au into the Bi_2Te_3 film, thereby prolonging the lifespan of the TED. The contact electrical resistivity of the TED was only

~ 10^{-11} Ωm^2. The device shows a cooling response-time of 20 μs or less for the contacted devices of 22 μm diameter, which is two-orders-of-magnitude higher than the reported TEDs [234,235] **(Table 8)**. Recent work using an organic silane monolayer or electroless Co-P layer have proven effective to modify the metal-Bi_2Te_3 interfaces [236,237]. Future decreasing the electrical/thermal resistance between the TE material and the electrode is the key for performance optimization of the micro-TEDs.

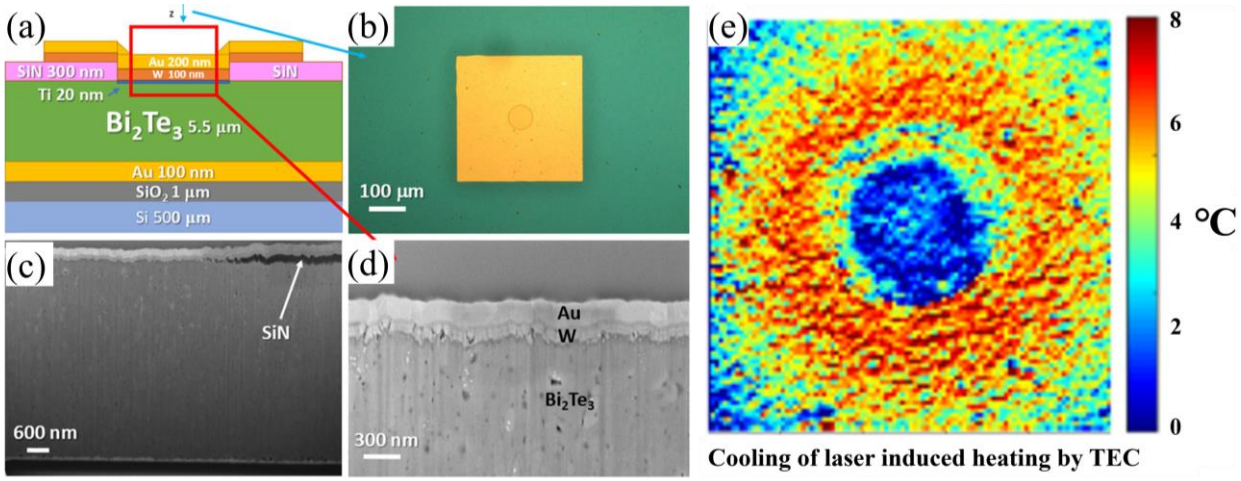

Figure 22. (a) Schematic diagram of cross section in a single-device structure showing top and bottom contacts. (b) Optical image of the 80 μm diameter pad with 400 μm side. (c) FIB-cut SEM image of the cross-sectional contact showing SiN layer transition. (d) FIB-cut SEM image of the top interfacial contacts showing W and Au layers. (e) Cooling effect of laser-induced heating by TED [215]. Copyright 2021, American Chemical Society. Reprinted with permission.

Table 8. Comparison of cooling performance of micro-TECs.

Composition	**Response time** ($\times10^{-2}$ ms)	**Contact resistance** (Ωm^2)	**ΔT** (K)	***COP*** ($\times10^{-1}$)	**Ref.**
Bi_2Te_3	2	10^{-11}	4.4	2.60	[215]
Bi_2Te_3-based ternary alloys	100	10^{-11}	6.0	0.74	[234]
SiGe	1000-3000	10^{-6}	-	-	[235]

8. Conclusions and Outlooks

TEDs can convert heat into electricity based on the Seebeck effect, and vice versa via the Peltier

effect. Generally, there are two main technologies—bulk and thin film technology for TED fabrication. The bulk technology is used where TEDs are of cm² or larger sizes (macro-TEDs) for W to kW power output; while thin film technology is used where TEDs are of mm² or smaller sizes (micro-TEDs) for μW to mW power output, in the areas of power supply for, or thermal management of, microelectronic/optoelectronic devices, wearable electronics, etc. The majority of the commercialized micro-TEDs are based on Bi_2Te_3. In contrast to macro-TEDs technology, Bi_2Te_3 material needs to be integrated into micro-TEDs in-situ, where the material processing determines the TE properties of the Bi_2Te_3 legs, thereby influencing the device performance. Among all film technologies, Bi_2Te_3 electrodeposition has unique advantages over traditional sputtering, evaporation, etc., due to its cost-effectiveness, facile processing, compatibility with CMOS based micro-fabrication and, most importantly, it can achieve a large film thickness for high electrical and thermal load. However, one of the main challenges for the electrodeposited Bi_2Te_3 in the near future will be to reach similar or above the efficiency of their bulk counterpart mainly fabricated by powder-sintered method.

8.1 Electrodeposition of high TE-property Bi_2Te_3

Generally, Bi_2Te_3 film is electrodeposited in a three-electrode system by the following reaction:

$$2\,Bi^{3+} + 3\,HTeO_2^{+} + 18\,e^{-} + 9\,H^{+} \rightarrow Bi_2Te_3 + 6\,H_2O \quad (4)$$

Bi^{III} and Te^{IV} ions are preferably provided by HNO_3 aqueous system, where Te^{IV} exists as $HTeO_2^{+}$. Due to the differences in solubility, mobility as well as onset potential, the optimal $C_{Bi^{III}}/C_{Te^{IV}}$ in electrolyte is (0.75 ~ 1):1, and appropriately high ionic concentrations in electrolyte and a low system temperature are preferred. Pulse deposition mode is favorable as it reserves the time for mass transfer, thereby making uniform composition. Annealing could help increase crystallinity and mean grain-size,

and alleviate defects. By annealing in Te vapor, or intercalating a Te supplement layer, or designing a diffusion barrier layer between Bi_2Te_3 and substrate could prevent composition deviation, thus enhancing the TE properties. Nanocomposites could induce interfacial/nanophase phonon scattering and energy-filtering effects, thereby depressing thermal conductivity and boosting Seebeck coefficient, respectively. Ternary doping with Sb and Se for p- and n-type Bi_2Te_3, respectively could enhance phonon scattering as well as carry out band engineering. Their detailed effects on the TE properties and mechanisms are summarized and listed in **Table 9**.

Some issues deserve concern for enhancing the TE properties of Bi_2Te_3 by ED: (1) Surfactants or some additives have been proven effective for adjusting nucleation and growth of Bi_2Te_3 during ED. The effect of each additive and their combinations on the microstructure and TE properties of Bi_2Te_3 and the underlying mechanisms deserve further systematic investigation. (2) Ternary Bi_2Te_3-based films by electrodeposition have revealed TE performances much lower than expected, which is attributed mainly to the composition deviation from the optimal $Bi_2Te_{2.7}Se_{0.3}$ or $Bi_{0.5}Sb_{1.5}Te_3$. It is an arduous task to realize optimal composition in the same electrolyte system, as the three ionic species have different mobilities. Selecting appropriate additives to form different complex structures with Bi^{III}, Te^{IV}, Sb^{III}, and Se^{IV} ions to manipulate their mobilities, may add another dimension for composition regulation. (3) Surface oxidation of Bi_2Te_3 during ED deteriorates TE performance, though the oxygen inward diffusion is slow. Inert and reducing gas purging to remove oxygen has already been adopted. A thin Te film as a protective layer is suggested to be deposited for hindering oxidation as well as to supplement Te volatilization in subsequent annealing. (4) It is challenging to maintain the ionic concentration in the optimal proportion range during long-term electrodeposition. A Bi_2Te_3 rod used as the CE can continuously supplement the consumed ions. However, the ionic concentration ratio may

be altered, as the optimal $C_{Bi^{III}}/C_{Te^{IV}}$ is not fixed at 2:3. Therefore, the stoichiometric ratio of the Bi_xTe_y needs to be predesigned. (5) Another challenge is to use less rare-earth and toxic materials (e.g., Te) and to move towards more sustainable and environmentally-friendly nanostructured materials and processes where electrodeposition may play a vital role. In terms of substrate/platform Si, SiC, AlN or other flexible biodegradable polymer-based substrates should be further investigated.

Table 9. Methodology and its influence on structure/composition as well as the structure/composition-performance relationship.

Methodology	Optimal	Structure/Composition	Structure/Composition-performance relationship
Solvent systems	HNO_3 aqueous solution	High ionic concentration	$Bi_2(SO_4)_3$ is insoluble in H_2SO_4; Cl^- chelates with Bi^{III} and Te^{IV} in HCl; ED in HNO_3 ensures large ionic concentration, form dense structure, large grain size, leading to high μ, and excellent σ.
Temperature	RT	Dense and uniform film	Higher temperature increases difference in ionic mobility, Te^{IV} cannot supplement its consumption, forming dendritic and loose structure, and leading to reduced μ; the composition is also deviated, leading to reduced *S*. promote current density, resulting in loose structure and reducing μ.
Concentration ratio	$C_{Bi^{III}} / C_{Te^{IV}}$ = (0.75 ~ 1):1	Bi:Te atomic ratio≈2:3 in film	Bi^{III} has a lower ionic mobility and more negative E_{onset} than Te^{IV} cations. An appropriate $C_{Bi^{III}}/C_{Te^{IV}}$ can ensure a stoichiometric atomic ratio (2/3) for optimized *PF* by regulating *n*.
Absolute concentration	$C_{Te^{IV}}$ = 8~15 mM	Dense film and low composition deviation	The smaller the absolute ionic concentration, the larger is the deviation from the stoichiometric one, since the ionic mobility of Te^{IV} is larger than that of Bi^{III}, even if $C_{Bi^{III}}/C_{Te^{IV}}$ is in the optimal range; too large ionic concentration will lead to a high current density, making a loose film.
Anti-oxidation process	Purge with inert gas; anneal in reduction atmosphere	Reduced oxygen content in Bi_2Te_3	Oxygen atoms occupy Te_2 positions and act as donors, leading to increased *n* and decreased *S*, while the induced defects will enhance electron scattering, reducing μ, and ultimately deteriorate TE properties.
Electrode size	$S_{CE} : S_{WE} \geq 4$,	Homogeneous composition	Reduce electrochemical polarization, stabilize the electric field for uniform composition.
Deposition mode	Pulse	Dense film and uniform composition	Reduce deposition rate and concentration polarization for a dense structure, thus enhancing μ; weaken concentration polarization to ensure a uniform composition with atomic ratio Bi:Te≈2:3, thus optimizing *S*.
Annealing	250 ~ 350°C;	Grain-size control and	Recrystallization by annealing, reduce grain boundaries and defects, improve the μ; benefit mass diffusion for a uniform
	~ 2 h; Inert Gas;	composition homogenization	composition with atomic ratio Bi:Te≈2:3, thus optimizing *S*.
	Te supplement layer	Supplement Te deficiency	Supplement Te deficiency due to volatilization to maintain the composition, thus optimizing *n*.
	TiN barrier layer	Impurity impeding	Maintain *n* and μ by adding a TiN diffusion barrier layer between the substrate and Bi_2Te_3 to prevent impurities from the substrate to the film due to annealing.
Nanocomposite	Pt	Bi_2Te_3/nanophase composite	Increase *S* by filtering out low-energy carriers and reduce κ_l by phonon-scattering by nanophase.
Ternary alloying	$Bi_{0.5}Sb_{1.5}Te_3$; $Bi_2Se_{2.7}Te_{0.3}$, etc.	Ternary composition	Reduce κ_l by point defect scattering; regulate the *n* for an optimized *PF* by forming antisite defects Sb'_{Te} to ionize holes in p-type $Bi_xSb_{1-x}Te_3$, and inducing Se vacancies ($V_{Se}^{\cdot\cdot}$) to ionize electrons in n-type $Bi_2Te_{3-y}Se_y$.

8.2 Processing and Structural design of high-performance micro-TEDs

Micro-TEDs could possess a high-power output with a large packing density. Electrodeposition of Bi_2Te_3 is one key step towards the in-situ integration process of micro-TEDs. As discussed, it is difficult to electrodeposit Bi_2Te_3 into predesigned array holes with large aspect-ratio in glass or organic templates, since only the hole bottom that contacts the electrode can exchange electrons with the ions from the electrolyte, so a greater overpotential is required. To make things even worse, the ions in the electrolyte cannot supplement the consumed ions at the bottom of the through-holes in a timely fashion due to space restriction, resulting in a loose-structure and composition-deviated Bi_2Te_3 legs. A multi-step pulse method combined with microwave-assisted electrodeposition is suggested to ensure timely mass transfer to ensure dense and stochiometric Bi_2Te_3 legs. For a higher fabrication scalability, the photolithography technology with a flip-chip method is proposed. It becomes easy to finish the top electrical-interconnects using bonding materials after flipping one of the two substrate/Bi_2Te_3 dies.

Regarding structural design, the topological structure including geometry, size, matching of current and heat flow, and the heterogeneous interface structure including electrode/Bi_2Te_3 are the main factors that influence the device performance. For in-plane micro-TEDs, a Y-shaped structure could realize long TE legs as well as a large film thickness, thereby establishing a larger temperature gap and smaller internal resistance. For cross-plane micro-TEDs, umbrella shape with a large electrode area is suggested to maximize heat collection and increase heat flow through TE legs, meanwhile, creating a shadow on the bottom electrode, thereby maintaining a large temperature gap. Square-cross-sectioned Bi_2Te_3 legs are preferred as they give higher output than the circular- and hexagonal- ones, due to lower electrical resistance for a fixed available area. The aspect-ratio of p and n-type Bi_2Te_3 leg

needs to be considered for matching of current and heat flows in future work.

Interfacial contact is one of the significant factors in devices performance. The contact electrical/thermal resistance in micro-TEDs are much larger than macro-TEDs, due to the micro-size dimensions as well as high integration density of micro-Bi_2Te_3 legs. Moreover, the metallic atoms could diffuse from the electrodes into the Bi_2Te_3 legs during long-term service, thereby degrading TE performance. Future works on appropriate bonding design, including interface modification, bonding materials selection and their stacking design, are vital for the reduction of these electrical/thermal resistance, and diffusion as well as strengthening the mechanical stability, which are the key factors for performance optimization of the micro-TEDs.

Notes

The authors declare no competing financial interest.

Acknowledgements

This work has been supported by the European Union's Horizon 2020-funded project under grant agreement no. 825114 (SmartVista), the Opening Project of State Key Laboratory of High-Performance Ceramics and Superfine Microstructure no. SKL202004SIC, National Science Foundation of China (no. 51702183), and the Priority Academic Program Development of Jiangsu Higher Education Institutions (PAPD). The authors also acknowledge support from Natural Science Foundation in Jiangsu Province (no. BK20211264) and General Program of Natural Science Research in Colleges of Jiangsu Province (21KJB430023). This publication emanated from research supported in part by a research grant from Science Foundation Ireland (SFI) and was co-funded under the European Regional Development Fund under Grant Number 15/IA/360, 12/RC/2276 and 13/RC/2077. We thank Professor Roger W. Whatmore for his generous help to read the manuscript and to provide

suggestions to improve it.

References

[1] Kaur K, Kumar S, Baliyan A. 5G: a new era of wireless communication. Int J Inf Tech Decis. 2020;12:619−624.
https://doi.org/10.1007/s41870-018-0197-x

[2] Snyder GJ, Toberer ES. Complex thermoelectric materials. Nat Mater. 2008;7:105−114.
https://doi.org/10.1038/nmat2090

[3] Kishore RA, Nozariasbmarz A, Poudel B, et al. Ultra-high performance wearable thermoelectric coolers with less materials. Nat commun. 2019;10:1−13.
https://doi.org/10.1038/s41467-019-09707-8

[4] Wang Y, Yang L, Shi XL, et al. Flexible thermoelectric materials and generators: challenges and innovations. Adv Mater. 2019;31:1807916.
https://doi.org/10.1002/adma.201807916

[5] Ma Y, Ahlberg E, Sun Y, et al. Thermoelectric properties of thin films of bismuth telluride electrochemically deposited on stainless steel substrates. Electrochim Acta. 2011;56:4216−4223.
https://doi.org/10.1016/j.electacta.2011.01.093

[6] Wu M, Binnemans K, Fransaer J. Electrodeposition of antimony from chloride-free ethylene glycol solutions and fabrication of thermoelectric $Bi_2Te_3/(Bi_{1-x}Sb_x)_2Te_3$ multilayers using pulsed potential electrodeposition. Electrochim Acta. 2014;147:451−459.
https://doi.org/10.1016/j.electacta.2014.08.111

[7]Zeng YJ, Wu D, Cao XH, et al. Nanoscale organic thermoelectric materials: measurement, theoretical models, and optimization strategies. Adv Funct Mater. 2020;30:1903873.
https://doi.org/10.1002/adfm.201903873

[8] Mao J, Chen G, Ren Z. Thermoelectric cooling materials. Nature Materials. 2021;20:454−461.
https://doi.org/10.1038/s41563-020-00852-w

[9] Witting IT, Chasapis TC, Ricci F, et al. The thermoelectric properties of bismuth telluride. Adv Electron Mater. 2019;5:1800904.
https://doi.org/10.1002/aelm.201800904

[10] Hao F, Qiu P, Tang Y, et al. High efficiency Bi_2Te_3-based materials and devices for thermoelectric power generation between 100 and 300 degrees C. Energ Environ Sci. 2016;9:3120−3127.

https://doi.org/10.1039/c6ee02017h
[11] Ren Z, Taskin AA, Sasaki S, et al. Optimizing $Bi_{(2-x)}Sb_xTe_{(3-y)}Se_y$ solid solutions to approach the intrinsic topological insulator regime. Phys Rev. 2011;84:p.1615311.1−165311.6.
https://doi.org/10.1103/PhysRevB.84.165311
[12] Mamur H, Bhuiyan MRA, Korkmaz F, et al. A review on bismuth telluride (Bi_2Te_3) nanostructure for thermoelectric applications. Renew Sust Energ Rev. 2018;82:4159−4169.
https://doi.org/10.1016/j.rser.2017.10.112
[13] Manzano CV, Abad B, Muñoz Rojo M, et al. Anisotropic effects on the thermoelectric properties of highly oriented electrodeposited Bi_2Te_3 films. Sci. Rep. 2016;6:19129−19136.
https://doi.org/10.1038/srep19129
[14] Delves RT, Bowley AE, Hazelden DW, et al. Anisotropy of the electrical conductivity in bismuth telluride. Proc Phys Soc. 1961;78:838.
https://doi.org/10.1088/0370-1328/78/5/329
[15] Goldsmid HJ. The thermal conductivity of bismuth telluride. Proc Phys Soc B. 1956;69:203.
https://doi.org/10.1088/0370-1301/69/2/310/meta
[16] Na J, Kim Y, Park T, et al. Preparation of bismuth telluride films with high thermoelectric power factor. ACS Appl Mater Inter. 2016;8:32392−32400.
https://doi.org/10.1021/acsami.6b10188
[17] Ma Y, Zhang D, Peng Z, et al. Delivery of platinum(iv) prodrugs via Bi_2Te_3 nanoparticles for photothermal–chemotherapy and photothermal/photoacoustic imaging. Mol Pharmaceut. 2020;17:3403−3411.
https://doi.org/10.1021/acs.molpharmaceut.0c00458
[18] Wada K, Tomita K, Takashiri M. Fabrication of bismuth telluride nanoplates via solvothermal synthesis using different alkalis and nanoplate thin films by printing method. J Cryst Growth. 2016;468,194−198.
https://doi.org/10.1016/j.jcrysgro.2016.12:048
[19] Hosokawa Y, Wada K, Tanaka M, et al. Thermal annealing effect on structural and thermoelectric properties of hexagonal Bi_2Te_3 nanoplate thin films by drop-casting technique. Jap J Appl Phys. 2018;57:02CC02.
https://doi.org/10.7567/JJAP.57.02CC02
[20] Mori R, Mayuzumi Y, Yamaguchi M, et al. Improved thermoelectric properties of solvothermally synthesized Bi_2Te_3 nanoplate films with homogeneous interconnections using Bi_2Te_3 electrodeposited layers. J Alloy Compd. 2019;818:152901.

https://doi.org/10.1016/j.jallcom.2019.152901
[21] Shi TF, Chen MR, Liu ZG, et al. A Bi_2Te_3-filled nickel foam film with exceptional flexibility and thermoelectric performance. Nanomaterials-Basel. 2022;12:1693.
https://doi.org/10.3390/nano12101693.
[22] Lu Y, Knize R J. Modified laser ablation process for nanostructured thermoelectric nanomaterial fabrication. Appl Surf Sci. 2007;254:1211−1214.
https://doi.org/10.1016/j.apsusc.2007.06.040
[23] Wudil YS, Gondal MA, Rao SG, et al. Substrate temperature-dependent thermoelectric figure of merit of nanocrystalline Bi_2Te_3 and $Bi_2Te_{2.7}Se_{0.3}$ prepared using pulsed laser deposition supported by DFT study. Ceram Int. 2020;46:24162−24172.
https://doi.org/10.1016/j.ceramint.2020.06.196
[24] Fourmont P, Gerlein LF, Fortier FX, et al. Highly efficient thermoelectric microgenerators using nearly room temperature pulsed laser deposition. ACS Appl Mater Inter. 2018;1012:10194−10201.
https://doi.org/10.1021/acsami.7b18852
[25] Chang HC, Chen TH, Whang WT, et al. Superassembling of Bi_2Te_3 hierarchical nanostructures for enhanced thermoelectric performance. J Mater Chem A. 2015;3:10459−10465.
https://doi.org/10.1039/C5TA00911A
[26] Zhang H, Momand J, Levinsky J, et al. Nanostructure and thermal power of highly-textured and single-crystal-like Bi_2Te_3 thin films. Nano Res. 2021;15:2382−2390.
https://doi.org/10.1007/s12274-021-3743-y
[27] Ahmad F, Singh S, Pundir SK, et al. Effect of doping and annealing on thermoelectric properties of bismuth telluride thin films. J Electron Mater. 2020;49:4195−4202.
https://doi.org/10.1007/s11664-020-08126-6
[28] Yang F, Zheng S, Wang H, et al. A thin film thermoelectric device fabricated by a self-aligned shadow mask method. J Micromech Microeng. 2017;27:055005.
https://doi.org/10.1088/1361-6439/aa64a3
[29] Vieira EMF, Figueira J, Pires AL, et al. Enhanced thermoelectric properties of Sb_2Te_3 and Bi_2Te_3 films for flexible thermal sensors. J Alloy Compd. 2018;774:1102−1116.
https://doi.org/10.1016/j.jallcom.2018.09.324
[30] Sudarshan C, Jayakumar S, Vaideki K, et al. Effect of vacuum annealing on structural, electrical and thermal properties of e-beam evaporated Bi_2Te_3 thin films. Thin Solid Films. 2017;629:28−38
https://doi.org/10.1016/j.tsf.2017.03.043
[31] Kim JK, Choi JY, Bae JM, et al. Thermoelectric characteristics of n-type Bi_2Te_3 and p-type Sb_2Te_3 thin films prepared by co-evaporation and annealing for thermopile sensor applications. Mater Trans.

2013;54:618−625.
https://doi.org/10.2320/matertrans.M2013010.
[32] Jitthamapirom P, Wanarattikan P, Nuthongkum P, et al. Comparison of thermoelectric properties of flexible bismuth telluride thin films deposited via DC and RF magnetron sputtering. Ferroelectrics. 2019;552:64−72.
https://doi.org/10.1080/00150193.2019.1653083
[33] Kurokawa T, Mori R, Norimasa O, et al. Influences of substrate types and heat treatment conditions on structural and thermoelectric properties of nanocrystalline Bi_2Te_3 thin films formed by dc magnetron sputtering. Vacuum. 2020;179:109535.
https://doi.org/10.1016/j.vacuum.2020.109535
[34] Takayama K, Takashiri M. Multi-layered-stack thermoelectric generators using p-type Sb_2Te_3 and n-type Bi_2Te_3 thin films by radio-frequency magnetron sputtering. Vacuum. 2017;144:164−171.
https://doi.org/10.1016/j.vacuum.2017.07.030
[35] Takahashi M, Katou Y, Nagata K, et al. The composition and conductivity of electrodeposited Bi-Te alloy films. Thin Solid Films. 1994;240:70−72.
https://doi.org/10.1016/0040-6090(94)90696-3
[36] Norimasa O, Takashiri M. In-and cross-plane thermoelectric properties of oriented Bi_2Te_3 thin films electrodeposited on an insulating substrate for thermoelectric applications. J Alloy Compd. 2022;899:163317.
https://doi.org/10.1016/j.jallcom.2021.163317
[37] Padmanathan N, Lal S, Gautam D, et al. Amorphous Framework in Electrodeposited CuBiTe Thermoelectric Thin Films with High Room-Temperature Performance. ACS Appl Electron Mater. 2021;3:1794−1803.
https://doi.org/10.1021/acsaelm.1c00063
[38] Tarancón A. Powering the IoT revolution with heat. Nat Electron. 2019;2:270−271.
https://doi.org/10.1038/s41928-019-0276-4
[39] Yu Y, Zhu W, Kong X, et al. Recent development and application of thin-film thermoelectric cooler. Front Chem Sci Eng. 2020;14:492−503.
https://doi.org/10.1007/s11705-019-1829-9
[40] Wu T, Kim J, Lim JH, et al. Comprehensive review on thermoelectric electrodeposits: enhancing thermoelectric performance through nanoengineering. Front Chem. 2021;9:762896.
https://doi.org/10.3389/fchem.2021.762896
[41] Rostek R, Stein N, Boulanger C. A review of electroplating for V–VI thermoelectric films: from

synthesis to device integration. J Mater Res. 2015;30:2518–2543.
https://doi.org/10.1557/jmr.2015.203
[42] Martın-González MS, Prieto AL, Gronsky R, et al. Insights into the electrodeposition of Bi_2Te_3. J Electrochem Soc. 2002;149:C546−C554.
https://doi.org/10.1149/1.1509459
[43] Jon JS, Ri WK, Sin KR, et al. Derivation of limiting ion mobility equation based on the application of solvation effect-incorporated Poisson-Boltzmann equation. J Mol Liq. 2022;347:117988.
https://doi.org/10.1016/j.molliq.2021.117988
[44]Schoenleber J, Stein N, Boulanger C. Influence of tartaric acid on diffusion coefficients of Bi^{III}, Sb^{III}, Te^{IV} in aqueous medium: Application of electrodeposition of thermoelectric films. Electroanal Chem. 2014;724:111−117.
https://doi.org/10.1016/j.jelechem.2014.04.004
[45] Sonkar PK, Prakash K, Yadav M, et al. Co (II)-porphyrin-decorated carbon nanotubes as catalysts for oxygen reduction reactions: an approach for fuel cell improvement. J Mater Chem A. 2017;5: 6263−6276.
https://doi.org/10.1039/c6ta10482g
[46]Jain A, Ong SP, Hautier G, et al. The Materials Project: A materials genome approach to accelerating materials innovation APL Materials, 2013;1:011002.
https://doi.org/10.1063/1.4812323
[47] Allen JB, György I, Fritz S. Electrochemical dictionary. Berlin, Heidelberg: Springer Berlin Heidelberg. 2012.
https://doi.org/10.1007/978-3-540-74598-3
[48] Li FH, Jia FL, Wang W. Studies of the electrochemical reduction processes of Bi^{3+}, $HTeO_2^+$ and their mixtures. Appl Surf Sci. 2009;255:7394−7402.
https://doi.org/10.1016/j.apsusc.2009.04.007.
[49] Bo X, Tang A, Dou M, et al. Controllable electrodeposition and mechanism research of nanostructured Bi_2Te_3 thin films with high thermoelectric properties. Appl Surf Sci. 2019;486:65−71.
https://doi.org/10.1016/j.apsusc.2019.04.194
[50] Oh JW, Seong Y, Shin DS, et al. Investigation and two-stage modeling of sintering behavior of nano/micro-bimodal powders. Powder Technology. 2019;352:42−52.
https://doi.org/10.1016/j.powtec.2019.04.056.
[51] Zhao D, Løvvik OM, Marthinsen K, et al. Segregation of Mg, Cu and their effects on the strength of Al Σ5 (210)[001] symmetrical tilt grain boundary. Acta Mater. 2018;145:235−246.

https://doi.org/10.1016/j.actamat.2017.12.023
[52] Li M, Ma Q, Zi W, et al. Pt monolayer coating on complex network substrate with high catalytic activity for the hydrogen evolution reaction. Sci Adv. 2015;1:e1400268.
https://doi.org/10.1021/10.1126/sciadv.1400268
[53]Schaefer C, Kirk AT, Allers M, et al. Ion mobility shift of isotopologues in a high kinetic energy ion mobility spectrometer (HiKE-IMS) at elevated effective temperatures. J Am Soc Mass Spectr. 2020;31:2093−2101.
https://doi.org/10.1021/jasms.0c00220
[54] Xu W, Cooper EI, Angell CA. Ionic liquids: ion mobilities, glass temperatures, and fragilities. J Phy Chem B. 2003;107:6170−6178.
https://doi.org/10.5555/10.1021/jp0275894
[55] Mirmahdieh S, Khayamian T, Saraji M. Analysis of dextromethorphan and pseudoephedrine in human plasma and urine samples using hollow fiber-based liquid‐liquid‐liquid microextraction and corona discharge ion mobility spectrometry. Microchim Acta. 2012;176:471−478.
https://doi.org/10.1007/s00604-011-0743-8
[56] Borsdorf H, Mayer T, Zarejousheghani M, et al. Recent developments in ion mobility spectrometry. Appl Spectrosc Rev. 2011;46:472−521.
https://doi.org/10.1080/05704928.2011.582658
[57] Manzano CV, Abad B, Martín-González M. The effect of electrolyte impurities on the thermoelectric properties of electrodeposited Bi_2Te_3 films. J Electrochem Soc. 2018;165:D768−D773.
https://doi.org/10.1149/2.1131814jes
[58] Chan TE, LeBeau JM, Venkatasubramanian R, et al. Carrier concentration modulation by hot pressing pressure in n-type nanostructured Bi(Se)Te alloy. Appl Phys Lett. 2013;103:144106−144110.
https://doi.org/10.1063/1.4823801
[59] Dou Y, Zhu Q, Du Y, et al. Enhanced thermoelectric performance of Cu_3SbSe_4 doped with alkali-ion (Na and K). Electron Mater Lett. 2020;16:99−105.
https://doi.org/10.1007/s13391-020-00198-0
[60] Shuai J, Kim HS, Lan Y, et al. Study on thermoelectric performance by Na doping in nanostructured $Mg_{1-x}Na_xAg_{0.97}Sb_{0.99}$. Nano Energy. 2015;11: 640−646.
https://doi.org/10.1016/j.nanoen.2014.11.027
[61] Kim Y J, Zhao L D, Kanatzidis M G, et al. Analysis of nanoprecipitates in a Na-doped PbTe–SrTe thermoelectric material with a high figure of merit. ACS Appl Mater Inter. 2017;9:21791−21797.
https://doi.org/10.1021/acsami.7b04098

[62] Zhu XG, Wen J, Wang G, et al. Doping nature of Cu in epitaxial topological insulator Bi_2Te_3 thin films. Surf Sci. 2013;617:156−161.
https://doi.org/10.1016/j.susc.2013.06.018
[63] Guo X, Zhang C, Liu Z, et al. Multiple roles of unconventional heteroatom dopants in chalcogenide thermoelectrics: the influence of Nb on transport and defects in Bi_2Te_3. ACS Appl Mater Inter. 2021;13:13400−13409.
https://doi.org/10.1021/acsami.1c00355
[64] Ivanov O, Yaprintsev M. Mechanisms of thermoelectric efficiency enhancement in Lu-doped Bi_2Te_3. Mater Res Express. 2018;5:015905.
https://doi.org/10.1088/2053-1591/aaa265
[65] Guo Z, Song K, Yan Z, et al. Broadening the optimum thermoelectric power generation range of p-type sintered $Bi_{0.4}Sb_{1.6}Te_3$ by suppressing bipolar effect. Chem Eng J. 2021;426:131853.
https://doi.org/10.1016/j.cej.2021.131853
[66] Kulbachinskiĭ VA, Kaminskiĭ AY, Tarasov PM, et al. Fermi surface and thermoelectric power of $(Bi_{1-x}Sb_x)_2Te_3$< Ag, Sn> mixed crystals. Phys Solid State+. 2006;48:833−840.
https://doi.org/10.1134/S1063783406050040
[67] Ni Y, Zhang Z, Nlebedim IC, et al. Ferromagnetism of magnetically doped topological insulators in $Cr_xBi_{2-x}Te_3$ thin films. J Appl Phys. 2015;117:17C748.
https://doi.org/10.1063/1.4918560
[68] Magri P, Boulanger C, Lecuire JM. Synthesis, properties and performances of electrodeposited bismuth telluride films. J Mater Chem C. 1996;6:773−779.
https://doi.org/10.1039/JM9960600773
[69] Kao CH, Chen KL, Chiu YS, et al. Comparison of NH_3 and N_2O plasma treatments on Bi_2O_3 sensing membranes applied in an electrolyte–insulator–semiconductor structure. Membranes. 2022;12:188.
https://doi.org/10.3390/membranes12020188
[70] Kang W, Li W, Chou W, et al. Microstructure and thermoelectric properties of Bi_2Te_3 electrodeposits plated in nitric and hydrochloric acid baths. Thin Solid Films. 2017;623:90−97.
https://doi.org/10.1016/j.tsf.2016.12.047
[71] Franklin TC. Some mechanisms of action of additives in electrodeposition processes. Surf Coat Tech. 1987;30:415−428.
https://doi.org/10.1016/0257-8972(87)90133-2
[72] Heo P, Hagiwara K, Ichino R, et al. Electrodeposition and thermoelectric characterization of Bi_2Te_3. J Electrochem Soc. 2006;153:C213−C217

https://doi.org/10.4028/www.scientific.net/AMR.634-638.682
[73] Martín-González M, Prieto AL, Knox MS, et al. Electrodeposition of $Bi_{1-x}Sb_x$ films and 200-nm wire arrays from a nonaqueous solvent. Chem Mater. 2003;15:1676−1681.
https://doi.org/10.1021/cm021027f
[74] Xia Y, Zhu D, Si S, et al. Nickel foam-supported polyaniline cathode prepared with electrophoresis for improvement of rechargeable Zn battery performance. J Power Sources. 2015;283:125−131.
https://doi.org/10.1016/j.jpowsour.2015.02.123
[75] Abellán M, Schrebler R, Gómez H. Electrodeposition of Bi_2Te_3 thin films onto FTO substrates from DMSO solution. Int J Electrochem Sci. 2015;10:7409−7422.
[76] Nguyen HP, Wu M, Su J, et al. Electrodeposition of bismuth telluride thermoelectric films from a nonaqueous electrolyte using ethylene glycol. Electrochim Acta. 2012;68:9−17.
https://doi.org/10.1016/j.electacta.2012.01.091
[77] Cicvarić K, Meng L, Newbrook DW, et al. Thermoelectric properties of bismuth telluride thin films electrodeposited from a nonaqueous solution. ACS Omega. 2020;5:14679−14688.
https://doi.org/10.1021/acsomega.0c01284g
[78] Van der Wal S. Low viscosity organic modifiers in reversed-phase HPLC. Chromatographia, 1985;20:274−278.
https://doi.org/10.1007/BF02310382
[79] Kestin J, Sokolov M, Wakeham WA. Viscosity of liquid water in the range – 8 °C to 150 °C. J Phys Chem Ref Data. 1978;7:941−948.
https://doi.org/10.1063/1.555581
[80] Jaworski AJ, Bolton GT. The design of an electrical capacitance tomography sensor for use with media of high dielectric permittivity. Meas Sci Technol. 2000;11:743.
https://doi.org/10.1088/0957-0233/11/6/318
[81] Warashina T, Hoshino H. Solvent effects for spectroscopic properties of near-infrared absorbing nickel–dithiolene complex [Ni (iPr$_2$timdt)$_2$](iPr$_2$timdt: monoanion of 1, 3-diisopropylimidazolidine-2, 4, 5-trithione). B Chem Soc Jan. 2016;89:836−841.
https://doi.org/10.1246/bcsj.20160060
[82] Kraus CA, Fuoss RM. Properties of electrolytic solutions. I. conductance as influenced by the dielectric constant of the solvent medium. J Am Chem Soc. 1933;55:21−36.
https://doi.org/10.1021/ja01328a003
[83] Wang P, Anderko A. Computation of dielectric constants of solvent mixtures and electrolyte solutions. Fluid Phase Equilibr. 2001;186:103−122.
https://doi.org/10.1016/S0378-3812(01)00507-6

[84] Jouyban A, Soltanpour S, Chan HK. A simple relationship between dielectric constant of mixed solvents with solvent composition and temperature. Int J Pharmaceut. 2004;269:353−360.
https://doi.org/10.1016/j.ijpharm.2003.09.010
[85] Creager S. Handbook of electrochemistry. Elsevier. 2007.
https://doi.org/10.1016/B978-044451958-0.50004-5
[86] Saad MA, Abdurahman NH, Yunus RM, et al. Surfactant for petroleum demulsification, structure, classification, and properties. A review. IOP Cof Ser Mater Sci Eng. 2020;991:012115.
https://doi.org/10.1088/1757-899X/991/1/012115
[87] Yoo IJ, Song Y, Lim DC, et al. Thermoelectric characteristics of Sb_2Te_3 thin films formed via surfactant-assisted electrodeposition. J Mater Chem A. 2013;1:5430−5435.
https://doi.org/10.1039/c3ta01631e
[88] Kulsi C, Mitra M, Kargupta K, et al. Effect of different surfactants and thicknesses on electrodeposited films of bismuth telluride and its thermoelectric performance. Mater Res Express. 2015;2:106403−106413.
https://doi.org/10.1088/2053-1591/2/10/106403
[89] Naylor AJ, Koukharenko E, Nandhakumar IS, et al. Surfactant-mediated electrodeposition of bismuth telluride films and its effect on microstructural properties. Langmuir. 2012;28:8296−8299.
https://doi.org/10.1021/la301367m
[90] Chien HC, Yang CR, Liao LL, et al. Thermal conductivity of thermoelectric thick films prepared by electrodeposition. Appl Therm Eng. 2013;51:75−83.
https://doi.org/10.1016/j.applthermaleng.2012.09.004
[91] Caballero-Calero O, Díaz-Chao P, Abad B, et al. Improvement of bismuth telluride electrodeposited films by the addition of sodium lignosulfonate. Electrochim Acta. 2014;123:117−126.
https://doi.org/10.1016/j.electacta.2013.12.185
[92] Liu P, Mitlin D. Emerging potassium metal anodes: perspectives on control of the electrochemical interfaces. Acc Chem Res. 2020;53:1161–1175
https://doi.org/10.1021/acs.accounts.0c00099
[93] Koch R. The intrinsic stress of polycrystalline and epitaxial thin metal films. J Phys-Condens Mat. 1994;6:9519−9550.
https://doi.org/10.1088/0953-8984/6/45/005
[94] Peng Z, Hong Y. Designer platinum nanoparticles: Control of shape, composition in alloy, nanostructure and electrocatalytic property. Nano Today. 2009;4:143−164.
https://doi.org/10.1016/j.nantod.2008.10.010

[95] Song Y, Yoo I, Heo N, et al. Electrodeposition of thermoelectric Bi_2Te_3 thin films with added surfactant. Curr Appl Phys. 2015;15:261−264.
https://doi.org/10.1016/j.cap.2014.12.004
[96] Athimotlu, Raju, Rajamani, et al. Effects of additives on kinetics, morphologies and lead-sensing property of electrodeposited bismuth films. J Phys Chem C. 2016; 120:22398−22406.
https://doi.org/10.1021/acs.jpcc.6b06924
[97] Liu F, Wang B, Xing Y, et al. Effect of polyvinyl alcohol on the rheological properties of cement mortar. Molecules. 2020;25:754.
https://doi.org/10.3390/molecules25030754
[98] Bhandari A, Hearne SJ, Sheldon BW, et al. Microstructural origins of saccharin-induced stress reduction in electrodeposited Ni. J Electrochem Soc. 2009;156:D279−D282.
https://doi.org/10.1149/1.3142363
[99] Saitou M, Oshiro S, Sagawa Y. Scaling behavior of internal stress in electrodeposited nickel thin films. J Appl Phys. 2008;104:1231.
https://doi.org/10.1063/1.3009336
[100] Sen R, Das S, Das K. Influence of sodium saccharin on the microstructure of pulse electrodeposited Ni–CeO_2 nanocomposite coating. J Nanosci Nanotechno. 2012;12:7944−7949.
https://doi.org/10.1166/jnn.2012.6654
[101] Yu W, Van Toan N, Li YJ, et al. Morphological analysis and properties evaluation of electrodeposited thick BiSbTe films with cooperative interactions among multiple additives. J Electrochem Soc. 2021;168:22505−22513.
https://doi.org/10.1149/1945-7111/abdd7b
[102] Saxena M, Okram G S, Lakhani A, et al. Enhanced thermoelectric performance of solution-grown Bi_2Te_3 nanorods. Mater Today Energy. 2021;21:100700.
https://doi.org/10.1016/j.mtener.2021.100700
[103] Kim WS, Anoop G, Jeong IS, et al. Feasible tuning of barrier energy in PEDOT: PSS/Bi_2Te_3 nanowires-based thermoelectric nanocomposite thin films through polar solvent vapor annealing. Nano Energy. 2020;67:104207.
https://doi.org/10.1016/j.nanoen.2019.104207
[104] Shi XL, Zou J, Chen ZG. Advanced thermoelectric design: from materials and structures to devices. Chem Rev. 2020;120:7399−7515.
https://doi.org/10.1021/acs.chemrev.0c00026
[105] Takahashi M, Kojima M, Sato S, et al. Electric and thermoelectric properties of electrodeposited bismuth telluride (Bi_2Te_3) films. J Appl Phys. 2004;96:5582−5587.

https://doi.org/10.1063/1.1785834
[106] Miyazaki Y, Kajitani T. Preparation of Bi_2Te_3 films by electrodeposition. J Cryst Growth. 2001; 229:542−546.
https://doi.org/10.1016/S0022-0248(01)01225-8
[107] Manzano CV, Rojas AA, Decepida M, et al. Thermoelectric properties of Bi_2Te_3 films by constant and pulsed electrodeposition. J Solid State Electr. 2013;17:2071−2078.
https://doi.org/10.1007/s10008-013-2066-7
[108] Burton MR, Richardson SJ, Staniec PA, et al. A novel route to nanostructured bismuth telluride films by electrodeposition. Electrochem Commun. 2017;76:71−74.
https://doi.org/10.1016/j.elecom.2017.02.004
[109] Zhu T, Hu L, Zhao X, et al. New insights into intrinsic point defects in V_2VI_3 thermoelectric materials. Adv Sci. 2016;3:1600004.
https://doi.org/10.1002/advs.201600004
[110] Yoo I, Myung NV, Lim DC, et al. Electrodeposition of Bi_xTe_y thin films for thermoelectric application. Thin Solid Films. 2013;546:48−52.
https://doi.org/10.1016/j.tsf.2013.05.036
[111] Ma LS, Zhang Q, Zhao QQ, et al. Synthesis and characterization of Bi_2Te_3/Te superlattice nanowire arrays. J Nanosci Nanotechnol. 2016;16:1207−1210.
https://doi.org/10.1166/jnn.2016.10698
[112] Li WJ, Yu WL, Yen CY. Pulsed electrodeposition of Bi_2Te_3 and Bi_2Te_3/Te nanowire arrays from a DMSO solution, Electrochim Acta. 2011;58:510−515.
https://doi.org/10.1016/j.electacta.2011.09.075.
[113] Horak J, Čermák K, Koudelka L. Energy formation of antisite defects in doped Sb_2Te_3 and Bi_2Te_3 crystals. J Phys Chem Solids. 1986;47:805−809.
https://doi.org/10.1016/0022-3697(86)90010-7
[114] Satterthwaite CB, Ure RW. Electrical and thermal properties of Bi_2Te_3. Phys Rev. 1957;108:1164−1170.
http://dx.doi.org/10.1103/PhysRev.108.1164
[115] Zhang M, Liu W, Zhang C, et al. Evolution of atomic structure and electronic transport properties in n-type Bi_2Te_3 films via Bi_2 planar defects. Appl Phys Lett. 2021;118:103901.
https://doi.org/10.1063/5.0045518
[116] Bakavets A, Aniskevich Y, Yakimenko O, et al. Pulse electrodeposited bismuth-tellurium superlattices with controllable bismuth content. J Power Sources. 2020;450:227605−227613.
https://doi.org/10.1016/j.jpowsour.2019.227605

[117] Medlin DL, Erickson KJ, Limmer SJ, et al. Dissociated 1/3 〈0111〉 dislocations in Bi_2Te_3 and their relationship to seven-layer Bi_3Te_4 defects. J Mater Sci. 2014;49:3970−3979.
https://doi.org/10.1007/s10853-014-8035-4
[118] Golgovici F, Visan T. Electrochemical deposition of BiTe films from choline chloride–malonic acid mixture as ionic liquid. Chalcogenide Lett. 2012;10:427−434.
https://doi.org/10.5560/ZNA.2012-0073
[119] Hirofumi E, Mikito U, Toshiaki O. Electrodeposition of Sb, Bi, Te, and their alloys in $AlCl_3$–NaCl–KCl molten salt, Electrochim Acta. 2007;53:100−105.
https://doi.org/10.1016/j.electacta.2007.03.017.
[120] Masaki, Yamaguchi, Hiroki, et al. Characteristics of electrodeposited bismuth telluride thin films with different crystal growth by adjusting electrolyte temperature and concentration-sciencedirect. Curr Appl Phys. 2018;18:1513−1522.
https://doi.org/10.1016/j.cap.2018.09.008
[121] Lee T, Lee JW, Park KT, et al. Nanostructured inorganic chalcogenide-carbon nanotube yarn having a high thermoelectric power factor at low temperature. ACS Nano. 2021;15:13118−13128.
https://doi.org/10.1021/acsnano.1c02508
[122] Bando H, Koizumi K, Oikawa Y, et al. The time-dependent process of oxidation of the surface of Bi_2Te_3 studied by x-ray photoelectron spectroscopy. J Phys-Condens Mat. 2000;12:5607−5616.
https://doi.org/10.1088/0953-8984/12/26/307
[123] Abdelnabi AA, Lakhian V, McDermid J, et al. The effect of powder pre-treatment on the mechanical and thermoelectric properties of spark plasma sintered N-type bismuth telluride. J Alloy Compd. 2021;874:159782.
https://doi.org/10.1016/j.jallcom.2021.159782
[124]Jung M, Ji M, Han JH, et al. Atomic layer deposition of ZnO layers on Bi_2Te_3 powders: comparison of gas fluidization and rotary reactors. Ceram Int. 2022.
https://doi.org/10.1016/j.ceramint.2022.08.241
[125] Schultz JM, McHugh JP, Tiller WA. Effects of heavy deformation and annealing on the electrical properties of Bi_2Te_3. J Appl Phys. 1962;33:443−2450.
https://doi.org/10.1063/1.1728990
[126] Horio Y, Inoue A. Effect of oxygen content on thermoelectric properties of n-type $(Bi,Sb)_2(Te,Se)_3$ alloys prepared by rapid solidification and hot-pressing techniques. Mater Trans. 2006;47:1412−1416.
https://doi.org/10.2320/matertrans.47.1412

[127] Music D, Chang KK, Schmidt P, et al. On atomic mechanisms governing the oxidation of Bi_2Te_3.J Phys: Condens Matter. 2017;29:485705.
https://doi.org/10.1088/1361-648X/aa945f
[128] Rashid Mm, Chung G. Effect of deposition conditions on the microstructure and the thermoelectric properties of galvanostatically electrodeposited Bi_2Te_3 film. Surf Rev Lett. 2013;20:1350044−1350052.
https://doi.org/10.1142/S0218625X13500443
[129] Frano B. PEM Fuel Cells. Academic Press. 2013.
https://doi.org/10.1016/B978-0-12-387710-9.00002-3.
[130] Sablani S S, Goosen M F A, Al-Belushi R, et al. Concentration polarization in ultrafiltration and reverse osmosis: a critical review. Desalination. 2001,141:269−289.
https://doi.org/10.1016/S0011-9164(01)85005-0
[131] Li M, Anand RK. Recent advancements in ion concentration polarization. Analyst. 2016;141:3496−3510.
https://doi.org/10.1039/c6an00194g
[132] Tittes K, Bund A, Plieth W, et al. Electrochemical deposition of Bi_2Te_3 for thermoelectric microdevices. J Solid State Electr. 2003;7:714−723.
https://doi.org/10.1557/PROC-626-Z11.3
[133] Wu M, Ramírez SA, Shafahian E, et al. Electrodeposition of bismuth telluride thin films containing silica nanoparticles for thermoelectric applications. Electrochim Acta. 2017;253:554−562.
https://doi.org/10.1016/j.electacta.2017.09.012
[134] Thorat JB. Surface deformation study of the electrodeposited nanostructured Bi_2Te_3 and Sb_2Te_3 thin films by double-exposure digital holographic interferometry. Phys Status Solidi A. 2019;216:1800661−1800672.
https://doi.org/10.1002/pssa.201800661
[135] Patil PB, Mali SS, Kondalkar VV, et al. Morphologically controlled electrodeposition of fern shaped Bi_2Te_3 thin films for photoelectrochemical performance. J Electroanal Chem. 2015;785:178−190.
https://doi.org/10.1016/j.jelechem.2015.09.019
[136] Rashid MM, Cho KH, Chung G. Rapid thermal annealing effects on the microstructure and the thermoelectric properties of electrodeposited Bi_2Te_3 film. Appl Surf Sci. 2013;279:23−30.
https://doi.org/10.1016/j.apsusc.2013.03.112
[137] Yamamuro H, Hatsuta N, Wachi M, et al. Combination of electrodeposition and transfer

processes for flexible thin-film thermoelectric generators. Coatings. 2018;8:22−31.
https://doi.org/10.3390/coatings8010022
[138] Takashiri M, Makioka T, Yamamuro H. Promotion of crystal growth in as-grown Bi_2Te_3 electrodeposited films without micro-pores using sputtered Bi_2Te_3 seed layers deposited on a glass substrate. J Alloy Compd. 2018;764:802−808.
https://doi.org/10.1016/j.jallcom.2018.06.143
[139] Zhou A, Fu Q, Zhang W, et al. Enhancing the thermoelectric properties of the electroplated Bi_2Te_3 films by tuning the pulse off-to-on ratio. Electrochim Acta. 2015;178:217−224.
https://doi.org/10.1016/j.electacta.2015.07.164
[140] Su N, Guo S, Li F, et al. Electrodeposition of Bi-Te thin films on silicon wafer and micro-column arrays on microporous glass template. Nanomaterials-Basel. 2020;10:43−447.
https://doi.org/10.3390/nano10030431
[141] Hernandez-Flores G, Poggi-Varaldo HM, Solorza-Feria O, et al. Tafel equation based model for the performance of a microbial fuel cell. Int J Hydrogen Energ. 2015;40:17421−17432.
https://doi.org/10.1016/j.ijhydene.2015.06.119
[142]Corović S, Pavlin M, Miklavcic D. Analytical and numerical quantification and comparison of the local electric field in the tissue for different electrode configurations. Biomed Eng Online. 2007; 6:37−37.
https://doi.org/10.1186/1475-925X-6-37
[143] Negi AS, Anand SC. A textbook of physical chemistry. New Age International. 1985.
https://doi.org/10.1016/B978-0-12-044262-1.X5001-4
[144] Soliman H, Kashyout AHB. Electrochemical deposition and optimization of thermoelectric nanostructured bismuth telluride thick films. Engineering. 2011;3:659−667.
https://doi.org/10.4236/eng.2011.36079
[145] Nguyen TH, Enju J, Ono T. Enhancement of thermoelectric properties of bismuth telluride composite with gold nano-particles inclusions using electrochemical Co-deposition. J Electrochem Soc. 2019;166:D508−D513.
https://doi.org/10.1149/2.1011912jes
[146] Yoo IJ, Lim DC, Myung NV, et al. Electrical/thermoelectric characterization of electrodeposited $Bi_x Sb_{2-x}Te_3$ thin films. Electron Mater Lett. 2013;9:687–691.
https://doi.org/10.1007/s13391-013-2246-8
[147] Frantz C, Stein N, Gravier L, et al. Electrodeposition and characterization of bismuth telluride nanowires. J Electron Mater. 2010;39:2043–2048.

https://doi.org/10.1007/s11664-009-1001-2
[148]Hammerich O. Organic electrochemistry. Boca Raton, FL: CRC press. 2016.
https://doi.org/10.1201/9781420029659
[149] Sankara P. Techniques for Corrosion Monitoring. Woodhead Publishing. 2008.
https://doi.org/10.1533/9781845694050.1.49.
[150] Conway BE, Wilkinson DP. Non-isothermal cell potentials and evaluation of entropies of ions and of activation for single electrode processes in non-aqueous media. Electrochim acta. 1993;38:997−1013.
https://doi.org/10.1016/0013-4686(93)87020-E
[151] Zhou J, Lin QH, Li HY, et al. Phosphorus-doped bismuth telluride films by electrodeposition. Mater Chem Phys. 2013;141:401−405.
https://doi.org/10.1016/j.matchemphys.2013.05.033
[152] Agapescu C, Cojocaru A, Cotarta A, et al. Electrodeposition of bismuth, tellurium, and bismuth telluride thin films from choline chloride–oxalic acid ionic liquid. J Appl Electrochem. 2013;43:309−321.
https://doi.org/10.1007/s10800-012-0487-0
[153] Zhu W, Yang JY, Gao XH, et al. Growth of bismuth telluride thin film on Pt by electrochemical atomic layer epitaxy. T Nonferr Metal Soc. 2005;15:404−409.
https://doi.org/10.1016/j.scriptamat.2004.12.017
[154] Zhou AJ, Wang WH, Yao X, et al. Investigation on the homogeneity of pulsed electrochemically deposited thermoelectric films with synchrotron μ-XRF, μ-XRD and μ-XANES. Appl Therm Eng. 2016;107:4215−4220.
https://doi.org/10.1016/j.applthermaleng.2016.05.037
[155] Reinsberg KG, Schumacher C, Tempez A, et al. Depth-profile analysis of thermoelectric layers on Si wafers by pulsed r.f. glow discharge time-of-flight mass spectrometry. Spectrochim Acta B. 2012;76:175−180.
https://doi.org/10.1016/j.sab.2012.06.005
[156] Cao Y, Zeng ZG, Liu YL, et al. Electrodeposition and thermoelectric characterization of (00L)-oriented Bi_2Te_3 thin films on silicon with seed layer. J Electrochem Soc. 2013;160:D565−D569.
https://doi.org/10.1149/2.099311jes
[157] Ma Y, Ahlberg E, Sun Y, et al. Thermoelectric characteristics of electrochemically deposited Bi_2Te_3 and Sb_2Te_3 thin films of relevance to multilayer preparation. J Electrochem Soc. 2011;159:D50−D58.
https://doi.org/10.1149/2.033202jes

[158] Yoo BY, Huang CK, Lim JR, et al. Electrochemically deposited thermoelectric n-type Bi_2Te_3 thin films. Electrochim Acta. 2005;50:4371−4377.
https://doi.org/10.1016/j.electacta.2005.02.016
[159] Puneet P, Podila R, Karakaya M, et al. Preferential scattering by interfacial charged defects for enhanced thermoelectric performance in few-layered n-type Bi_2Te_3. Sci Rep-UK. 2013,3:1−7.
https://doi.org/10.1038/srep03212
[160] Hamdou B, Kimling J, Dorn A, et al. Thermoelectric characterization of bismuth telluride nanowires, synthesized via catalytic growth and post-annealing. Adv Mater. 2013;25:239−244.
https://doi.org/10.1002/adma.201202474
[161] Nishizawa JI. Growth and crystal properties of Ti-doped PbTe crystals grown by Bridgman method under Pb and Te vapor pressure. J Cryst Growth. 2001;222:38−43.
https://doi.org/10.1016/S0022-0248(00)00875-7
[162] Suto K, Nishizawa J, Yasuda A. Calculation of the optimum vapor pressure for stoichiometry in PbTe and PbSnTe. Mat Sci Semicon Proc. 2003;6:289−292.
https://doi.org/10.1016/j.mssp.2003.08.022
[163] Rostek R, Sklyarenko V, Woias P. Influence of vapor annealing on the thermoelectric properties of electrodeposited Bi_2Te_3. J Mater Res. 2011;26:1785−1790.
https://doi.org/10.1557/jmr.2011.141
[164] Lal S, Gautam D, Razeeb KM. Optimization of annealing conditions to enhance thermoelectric performance of electrodeposited p-type BiSbTe thin films. Apl Mater. 2019;7:31102−31109.
https://doi.org/10.1063/1.5049586
[165] Lal S, Gautam D, Razeeb KM. The impact of surfactant sodium dodecyl sulfate on the microstructure and thermoelectric properties of p-type $(Sb_{1-x}Bi_x)_2Te_3$ electrodeposited films. Ecs J Solid State Sc. 2017;6:N3017−N3021.
https://doi.org/10.1149/2.0041703jss
[166] Wang C, Hsieh H, Sun Z, et al. Interfacial stability in Bi_2Te_3 thermoelectric joints. ACS Appl Mater Inter. 2020;12:27001−27009.
https://doi.org/10.1021/acsami.9b22853
[167] Koike J, Wada M. Self-forming diffusion barrier layer in Cu–Mn alloy metallization. Appl Phys Lett. 2005;87:041911.
https://doi.org/10.1063/1.1993759
[168] Nicolet MA. Diffusion barriers in thin films. Thin solid films. 1978;52:415−443.
https://doi.org/10.1016/0040-6090(78)90184-0

[169] Li W, Yan X, Aberle AG, et al. Effect of a TiN alkali diffusion barrier layer on the physical properties of Mo back electrodes for cigs solar cell applications. Curr Appl Phys. 2017;17:1747−1753. https://doi.org/10.1016/j.cap.2017.08.021
[170] Woo HJ, Lee WJ, Koh EK, et al. Plasma-enhanced atomic layer deposition of TiN thin films as an effective Se diffusion barrier for cigs solar cells. Nanomaterials-Basel. 2021;11:370. https://doi.org/10.3390/nano11020370
[171] Sato M, Kitada H, Takeyama MB. Characterization of tin films sputter-deposited at low temperatures for Cu-through-silicon via. Jpn J Appl Phys. 2019;58:SBBC03. https://doi.org/10.7567/1347-4065/ab01d9
[172] Qu Z, Wang W, Li X, et al. Measurement and error analysis of Cu film thickness with ta barrier layer on wafer for cmp application. IEEE T Instrum Meas. 2021;70:8000410. https://doi.org/10.1109/TIM.2020.3017057
[173] Tseng SC, Lee TC, Tsai HY. Diffusion effect for the catalytic growth of carbon nanotubes on metal alloys substrate. Diam Relat Mater. 2019;96:112−117. https://doi.org/10.1016/j.diamond.2019.04.020
[174] Boulat L, Viennois R, Oliviero E, et al. Study of TaN and TaN-Ta-TaN thin films as diffusion barriers in $CeFe_4Sb_{12}$ skutterudite. J Appl Phys. 2019;126:125306. 10.1063/1.5105385
[175] Xu H, Hu ZJ, Qu XP, et al. Effect of thickness scaling on the permeability and thermal stability of Ta(N) diffusion barrier. Appl Surf Sci. 2019;498:143887. https://doi.org/10.1016/j.apsusc.2019.143887
[176] Eguchi R, Yamamuro H, Takashiri M. Enhanced thermoelectric properties of electrodeposited Bi_2Te_3 thin films using TiN diffusion barrier layer on a stainless-steel substrate and thermal annealing. Thin Solid Films. 2020;714:138356−138312. https://doi.org/10.1016/j.tsf.2020.138356
[177] Hsu KF, Loo S, Guo F, et al. Cubic $AgPb_mSbTe_{2+m}$: bulk thermoelectric materials with high figure of merit. Science. 2004;303:818−821. https://doi.org/10.1126/science.1092963
[178] Gayner C, Amouyal Y. Energy filtering of charge carriers: current trends, challenges, and prospects for thermoelectric materials. Adv Funct Mater. 2020;30:1901789. https://doi.org/10.1002/adfm.201901789
[179] Yaprintsev M, Vasil'ev A, Ivanov O, et al. Forming the locally-gradient $Ni@NiTe_2$ domains from initial Ni inclusions embedded into thermoelectric Bi_2Te_3 matrix. Mater Lett. 2021;290:129451. https://doi.org/10.1016/j.matlet.2021.129451

[180] Wang Y, Zhang J, Shen Z, et al. Preparation of Bi_2Te_3/nano-SiC composite thermoelectric films by electrodeposition. J Electron Mater. 2015;44:2166−2171.
https://doi.org/10.1007/s11664-015-3747-z
[181] Eigler S, Enzelberger-Heim M, Grimm S, et al. Wet chemical synthesis of graphene. Adv Mater. 2013;25:3583−3587.
https://doi.org/10.1002/adma.201300155
[182] Zong P, Liang J, Zhang P, et al. Graphene-based thermoelectrics. ACS Appl Energy Mater. 2020, 3:2224–2239.
https://doi.org/10.1021/acsaem.9b02187
[183] Zong P, Hanus R, Dylla M, et al. Skutterudite with graphene-modified grain-boundary complexion enhances zT enabling high-efficiency thermoelectric device. Energ Environ Sci. 2017;10:183−191.
https://doi.org/10.1039/c6ee02467j
[184] Han X, Wei W. Synthesis and characterization of CNTs/Bi_2Te_3 thermoelectric nanocomposites. Int J Electrochem Sc. 2013; 8:6686−6691.
https://doi.org/10.1166/sl.2013.2670
[185] Xu H, Wang W. Electrodeposition of MWNT/Bi_2Te_3 composite thermoelectric films. J Electron Mater. 2013;42:1936−1945.
https://doi.org/10.1007/s11664-013-2479-1
[186] Li A, Fu C, Zhao X, et al. High-performance Mg_3Sb_{2-x} Bi_x thermoelectrics: progress and perspective. Research. 2020;2020:1934848.
https://doi.org/10.34133/2020/1934848
[187] Pallecchi I, Pani M, Ricci F, et al. Thermoelectric properties of chemically substituted full-Heusler $Fe_2TiSn_{1-x}Sb_x$ (x = 0, 0.1, and 0.2) compounds. Phys Rev Mater. 2018;2:075403.
https://doi.org/10.1103/PhysRevMaterials.2.075403
[188] Wang Z, Akao T, Onda T, et al. Formation of Te-rich phase and its effect on microstructure and thermoelectric properties of hot-extruded Bi-Te-Se bulk materials. J Alloy Compd. 2016;684:516−523.
https://doi.org/10.1016/j.jallcom.2016.05.232
[189] Jang J, Min BK, Kim BS, et al. Development of p-type $Bi_{2-x}Sb_xTe_3$ thermoelectric materials for power generation application exploiting synergetic effect of Sb alloying and repress process. Appl Surf Sci. 2019;508:145236−145242.
https://doi.org/10.1016/j.apsusc.2019.145236
[190] Kim HS, Heinz NA, Gibbs ZM, et al. High thermoelectric performance in $(Bi_{0.25}Sb_{0.75})_2Te_3$ due to band convergence and improved by carrier concentration control. Mater Today. 2017,20:452−459.

https://doi.org/10.1016/j.mattod.2017.02.007
[191] Hori T, Shiomi J. Tuning phonon transport spectrum for better thermoelectric materials. Sci Technol Adv Mater. 2019;20:10−25.
https://doi.org/10.1080/14686996.2018.1548884
[192] Witting IT, Ricci F, Chasapis TC, et al. The thermoelectric properties of n-type bismuth telluride: bismuth selenide alloys. Research. 2020;2020: UNSP 4361703.
https://doi.org/10.34133/2020/4361703
[193] Sootsman J, Chung D, Kanatzidis M. New and old concepts in thermoelectric materials. Angew Chem Int Edit. 2010;48:8616−8639.
https://doi.org/10.1002/anie.200900598
[194] Li L, Xu S, Li G. Enhancement of thermoelectric properties in Bi-Sb-Te alloy nanowires by pulsed electrodeposition. Energy Technol-Ger. 2015;3:825−829.
https://doi.org/10.1002/ente.201500071
[195] Lim S, Kim M, Oh T. Thermoelectric properties of the bismuth-antimony-telluride and the antimony-telluride films processed by electrodeposition for micro-device applications. Thin Solid Films. 2009;517:4199−4203.
https://doi.org/10.1016/j.tsf.2009.02.005
[196] Feng X, Hangarter C, Yoo B, et al. Recent progress in electrodeposition of thermoelectric thin films and nanostructures. Electrochim Acta. 2008;53:8103−8117.
https://doi.org/10.1016/j.electacta.2008.06.015
[197] Zhang Q, Fang T, Liu F, et al. Tuning optimum temperature range of Bi_2Te_3 based thermoelectric materials by defect engineering. Chem-Asian J. 2020;15:2775−2792.
https://doi.org/10.1002/asia.202000793
[198] Fang T, Li X, Hu C, et al. Complex band structures and lattice dynamics of Bi_2Te_3-based compounds and solid solutions. Adv Funct Mater. 2019;29:1900677.
https://doi.org/10.1002/adfm.201900677
[199] Chen J, Zhou X, Uher C, et al. Structural modifications and non-monotonic carrier concentration in $Bi_2Se_{0.3}Te_{2.7}$ by reversible electrochemical lithium reactions. Acta Mater. 2013;61:1508−1517.
https://doi.org/10.1016/j.actamat.2012.11.028
[200] Pan Y, Aydemir U, Sun FH, et al. Self-tuning n-type $Bi_2(Te, Se)_3$/SiC thermoelectric nanocomposites to realize high performances up to 300 °C. Adv Sci. 2017;4:1700259.
https://doi.org/10.1002/advs.201700259
[201] Ma Y, Wijesekara W, Palmqvist AE. Electrochemical deposition and characterization of thermoelectric ternary $(Bi_xSb_{1-x})_2Te_3$ and $Bi_2(Te_{1-y}Se_y)_3$ thin films. J Electron Mater.

2012;41:1138−1146.
https://doi.org/10.1007/s11664-011-1790-y
[202] Nolas G S, Sharp J, Goldsmid J. Thermoelectrics: basic principles and new materials developments. Springer Science & Business Media. 2001;45.
https://doi.org/10.1007/978-3-662-04569-5
[203] Wang W, Ji Y, Xu H, et al. A high packing density micro-thermoelectric power generator based on film thermoelectric materials fabricated by electrodeposition technology. Surf Coat Tech. 2013;231:583−589.
https://doi.org/10.1016/j.surfcoat.2012.04.048
[204] Nguyen T, Kei S, Nguyen T, et al. Synthesis and evaluation of thick films of electrochemically deposited Bi_2Te_3 and Sb_2Te_3 thermoelectric materials. Materials. 2017;10:154.
https://doi.org/10.3390/ma10020154
[205] Yamamuro H, Takashiri M. Power generation in slope-type thin-film thermoelectric generators by the simple contact of a heat source. Coatings. 2019;9:63−71.
https://doi.org/10.3390/coatings9020063
[206] Lei C, Ryder KS, Koukharenko E, et al. Electrochemical deposition of bismuth telluride thick layers onto nickel. Electrochem Commun. 2016;66:1−4.
https://doi.org/10.1016/j.elecom.2016.02.005
[207] Kang WS, Chou WC, Li WJ, et al. Electrodeposition of Bi_2Te_3-based p and n-type ternary thermoelectric compounds in chloride baths. Thin Solid Films. 2018;660:108−119.
https://doi.org/10.1016/j.tsf.2018.06.001
[208] Bu L, Wang W, Wang H. Effect of the substrate on the electrodeposition of $Bi_2Te_{3-y}Se_y$ thin films. Mater Res Bull. 2008;43:1808−1813.
https://doi.org/10.1016/j.materresbull.2007.07.002
[209] Zou ZG, Cai KF, Chen S, et al. Pulsed electrodeposition and characterization of $Bi_2Te_{3-y}Se_y$ film. Mater Res Bull. 2012;47:3292−3295.
https://doi.org/10.1016/j.materresbull.2012.07.036
[210] Kim J, Lee KH, Kim SW, et al. Potential-current co-adjusted pulse electrodeposition for highly (110)-oriented $Bi_2Te_{3-x}Se_x$ films. J Alloy Compd. 2019;787:767−771.
https://doi.org/10.1016/j.jallcom.2019.01.301
[211] Li F, Wang W. Electrodeposition of $Bi_xSb_{2-x}Te_y$ thermoelectric thin films from nitric acid and hydrochloric acid systems. Appl Surf Sci. 2009;255:4225−4231.
https://doi.org/10.1016/j.apsusc.2008.11.013
[212] Kfsa B, Nht A, To A. Enhancement in thermoelectric performance of electrochemically

deposited platinum-bismuth telluride nanocomposite. Electrochim Acta. 2019;312:62−71.
https://doi.org/10.1016/j.electacta.2019.04.139
[213] Kao PH, Shih PJ, Dai CL, et al. Fabrication and characterization of CMOS-MEMS thermoelectric micro generators. Sensors. 2010;10:1315−1325.
https://doi.org/10.3390/s100201315
[214] Lal S, Gautam D, Razeeb KM. Fabrication of micro-thermoelectric cooler for the thermal management of photonic devices. IEEE-NANO. 2018:1−2.
https://doi.org/10.1109/NANO.2018.8626304
[215] Corbett S, Gautam D, Lal S, et al. Electrodeposited thin-film micro-thermoelectric coolers with extreme heat flux handling and microsecond time response. ACS Appl Mater Inter. 2021;13:1773−1782.
https://doi.org/10.1021/acsami.0c16614
[216] Chung SH, Kim JT, Kim H, et al. High-temperature Bi_2Te_3 thermoelectric generator fabricated using Cu nanoparticle paste bonding. J Alloy Compd. 2022;896:163060.
https://doi.org/10.1016/j.jallcom.2021.163060
[217] Jiang CP, Fan X, Rong ZZ, et al. Elemental diffusion and service performance of Bi_2Te_3-based thermoelectric generation modules with flexible connection electrodes. J Electron Mater. 2017;46:1363−1370.
https://doi.org/10.1007/s11664-016-5135-8
[218] Tan M, Deng Y, Hao Y. Enhanced thermoelectric performance of a highly ordered vertical $Bi_{0.5}Sb_{1.5}Te_3$ pillar array device with optimized interconnect. Sci Adv Mater. 2015;6:1076−1082.
https://doi.org/info:doi/10.1166/sam.2015.2151
[219] Morgan KA, Tang T, Zeimpekis I, et al. High-throughput physical vapour deposition flexible thermoelectric generators. Sci Rep-Uk. 2019;9:4393−4401.
https://doi.org/10.1038/s41598-019-41000-y
[220] Wu Z, Mu E, Wang Z, et al. Bi_2Te_3 nanoplates' selective growth morphology on different interfaces for enhancing thermoelectric properties. Cryst Growth Des. 2019;19:3639−3646.
https://doi.org/10.1021/acs.cgd.8b01632
[221] Snyder GJ, Lim JR, Huang CK, et al. Thermoelectric microdevice fabricated by a mems-like electrochemical process. Nat Mater. 2003;2:528−531.
https://doi.org/10.1038/nmat943
[222] Yan J, Liao X, Yan D, et al. Review of micro thermoelectric generator. J Microelectromech S. 2018;27:1−18.
https://doi.org/10.1109/JMEMS.2017.2782748

[223] Nguyen HT, Nguyen VT, Takahito O. Flexible thermoelectric power generator with Y-type structure using electrochemical deposition process. Appl Energ. 2018;210:467−476.
https://doi.org/10.1016/j.apenergy.2017.05.005
[224] Tanwar A, Lal S, Razeeb KM. Structural design optimization of micro-thermoelectric generator for wearable biomedical devices. Energies. 2021;14:2339−2351.
https://doi.org/10.3390/en14082339
[225] O'Dwyer C, Chen R, He J, et al. Scientific and technical challenges in thermal transport and thermoelectric materials and devices. Ecs J Solid State Sc. 2017;6:N3058−N3064.
https://doi.org/10.1149/2.0091703jss
[226] Liu S, Hu B, Liu D, et al. Micro-thermoelectric generators based on through glass pillars with high output voltage enabled by large temperature difference. Appl Energ. 2018;225:600−610.
https://doi.org/10.1016/j.apenergy.2018.05.056
[227] Lal S, Gautam D, Razeeb KM. Fabrication of micro-thermoelectric devices for power generation and the thermal management of photonic devices. J Micromech Microeng. 2019;29:065015.
https://doi.org/10.1088/1361-6439/ab18f1
[228] Yazawa K, Shakouri A. Cost-efficiency trade-off and the design of thermoelectric power generators. Environ Sci Technol. 2011;45:7548−7553.
https://doi.org/10.1021/es2005418
[229] Uda K, Seki Y, Saito M, et al. Fabrication of π-structured Bi-Te thermoelectric micro-device by electrodeposition. Electrochim Acta. 2015;153:515−522.
https://doi.org/10.1016/j.electacta.2014.12.019
[230] Roth R, Rostek R, Cobry K, et al. Design and characterization of micro thermoelectric cross-plane generators with electroplated Bi_2Te_3, Sb_xTe_y, and reflow soldering. J Microelectromech S. 2014;23:961−971.
https://doi.org/10.1109/JMEMS.2014.2303198
[231] Zhang W, Yang J, Xu D. A high power density micro-thermoelectric generator fabricated by an integrated bottom-up approach. J Microelectromech S. 2016;25:1−6.
https://doi.org/10.1109/JMEMS.2016.2565504
[232] Kim MY, Oh TS. Thermoelectric power generation characteristics of a thin-film device consisting of electrodeposited n-Bi_2Te_3 and p-Sb_2Te_3 thin-film legs. J Electron Mater. 2013;42:2752−2757.
https://doi.org/10.1007/s11664-013-2671-3
[233] Pelz U, Jaklin J, Rostek R, et al. Fabrication process for micro thermoelectric generators (μTEGs). J Electron Mater. 2016;45:1502−1507.

https://doi.org/10.1007/s11664-015-4088-7
[234] Li G, Fernandez JG, Lara Ramos DA, et al. Integrated microthermoelectric coolers with rapid response time and high device reliability. Nat Electron. 2018;1:555−561.
https://doi.org/10.1038/s41928-018-0148-3
[235] Younes E, Christofferson J, Maize K, et al. Short time transient behavior of SiGe-based microrefrigerators. MRS Proc. 2011;1166:1166−N01−06.
https://doi.org/10.1557/PROC-1166-N01-06
[236] Wang CH, Hsieh HC, Lee HY, et al. Co-P diffusion barrier for p-Bi_2Te_3 thermoelectric material. J Electron Mater. 2018;48:53−57.
https://doi.org/10.1007/s11664-018-6633-7
[237] Cardinal T, Kwan M, Borca-Tasciuc T, et al. Multifold electrical conductance enhancements at metal-bismuth telluride interfaces modified using an organosilane monolayer. ACS Appl Mater Inter. 2017;9:2001−2005.
https://doi.org/10.1021/acsami.6b12488